Order Parameter Symmetry of the Electron-Doped Infinite-Layer Cuprate Superconductor $Sr_{1-x}La_xCuO_2$

Dissertation
der Mathematisch-Naturwissenschaftlichen Fakultät
der Eberhard Karls Universität Tübingen
zur Erlangung des Grades eines
Doktors der Naturwissenschaften
(Dr. rer. nat.)

vorgelegt von
Jochen Tomaschko
aus Böblingen

Tübingen
2012

Tag der mündlichen Qualifikation:	21. Februar 2012
Dekan:	Prof. Dr. Wolfgang Rosenstiel
1. Berichterstatter:	Prof. Dr. Dieter Kölle
2. Berichterstatter:	Prof. Dr. Reinhold Kleiner

Abstract

Crucial to the development of a microscopic theory of high transition temperature (high-T_c) superconductivity in the cuprates is the knowledge of the symmetry of the order parameter characterizing the pairing of electrons in the superconducting state. Cuprate superconductors with various crystal structures are known; however, all of them exhibit a common feature, the copper oxide (CuO_2) plane where Cooper pairs form. A cuprate essentially consisting of CuO_2 planes is therefore of special interest because secondary effects, possibly stemming from too complex crystal structures, can be ruled out in advance. This thesis explores the order parameter symmetry of such a simple cuprate, the electron-doped infinite-layer cuprate $Sr_{1-x}La_xCuO_2$ (SLCO), denoted as the parent structure of high-T_c superconductors. Four kinds of samples were fabricated and investigated, SLCO thin films, SLCO/gold/niobium planar tunnel junctions (PTJs), SLCO grain boundary Josephson junctions (GBJs), and an SLCO tetracrystal superconducting quantum interference device (SQUID). Strong evidence for a predominant $d_{x^2-y^2}$-wave (d-wave) symmetry of the order parameter of SLCO was found experimentally.

As a basis for the experimental work, single crystalline SLCO thin films with doping $x \approx 0.15$ and maximum $T_c = 22\,\mathrm{K}$ were grown epitaxially by means of pulsed laser deposition. [001]-oriented $KTaO_3$ and $SrTiO_3$ single crystals were used as substrates. In case of $SrTiO_3$, a $BaTiO_3$ thin film was deposited prior to SLCO, acting as buffer layer. To induce superconductivity, the as-grown SLCO thin films were annealed under reducing conditions, which is described in detail. The thin films were characterized by reflection high-energy electron diffraction, atomic force microscopy, x-ray diffraction, Rutherford backscattering spectroscopy, and electric transport measurements at temperatures down to $T = 4.2\,\mathrm{K}$. The influence of different process parameters on the final SLCO and $BaTiO_3$ thin film properties is discussed in detail.

To explore a potential s-wave component of the order parameter of SLCO, SLCO/-gold/niobium PTJs were fabricated by in-situ thin film technologies. Measurements of electric transport across these junctions did not exhibit any Cooper pair (CP) tunneling, however, nonlinear current-voltage characteristics gave evidence for quasiparticle (QP) tunneling across a thin insulating SLCO surface layer. To examine its origin, x-ray photoelectron spectroscopy and x-ray Auger-electron spectroscopy on SLCO thin film reference samples were performed, revealing a reduced copper species as the reason for insulating behavior, which is likely to be formed during post-deposition vacuum annealing of SLCO. Hence, PTJs could neither confirm nor exclude a potential s-wave component of the order parameter but yielded technically important information on the electronic state of the surface of SLCO.

To examine the superconducting gap and a potential d-wave specific subgap structure, SLCO GBJs were grown epitaxially on $BaTiO_3$-buffered 24° $SrTiO_3$ bicrystals. Both CP and QP tunneling was examined. CP tunneling revealed an extraordinary high critical current density for electron-doped cuprates of $j_c \gtrsim 1\,\mathrm{kA/cm^2}$ at $T = 4.2\,\mathrm{K}$. Thermally activated phase slippage was observed as a dissipative mechanism close to T_c and Fiske and flux flow resonances were visible. Out-of-plane magnetic fields H revealed remarkably regular Fraunhofer-like $j_c(H)$ patterns, as expected for either s-wave superconductors or for d-wave superconductors with an unfaceted grain boundary. By means of QP tunneling spectroscopy, the density of states was found to be V-shaped, indicative of a d-wave order parameter symmetry, with a zero-temperature energy gap $\Delta_0 \approx 2.4\,\mathrm{meV}$. No d-wave specific zero-bias

conductance peak was observed, which is discussed in terms of extrinsic influences, such as oxygen vacancies.

Since the order parameter symmetry of SLCO could not be pinpointed by the above-mentioned GBJ experiments, a phase-sensitive test was performed. For that purpose, an SLCO film was deposited on a $BaTiO_3$-buffered STO tetracrystal and two types of SQUIDs were patterned: a reference SQUID comprising one single grain boundary and a probe SQUID comprising the tetracrystalline point. The reference SQUID was designed to act as a conventional SQUID for both *s*-wave and *d*-wave symmetry, whereas the probe SQUID was designed to induce a frustrated ground state of the wave function only in case of *d*-wave symmetry. The magnetic field dependence of the critical current and of the *LC* resonance of the probe SQUID gave strong evidence for a frustrated ground state, implying predominant *d*-wave symmetry of the order parameter of SLCO.

Kurzfassung

Für die Entwicklung einer mikroskopischen Theorie der Hochtemperatur-Supraleitung in den Kupraten ist die Kenntnis der Ordnungsparameter-Symmetrie entscheidend, welche die Paarung der Elektronen im supraleitenden Zustand kennzeichnet. Es sind Kupratsupraleiter mit verschiedenen Kristallstrukturen bekannt, aber alle besitzen eine Gemeinsamkeit, die Kupferoxid (CuO_2)-Ebene, in der sich die Cooper-Paare bilden. Ein Kuprat, das im Wesentlichen aus CuO_2-Ebenen besteht, ist daher von besonderem Interesse, da Nebeneffekte, die möglicherweise von einer zu komplexen Kristallstruktur herrühren, im Voraus ausgeschlossen werden können. Diese Arbeit erforscht die Ordnungsparameter-Symmetrie eines solch einfachen Kuprats, des elektronendotierten Unendlichschichters $Sr_{1-x}La_xCuO_2$ (SLCO), der als Mutterstruktur der Hochtemperatur-Supraleiter bezeichnet wird. Vier Arten von Proben wurden hergestellt und untersucht, SLCO-Dünnfilme, planare SLCO/Gold/Niob-Tunnelkontakte, SLCO-Korngrenzen-Josephson-Kontakte und ein supraleitendes S-LCO-Tetrakristall-Quanteninterferometer (superconducting quantum interference device, SQUID). Es wurden deutliche experimentelle Hinweise auf eine dominante $d_{x^2-y^2}$-Wellen (d-Wellen)-Symmetrie des Ordnungsparameters von SLCO gefunden.
Als Grundlage der experimentellen Arbeit wurden einkristalline SLCO-Dünnfilme mit einer Dotierung $x \approx 0.15$ und einem maximalen $T_c = 22\,\mathrm{K}$ mittels gepulster Laserablation epitaktisch aufgewachsen. Als Substrate wurden [001]-orientierte $KTaO_3$- und $SrTiO_3$-Einkristalle verwendet. Im Falle von $SrTiO_3$ wurde vor dem SLCO-Dünnfilm ein $BaTiO_3$-Dünnfilm aufgewachsen, der als Pufferschicht diente. Wie ausführlich beschrieben wird, mussten die SLCO-Dünnfilme nach der Deposition unter reduzierenden Bedingungen getempert werden, um supraleitende Eigenschaften zu entwickeln. Die Dünnfilme wurden mittels Beugung hochenergetischer Elektronen bei Reflexion, Raster-Kraft-Mikroskopie, Röntgenbeugung, Rutherford-Rückstreu-Spektroskopie und elektrischer Transportmessungen bei Temperaturen bis minimal $T = 4.2\,\mathrm{K}$ charakterisiert. Der Einfluss verschiedener Prozessparameter auf die endgültigen Eigenschaften der SLCO- und $BaTiO_3$-Dünnfilme wird ausführlich behandelt.
Um eine potentielle s-Wellen-Komponente des Ordnungsparameters von SLCO zu erforschen wurden planare SLCO/Gold/Niob-Tunnelkontakte mithilfe verschiedener Dünnfilmtechnologien in-situ hergestellt. Elektrische Transportmessungen dieser Kontakte zeigten keinen Cooper-Paar-Tunnelstrom, jedoch deuteten nichtlineare Strom-Spannungs-Kennlinien auf einen Quasiteilchen-Tunnelstrom durch eine dünne, isolierende SLCO-Oberflächenschicht hin. Mithilfe von Röntgen-Photoelektronen-Spektroskopie und Röntgen-Auger-Elektronen-Spektroskopie an SLCO-Dünnfilmen als Referenz wurde eine reduzierte Form von Kupfer als Ursache des isolierenden Verhaltens identifiziert, welche sich wahrscheinlich während dem Vakuum-Tempern nach der Deposition bildete. Die planaren Tunnelkontakte konnten daher eine potentielle s-Wellen-Komponente weder bestätigen noch ausschließen, aber sie lieferten technisch relevante Informationen über den elektronischen Zustand der SLCO-Oberfläche.
Um die supraleitende Energielücke und eine d-Wellen-spezifische Struktur innerhalb der Lücke zu untersuchen wurden SLCO-Korngrenzenkontakte auf $BaTiO_3$-gepufferten 24° $SrTiO_3$-Bikristallen epitaktisch aufgewachsen. Sowohl das Cooper-Paar- als auch das Quasiteilchen-Tunneln wurde untersucht. Das Cooper-Paar-Tunneln zeigte eine für elektronendotierte Kuprate außergewöhnlich hohe kritische Stromdichte von $j_c \gtrsim 1\,\mathrm{kA/cm^2}$ bei $T = 4.2\,\mathrm{K}$. Thermisch aktivierter Phasenschlupf

wurde nahe T_c als dissipativer Mechanismus beobachtet und Fiske-Resonanzen sowie Resonanzen aufgrund von magnetischem Flussfließen waren sichtbar. Mithilfe eines Magnetfelds H senkrecht zur Probenebene wurden außergewöhnlich regelmäßige, Fraunhofer-artige $j_c(H)$-Muster nachgewiesen, wie sie entweder für s-Wellen-Supraleiter oder aber für d-Wellen-Supraleiter mit einer unfacettierten Korngrenze erwartet werden. Mittels Quasiteilchen-Tunnelspektroskopie wurde eine V-förmige Zustandsdichte nachgewiesen, die auf eine d-Wellen-Symmetrie des Ordnungsparameters hindeutete und bei $T = 0$ einen Wert der Energielücke von $\Delta_0 \approx 2.4\,\mathrm{meV}$ besaß. Eine d-Wellen-spezifische Zero-Bias-Anomalie wurde nicht beobachtet, was in Bezug auf äußere Einflüsse, wie z.B. Sauerstoff-Fehlstellen, diskutiert wird.
Da die Ordnungsparameter-Symmetrie von SLCO mithilfe der oben erwähnten Korngrenzen-Kontakte nicht eindeutig bestimmt werden konnte, wurde ein phasensensitives Experiment durchgeführt. Dazu wurde ein SLCO-Dünnfilm auf einem $BaTiO_3$-gepuffertem $SrTiO_3$-Tetrakristall aufgewachsen und zwei Arten von SQUIDs strukturiert: ein Referenz-SQUID, das eine einzelne Korngrenze umfasst, und ein Versuchs-SQUID, das den tetrakristallinen Punkt enthält. Das Referenz-SQUID war so ausgelegt, dass es sowohl bei s-Wellen- als auch bei d-Wellen-Symmetrie als gewöhnliches SQUID agiert, wohingegen das Versuchs-SQUID so ausgelegt war, dass es genau im Falle einer d-Wellen-Symmetrie einen frustrierten Grundzustand der Wellenfunktion induzieren würde. Die Magnetfeldabhängigkeit des kritischen Stroms und der LC-Resonanz des Versuchs-SQUIDs lieferten deutliche Hinweise auf einen frustrierten Grundzustand, was auf eine dominante d-Wellen-Symmetrie des Ordnungsparameters von SLCO schließen ließ.

List of puplications

This is a cummulative thesis which is based on the publications listed below. The publications are attached at the very end of the thesis. A fourth manuscript is in preparation. It is summarized in Sec. 4.2.

Publication I **J. Tomaschko**, V. Leca, T. Selistrovski, S. Diebold, J. Jochum, R. Kleiner, and D. Koelle,
Properties of the electron-doped infinite-layer superconductor $Sr_{1-x}La_xCuO_2$ epitaxially grown by pulsed laser deposition,
Phys. Rev. B **85**, 024519 (2012)

Publication II **J. Tomaschko**, C. Raisch, V. Leca, T. Chassé, R. Kleiner, and D. Koelle,
Electric transport across $Sr_{1-x}La_xCuO_2$/Au/Nb planar tunnel junctions and x-ray photoelectron and Auger-electron spectroscopy on $Sr_{1-x}La_xCuO_2$ thin films,
Phys. Rev. B **84**, 064521 (2011)

Publication III **J. Tomaschko**, V. Leca, T. Selistrovski, R. Kleiner, and D. Koelle,
Importance of grain-boundary Josephson junctions in the electron-doped infinite-layer cuprate superconductor $Sr_{1-x}La_xCuO_2$,
Phys. Rev. B **84**, 214507 (2011)

Contents

Introduction

Motivation

In 1911, three years after the first liquefaction of helium, Heike Kamerlingh Onnes discovered that the electric resistivity of mercury vanished at temperatures below $T = 4.2\,\mathrm{K}$[1]. He called this new state the superconductive state. For 22 years, superconductors were believed just to be ideal conductors, fully characterized by their vanishing resistivity ($\rho = 0$). However, in 1933, Walther Meissner and Robert Ochsenfeld experimentally found that superconductors also completely repel magnetic fields from their interior, irrespective of applying the magnetic field before or after cooling the sample below the critical temperature T_c[2]. Thus, ideal diamagnetism ($\vec{B} = 0$) was found to be an intrinsic property of the superconducting state, too, which helped to identify superconductivity as a thermodynamic phase. Only two years later, the brothers Fritz and Heinz London developed a phenomenological theory of superconductivity by extending Maxwell's equations to account for ideal conductivity and ideal diamagnetism[3]. One of the main achievements of the London theory was the explanation of diamagnetism by superconducting currents in a surface layer of thickness λ_L, shielding the interior from external magnetic flux. However, in 1936 Lev V. Shubnikov discovered that in some superconducting alloys magnetic fields could penetrate the interior of the sample without destroying the property of ideal conductance[4,5]. Those superconductors were called type-II superconductors to distinguish them from the abovementioned, ideally diamagnetic type-I superconductors. In 1950, Vitaly L. Ginzburg and Lev D. Landau presented their phenomenological theory of superconductivity[6]. The so-called GL theory is based upon Landau's theory of thermodynamic phase transitions[7]. To describe the totality of superconducting charge carriers, a quantum mechanical wave function $\Psi = \Psi_0 \exp(i\varphi)$ was introduced, which was furthermore identified with the order parameter Δ known from Landau's theory of phase transitions. In contrast to the London theory, the GL theory included spatial variations of the superconducting charge carrier density $n_s(\vec{r}) \equiv |\Psi(\vec{r})|^2$, leading to the prediction of another characteristic length scale, the coherence length ξ_{GL}, which describes the distance upon which n_s can change. Alexei A. Abrikosov used the GL theory to show that the ratio $\kappa = \lambda_L/\xi_{\mathrm{GL}}$ determines the sign of the interface energy σ_{ns} between normal and superconducting regions and could thereby explain the difference between type-I and type-II superconductors[8]. According to his theory, type-II superconductors exhibit negative σ_{ns}, which makes normal-to-superconductor interfaces energetically favorable, leading to the fragmentation of the inner flux to its smallest value, the magnetic flux quantum Φ_0. Almost half a century after the discovery of superconductivity, in 1957, John Bardeen, Leon N. Cooper, and John R. Schrieffer presented the microscopic explanation of superconductivity, the BCS theory[9]. One year earlier, Leon N. Cooper had shown that an arbitrarily small attractive electron-electron

interaction is sufficient to allow electrons to form bound states, lowering the energy of the system. Those bound states, called Cooper pairs, are made up of two electrons (or holes) with opposite $\vec{k}$ vector and (in most cases) with opposite spin, i.e. $\{\vec{k}\uparrow, -\vec{k}\downarrow\}$[10]. Consequently, the total spin of a Cooper pair is $S = 0$ and its total charge is $|q| = 2e$. As pointed out by BCS, an attractive electron-electron interaction can be mediated via lattice oscillations (phonons)[11,12], which was verified by experiments addressing the mass of the lattice atoms[13,14]. An important consequence of the BCS theory is that *all* Cooper pairs collectively occupy the *same* quantum state, i.e. they form a *macroscopic* quantum state of matter. If a Cooper pair is broken, the two single electrons, quasiparticles, occupy states which are no longer available to the totality of Cooper pairs, increasing the energy of the system. Finally, in 1959, Lev P. Gor'kov showed that the GL theory can be deduced from the BCS theory for temperatures close to T_c and the field of superconductivity seemed to be largely understood[15].

Surprisingly, since 1979 several families of so-called unconventional superconductors have been discovered. Simplifying, unconventional means that the pairing mechanism cannot be explained in terms of phonon mediated electron-electron interaction and that the superconducting energy gap has not an isotropic s-wave symmetry. A more elaborate definition of unconventional superconductivity takes account of symmetry breaking during the second-order phase transition: in conventional superconductors, only the one-dimensional global gauge symmetry is broken when T falls below T_c, whereas in unconventional superconductors, at least one more symmetry is broken (see e.g. Tsuei *et al.*[16]). Important families of unconventional superconductors are the heavy fermion metals, discovered by Frank Steglich in 1979 in $CeCu_2Si_2$[17], the cuprates, discovered by Johannes G. Bednorz and Karl A. Müller in 1986 in $La_{2-x}Ba_xCuO_4$[18], and the iron-based pnictides/chalcogenides (FeSCs), discovered by Yoichi Kamihara in 2008 in $LaO_{1-x}F_xFeAs$[19]. At ambient pressure, to date the maximum transition temperature is $T_c^{\max} = 2.3\,\mathrm{K}$ in the heavy fermion metals[20], 135 K in the cuprates[21], and 55 K in the FeSCs[22]. The latter two are therefore denoted as high-T_c superconductors. Despite intense research and various technical applications, the microscopic mechanism of unconventional superconductivity is still an open question. Only for the heavy fermion superconductors UPd_2Al_3[23] and $CeCu_2Si_2$[24], the pairing mechanism could be explained by antiferromagnetic excitons. Both in cuprates[25–27] and FeSCs[28,29], several experimental and theoretical results propose a pairing mechanism driven by antiferromagnetic spin fluctuations, which is however still under debate. Since the order parameter is dependent on the pairing mechanism, the determination of its symmetry is of fundamental significance. As a Cooper pair consists of two fermions, its wave function $\Psi(\vec{r}) = \chi \cdot \Phi(\vec{r})$ obeys Fermi-Dirac statistics[30–32], i.e. it is antisymmetric under the exchange of fermions. Besides some exceptions, such as Sr_2RuO_4[33–35] or UBe_{13}[36,37], most superconductors exhibit an antisymmetric spin wave function $\chi = (|\uparrow\downarrow\rangle - |\downarrow\uparrow\rangle)/\sqrt{2}$ (with eigenvalue $S = 0$) called singlet. Hence, the orbital part $\Phi(\vec{r})$ of the wave function must be symmetric, i.e. s-wave or d-wave like, corresponding to orbital angular momenta $L = 0$ or 2, respectively. To this day, all electron-phonon mediated superconductors, such as niobium or lead, were found to be s-wave superconductors. For the cuprates, a predominant d-wave order parameter[38–40] with only slight admixtures of an s-wave component[16,41,42] was detected. For the FeSCs, an $s_{\pm}$-wave was proposed, consistently explaining most of the experimental data[43–45] and theoretical calculations[46–48]. Finally, for the heavy fermion superconductors, both spin singlet (e.g. in UPd_2Al_3[23]) and spin triplet pairing (e.g. in UPt_3[49]) was detected. However,

due to complex interactions between lattice and electronic system, the actual order parameter symmetry of any of the heavy fermion superconductors has not yet been unambiguously determined[50,51] and p-, d-, and f-wave symmetry, as well as complex combinations of them, have been proposed[52,53].
Despite their diversity, members of different families of unconventional superconductors display remarkable similarities. Firstly, they are all anisotropic layered superconductors, i.e. their crystal is formed by quasi-two-dimensional superconducting planes (i.e. rare earth/actinide planes in the heavy fermion superconductors, CuO_2 planes in the cuprates, and FeAs planes in the FeSCs) and non-superconducting blocks, alternately stacked along the c-axis direction. Secondly, in their phase diagram, the superconducting phase is always in close proximity to an antiferromagnetic phase[51]. Thirdly, the magnetic ions (i.e. rare earth/actinide, Cu^{2+}, or Fe^{2+}), which are responsible for antiferromagnetism, are located in the superconducting planes. It is thus tempting to ask for a common unconventional pairing mechanism within the quasi-two-dimensional planes, probably closely related to antiferromagnetism. The most promising way to explore this basic question is to examine the simplest member of each family, which have unit cells essentially consisting of only one superconducting plane. The simplest member of the cuprates is the so-called infinite layer (IL) compound $ACuO_2$ (A = Ca or Sr)[54] and the simplest member of the FeSCs is the compound FeSe[55], both exhibiting superconductivity under doping[56,57]. Although several tests have firmly established predominant d-wave pairing in a number of cuprates[16], the symmetry of the IL compound is still under debate[58–67]. It is thus of fundamental interest, particularly with regard to the question of the pairing mechanism, whether d-wave pairing is inherent to all cuprate superconductors or if their simplest member exhibits a different order parameter symmetry.

Aim and outline

The issue of this work was twofold. First, a fabrication process yielding superconducting SLCO thin films had to be established. Secondly, experiments addressing fundamental properties of SLCO should be performed. The second part was driven by the question of the order parameter symmetry of SLCO.

This work is organized as follows: It consists of four chapters. The first three chapters refer to separate publications and the fourth chapter comprises data of a manuscript in preparation. The chapters start with an introduction to outline the physical context, followed by a summary of the publication or manuscript. This work finishes with a summary and outlook. The publications are attached at the very end of this work after the bibliography.

The **first chapter** deals with the fabrication of epitaxial SLCO thin films by means of pulsed laser deposition. The main issue was to establish a process to reproducibly synthesize superconducting SLCO thin films, the base of this work. The fabrication process and the influence of different process parameters on the final thin film properties, as examined by various in-situ and ex-situ techniques, are described in detail. In the **second chapter**, a study of SLCO/gold/niobium planar tunnel junctions is presented. In addition, x-ray photoelectron spectroscopy and x-ray Auger-electron spectroscopy were performed on SLCO thin film reference samples. All data is explained within one comprehensive model, giving a clear picture of the electric and electronic state of the SLCO surface.

In the **third chapter**, electric transport properties of epitaxial SLCO grain boundary Josephson junctions are discussed. Both Cooper pair and quasiparticle tunneling was examined. The superconducting gap was analyzed by means of quasiparticle tunneling spectroscopy, which is discussed with regard to the order parameter symmetry of SLCO.
In the **fourth chapter**, a phase-sensitive test of the order parameter symmetry of SLCO is presented. In an SLCO tetracrystal superconducting quantum interference device, strong evidence for a frustrated ground state of the wave function was found, allowing for a determination of the order parameter symmetry of SLCO.

Chapter 1

Fabrication and characterization of SLCO thin films

1.1 Introduction

Since the discovery of high transition temperature (high-T_c) superconductivity in copper oxides[18], tremendous work has been performed on these materials. Researchers succeeded in increasing T_c from initially 30 K to 135 K[68–70] by synthesizing increasingly complex compounds. However, the microscopic mechanism causing high-T_c superconductivity still has not been identified and is one of the biggest issues in solid state physics. It is therefore obvious, to ask what all these materials do have in common - it is the copper oxide (CuO_2) plane where superconducting charge carriers, Cooper pairs (CPs), form. A cuprate only consisting of CuO_2 planes is therefore of special interest for all questions addressing the basics of high-T_c superconductivity. Such a cuprate might help to identify the mechanism of high-T_c superconductivity because secondary effects, stemming from too complex crystal structures and hiding the actual mechanism, can be ruled out in advance.
In 1988, Siegrist *et al.* succeeded in synthesizing such a simple cuprate[54]. Its crystal is formed by stacks of CuO_2 planes along the *c*-axis direction, merely separated by a single alkaline earth metal plane (A^{II} = Ca, Sr or Ba), forming an $A^{II}CuO_2$ crystal. Formally, it is a member of the homologous series $A_2^{III}A_2^{II}Ca_{n-1}Cu_nO_{2n+4}$ (where A^{III} = Tl or Bi) with $n \to \infty$[54,71]. Hence, it is also called the infinite layer (IL) compound. Common features of cuprate superconductors, such as apical oxygen or charge reservoir blocks, are not present in the IL crystal[72]. Due to their simplicity, the IL compounds are known as the parent structure of cuprate superconductors. However, the undoped $A^{II}CuO_2$ crystal is not superconducting due to the lack of free charge carriers in the CuO_2 planes. To induce electron doping, the divalent alkaline earth metal A^{II} can be substituted partially by a trivalent lanthanide (L^{III} = La, Pr, Nd, Sm, or Gd) to form an $A^{II}_{1-x}L^{III}_xCuO_2$ crystal, or particularly as in this work a $Sr_{1-x}La_xCuO_2$ crystal[56,73,74], with maximum $T_c \approx 43$ K[56,73,75,76].
Some groups tried to synthesize hole-doped IL superconductors by partially substituting the alkaline earth metal by a monovalent alkaline metal, such as Li or Na. However, these hole-doped IL compounds did not exhibit superconducting behavior[77–79]. Azuma *et al.* reported on a hole-doped IL compound with $T_c = 110$ K[80]. Nevertheless, in this compound hole doping was induced by vacancies (possibly in the A^{II}-planes) and not by stoichiometric substitution. The crystal structure is thus not without controversy and might differ from the simple IL type[81]. Therefore, only the electron-doped IL compounds have been proven to be superconducting.

Besides IL compounds, only one more family of electron-doped cuprate superconductors is known. These are the T'-compounds. All other cuprate superconductors are hole-doped, such as $La_{2-x}Sr_xCuO_4$, $YBa_2Cu_3O_7$, $Bi_2Sr_2CaCu_2O_8$, $HgBa_2Ca_2Cu_3O_8$, and more. Electron doping is therefore rather an exception, making these materials even more interesting for fundamental research. The T'-compounds are characterized by the chemical formula $L^{\mathrm{III}}_{2-x}Ce_xCuO_4$, where L^{III} is a trivalent lanthanide such as La, Pr, or Nd[82,83]. They exhibit a charge reservoir block consisting of L^{III}, Ce, and O, i.e. they have a more complex crystal structure than IL compounds. Furthermore, their maximum T_c is about 15 K below the maximum T_c of the IL compounds[84,85].

To summarize, electron-doped IL compounds exhibit some unique features, which make them particularly interesting for fundamental research. These features are the simplest crystal structure among all cuprate superconductors, electron doping, and the highest T_c among electron-doped cuprate superconductors.

Despite their simple crystal structure, synthesizing superconducting IL compounds is challenging. No large single crystals have been synthesized so far and the synthesis of polycrystalline bulk material requires high pressure (~ 1 GPa)[74–76]. To overcome this problem, single crystalline IL thin films have been grown, where the high-pressure phase is stabilized by epitaxial strain[86,87]. However, in the first attempts, c-axis oriented $SrTiO_3$ (STO) was used as substrate[88,89]. As the in-plane lattice constant of STO ($a_{\mathrm{STO}} = 3.905$ Å)[90] is smaller than the in-plane lattice constant of electron-doped IL compounds ($a_{\mathrm{IL}} \approx 3.95$ Å)[56,75], the IL thin films were compressively strained. As a result, the IL thin films exhibited inferior superconducting properties. This was explained by the fact that compressive strain compresses the Cu−O bonds which in turn hampers electron doping of the CuO_2 planes[74]. Hence, the idea was to enhance the electron doping effect by epitaxially stretching the CuO_2 planes. For that purpose, thin layers of a material with in-plane lattice constants $a > a_{\mathrm{IL}}$ were deposited on top of STO prior to the deposition of the IL thin films. These layers, also called buffer layers, were able to provide tensile strain to the IL thin films and to allow for electron doping of the CuO_2 planes. Indeed, superconducting IL thin films were fabricated with this method, however still with reduced T_c[91–95]. Only one group succeeded in synthesizing IL thin films with T_c close to the maximum value[96]. The key was to choose $KTaO_3$ (KTO) as substrate, which exhibits a large in-plane lattice constant $a_{\mathrm{KTO}} = 3.988$ Å, making buffer layers redundant. In a later work, the same group showed that they could further increase T_c by the choice of another substrate, $DyScO_3$ (DSO). [110]-oriented DSO has an in-plane lattice constant of ~ 3.944 Å comparable to the in-plane lattice constant of electron-doped IL bulk material, resulting in relaxed IL thin films with less defects and superior superconducting properties[97].
In conclusion, *compressive* strain strongly suppresses superconductivity, whereas *tensile* strain enables superconductivity to emerge[96]. However, best superconducting properties are obtained for *relaxed* IL thin films[97].

Moreover, it was found that directly after deposition, IL thin films contained excess oxygen forming O^{2-} ions on interstitial sites in the $A^{\mathrm{II}}_{1-x}L^{\mathrm{III}}_x$ planes. On the one hand, interstitial oxygen localizes free charge carriers and on the other, it disturbs the crystal lattice due to its large ionic radius, altogether suppressing superconductivity[98]. Therefore, as introduced for T'-compounds before[99], a post-deposition vacuum annealing step was applied to remove excess oxygen. Meanwhile, this reduction step is a commonly used process for synthesis of superconducting IL thin films grown by various techniques, such as sputtering[100,101], pulsed laser deposition (PLD)[94,95]

and molecular beam epitaxy[96,97]. However, too strong reduction not only removes excess oxygen but also generates oxygen vacancies in the CuO_2 planes, destroying superconductivity[96,101]. A secondary phase can be formed if these vacancies arrange in an ordered structure, which is called the long c-axis phase or infinite layer-related (IL-r) phase[94,100,102,103]. Its unit cell $2\sqrt{2}a_{\mathrm{IL}} \times 2\sqrt{2}a_{\mathrm{IL}} \times c_s$ is a superstructure of the IL unit cell, where a_{IL} is the in-plane lattice parameter of the IL compound and c_s is the extended c-axis parameter of the superstructure (with $c_s \sim 3.6\,\text{Å}$ as compared to $c_{\mathrm{IL}} \sim 3.4\,\text{Å}$ for the IL compound).
Hence, the main challenge in synthesizing superconducting electron-doped IL compounds is to simultaneously reduce the $A^{\mathrm{II}}_{1-x}L^{\mathrm{III}}_{x}$ planes (e.g. $Sr_{1-x}La_x$ planes) without reducing the CuO_2 planes.

1.2 Summary of publication I

In this publication, we report on the fabrication of superconducting electron-doped SLCO films by means of pulsed laser deposition and on their characterization by in-situ and ex-situ techniques.

The fabrication process is described in detail. [001]-oriented STO and KTO single crystals were used as substrates, which allowed epitaxial growth of c-axis oriented, single crystalline SLCO films. Previous to the deposition of SLCO on STO, c-axis oriented $BaTiO_3$ (BTO) films with $a_{\mathrm{BTO}} \approx 3.994\,\text{Å}$ were deposited epitaxially, acting as buffer layers. In case of KTO, no buffer layers were deposited.

The growth mode, the evolution of the in-plane lattice constants, and the morphology of the BTO and SLCO films were monitored in-situ by high-pressure **reflection high-energy electron diffraction**. We observed a Stranski-Krastanov growth mode, i.e. two-dimensional layer growth with admixtures of three-dimensional island growth[104], for both BTO and SLCO films. Moreover, we found that BTO films almost completely relaxed after growth of a few unit cells and that a_{SLCO} increased during vacuum annealing, as expected for removal of excess oxygen.
Atomic force microscopy revealed very flat surfaces of BTO and SLCO with asperities in the range of $1-2$ and $1-3$ unit cells, respectively.
X-ray diffraction was used to check the crystal quality and lattice constants of the thin films. Intensity oscillations in $\Theta - 2\Theta$ scans, also known as Laue oscillations or fringes, and narrow rocking curves indicated high crystalline quality of the BTO and SLCO films. A comparison of the thin film lattice constants with literature bulk values showed that BTO buffer layers were almost completely relaxed, SLCO films on BTO-buffered STO (BTO/STO) moderately tensile strained, and SLCO films on KTO highly tensile strained.
The stoichiometry of SLCO films on BTO/STO was determined by **Rutherford backscattering spectroscopy**. A doping level of $x \approx 0.15$ was revealed, which is slightly above the nominal doping of the polycrystalline target ($x = 0.125$) and, according to literature, also above the doping level of SLCO polycrystals or thin films with maximum T_c ($x = 0.10$)[56,96].
Current-voltage characteristics and resistivity vs temperature were examined by **electric transport measurements**. At $T = 4.2\,\text{K}$, we determined the critical current density as $j_c \approx 2 \times 10^6\,\text{A/cm}^2$, comparable to the value reported for electron-doped T'-compounds[105]. The maximum T_c of the SLCO films was 22 K. This reduced value was explained by overdoping and by defects, such as excess oxygen, vacan-

cies, or dislocations. Moreover, despite exhibiting different degrees of tensile strain, SLCO films on BTO/STO and SLCO films on KTO showed comparable electric transport properties.

Furthermore, we discuss the influence of different process parameters on the final thin film properties, such as varying excimer laser energy E_L, target-to-substrate distance d_{TS}, deposition pressure p_{O_2}, vacuum annealing time t_a and vacuum annealing temperature T_a. We show that these parameters directly influence the oxygen content of the thin films and hence their electric transport properties.

Chapter 2

Planar SLCO/Au/Nb tunnel junctions

2.1 Introduction

A tunnel junction consists of two electrodes separated by a thin layer acting as tunneling barrier. For both application and fundamental research, tunnel junctions have shown to be helpful devices. In case of superconducting (S) electrodes, the tunneling barrier can be insulating (I) or normal conducting (N) and the corresponding tunnel junction is denoted as SIS-type or SNS-type tunnel junction*. Both Cooper pair (CP) and quasiparticle (QP) tunneling can be observed in superconducting tunnel junctions: If CPs are able to tunnel, the tunneling current is a supercurrent and no voltage drop occurs between the two superconducting electrodes. The physics underlying this scenario is known as Josephson tunneling, which is described by the two Josephson equations $j_s = j_0 \sin\delta$ and $V = \Phi_0/(2\pi)\cdot\dot{\delta}$ (where j_s = supercurrent density, j_0 = critical supercurrent density, δ = phase difference between electrodes, V = voltage between electrodes, and Φ_0 = magnetic flux quantum)[106,107]. The CP tunneling current is usually denoted as Josephson current. If the tunneling current cannot be sustained by the Josephson current, e.g. if the tunneling current density exceeds j_0 or if the barrier is too thick so that CPs are broken, the tunneling current is mediated by QPs, i.e. unpaired charge carriers, and a finite voltage $V \neq 0$ occurs. QP tunneling is known as Giaever tunneling[108,109]. It gives insight into the QP density of states $N_i(\epsilon)$ of the superconducting electrodes $i = 1$ and 2, which follows directly from the elastic tunneling model, yielding $j(V) \propto \int_{-\infty}^{\infty} d\epsilon\, |D(\epsilon)|^2 \cdot N_1(\epsilon) \cdot N_2(\epsilon + eV) \cdot [f(\epsilon) - f(\epsilon + eV)]$ (where ϵ = QP energy with respect to the Fermi energy, D = tunneling matrix element, and f = Fermi distribution). Thus, superconducting tunnel junctions are powerful tools to study the electronic properties of the underlying superconducting materials, with both CP and QP tunneling.

A planar tunnel junction (PTJ) is a special kind of tunnel device, where the tunnel junction area is defined by overlapping electrodes. Superconducting low-T_c PTJs based upon the well-established Nb/Al-Al_2O_3/Nb trilayer technology can be synthesized with fair reproducibility and solid superconducting properties[110]. The applicability of such low-T_c PTJs is large. For example, arrays of low-T_c PTJs are currently used as voltage standards[111] and single or multichannel SQUID systems based upon such PTJs are used for SQUID microscopy imaging[112,113] or biomag-

*Combinations, such as SNINS- or SINIS-type tunnel junctions, are also possible.

netic imaging (magnetoencephalography)[114,115]. Besides applications, low-T_c PTJs are also widely used for fundamental research, e.g. for studying the dynamics of fluxons in Josephson junctions[116].

Although high-T_c PTJs could increase the operation temperature for many applications, they are essentially used for fundamental research. They offer the great opportunity to study the electric transport properties of the electrode material(s) along distinct directions because the net supercurrent flows perpendicular to the PTJ area (see e.g. Tanaka *et al.*[117]). For example, if an *s*-wave superconductor (such as Pb) is deposited on top of a *c*-axis oriented superconductor (such as $YBa_2Cu_3O_7$), the electric transport properties of the latter along its *c*-axis can be studied. Such experiments were carried out on several cuprate superconductors to determine a possible *s*-wave contribution to the dominant *d*-wave order parameter[41,118]. The idea is as follows: A pure *d*-wave order parameter has lobes of equal amplitude but of opposite sign within the *a*-*b*-plane, thus, the net *c*-axis Josephson current in a PTJ should vanish. However, if there was a small *s*-wave contribution, a finite net *c*-axis Josephson current should occur. Indeed, PTJ experiments on *c*-axis oriented cuprates, such as $YBa_2Cu_3O_7$[41,118,119], $Nd_{2-x}Ce_xCuO_4$[120], and $Bi_2Sr_2CaCu_2O_8$[121], with Pb as counter electrode verified the presence of a finite subdominant *s*-wave component.

However, not only the (intrinsic) order parameter symmetry of the adjacent electrodes is decisive for the amplitude of the Josephson current, but also several extrinsic effects: Since PTJs comprise at least two surfaces (one between each electrode and the barrier), they are highly susceptible to the influence of defects preferentially located at surfaces, such as contamination, lattice defects (dislocations or surface reconstruction), and off-stoichiometry (impurity atoms or vacancies). In case of superconducting electrodes, these defects can lead to a suppression of the order parameter near the surface and hence to a disappearance of the Josephson current. However, in most cases, as in the examples given above, a finite Josephson current is required and the fabrication process has to be optimized to minimize the influence of surface defects.

In conclusion, PTJs are essential for both application and fundamental research, capable to yield information on the order parameter symmetry and on surface properties of the underlying material. Therefore, we have fabricated and characterized the first SLCO/gold/niobium (SLCO/Au/Nb) PTJs. These studies are presented in the following section 2.2.

2.2 Summary of publication II

In this publication, we report on electric transport measurements of SLCO/Au/Nb PTJs as well as on x-ray photoelectron spectroscopy (XPS) and x-ray Auger-electron spectroscopy (XAES) performed on SLCO thin films. We identified a reduced SLCO surface layer which is probably insulating.

In-situ grown PTJs with SLCO thin films as bottom electrode, thin gold (Au) interlayers and niobium (Nb) thin films as top electrode were fabricated for the first time and used for **electric transport measurements**. SLCO thin films were single crystalline and *c*-axis oriented. Our in-plane transport data show that below the

Nb transition temperature both electrodes are in the superconducting state. Out-of-plane electric transport measurements across the planar SLCO/Au/Nb tunnel junctions provide information on the interface and surface properties of the SLCO thin films. No Josephson current was observed. However, nonlinear current-voltage characteristics gave evidence for QP tunneling. An analysis of the QP conductance curves revealed a single gap value $\Delta \approx 1.4\,\mathrm{meV}$ at $T = 4.2\,\mathrm{K}$, which is characteristic for superconducting Nb. No superconducting SLCO gap was observed.
An interpretation of all these observations within the elastic tunneling model (see section 2.1) indicates a stacking of superconducting SLCO (bulk)/normal conducting SLCO/insulating SLCO (tunneling barrier)/superconducting Au/Nb along the sample normal. We further expect that the normal conducting/insulating SLCO surface layer is formed during vacuum annealing of the SLCO thin film right after growth.

In order to check the interpretation of our electric transport data, we examined the electronic structure and valence states of the SLCO surface layer. This was done by performing **XPS and XAES** measurements on SLCO thin films, which were fabricated under nominally identical conditions as used for the bottom SLCO electrode in the planar SLCO/Au/Nb tunnel junctions. Upon tilting the SLCO thin films (reducing the XPS/XAES information depth from $\sim 6\,\mathrm{nm}$ to $\sim 3\,\mathrm{nm}$), we identified a reduced surface component (with Cu valence +1 or 0) and an oxidized bulk component (with Cu valence +2) via XPS measurements[122–124]. The observation of Cu^{2+} in the bulk indicates fully oxidized CuO_2 planes, as expected for superconducting cuprates. In order to distinguish between Cu^{1+} and Cu^0 at the surface, XAES measurements were performed additionally, finally identifying Cu^{1+} to be present in the surface layer.

Furthermore, **x-ray diffraction** data on SLCO thin films indicated a disordered layer of $\sim 3\,\mathrm{nm}$ thickness, probably at the SLCO surface, which is consistent with both the XPS/XAES data and the out-of-plane transport data.

We can consistently interpret all our data, if we assume that the SLCO surface layer with Cu^{1+} is insulating. A likely scenario for its formation is the formation of a gradient of disordered oxygen vacancies along the SLCO film normal within the uppermost few nm. This could be due to the annealing step right after thin film deposition, and hence should occur for both the SLCO thin films and for the SLCO thin films within the SLCO/Au/Nb trilayer structures. On the one hand, such a gradient of oxygen vacancies can explain the XPS/XAES data (i.e. change in Cu valence states from +2 in the bulk to +1 on the surface). On the other hand, such a gradient can be assumed to change the SLCO thin films from superconducting to normal conducting and finally insulating along the surface normal, close to the SLCO thin film surface or SLCO/Au interface. This is supported by our out-of-plane transport data. Hence, our electric transport data for the planar SLCO/Au/Nb tunnel junctions are fully consistent with the XPS/XAES and XRD data on our SLCO thin films.

Finally, by high-temperature vacuum annealing in the XPS/XAES setup, we transformed one of the SLCO thin films from the IL phase into the infinite layer-related (IL-r) phase and performed the first XPS/XAES studies on the latter one. We showed, that the unit cell of the insulating IL-r phase contains mixed Cu valences

(+1 and +2). A comparison of the IL-r spectra with the IL spectra allowed us to pinpoint the spectral lines of the superconducting IL phase, in consistence with literature[125].

In conclusion, we fabricated the first PTJs based upon SLCO and showed that the absence of CP tunneling is due to a thin reduced SLCO surface layer. Optimized future samples, without reduced surface layer, might exhibit CP tunneling and provide information on a possible *s*-wave component of the order parameter of SLCO.

Chapter 3

SLCO grain boundary Josephson junctions

3.1 Introduction

The Josephson effect takes place at weak electrical coupling of two superconducting regimes[106,107]. Such a coupling can be realized in various ways, one example is given by PTJs described in chapter 2. Since cuprate superconductors exhibit a small coherence length ξ_{GL}[126], distortions on the atomic length scale, as realized by grain boundaries, can already act as weak links forming a Josephson junction. To create artificially one such grain boundary Josephson junction (GBJ), a cuprate thin film can be grown epitaxially on a bicrystalline substrate[127]. Such a substrate is composed of two tilt single crystalline grains comprising one grain boundary, which is transferred to the thin film during growth. Other possibilities to create GBJs are given by biepitaxial[128,129] or step-edge[130–132] techniques, as summarized by Hilgenkamp *et al.*[133].

The importance of GBJs in cuprate superconductors has been demonstrated by various experiments[133–135]. Chaudhari *et al.*[136] realized the first *single* YBCO GBJ and verified its functionality as a weak link. They further motivated the fabrication of high-T_c SQUIDs based upon GBJs, which could be used for scientific and practical purpose at temperatures up to the boiling point of liquid nitrogen ($T_{N_2} = 77\,\mathrm{K}$). In the aftermath, the optimization of high-T_c SQUIDs has paved the way for numerous applications[137], such as magnetocardiology[138,139] or SQUID microscopy[140].
Regarding fundamental research, high-T_c GBJs play a decisive role in experimental tests on the order parameter symmetry of cuprates[16]. An indication for d-wave pairing is the observation of a zero-bias conductance peak (ZBCP) in QP tunneling spectra, which shall be described briefly. As demonstrated by Hu *et al.*[141], repeated Andreev reflections[142,143] of QPs at a superconductor/normal conductor (S/N) interface can lead to the formation of bound states at zero QP energy ($\epsilon = E_F \equiv 0$) if the incident and specularly reflected QPs experience gap potentials of opposite sign. These so-called Andreev bound states (ABS) give rise to an increased zero-energy QP density of states $N(\epsilon = 0)$, which can be observed as a ZBCP in the QP tunneling spectra of S/N tunnel junctions[141,144,145]. The observation of ZBCPs in various hole-doped[146–151] and electron-doped[152–156] cuprate tunneling junctions was consistently ascribed to the d-wave symmetry of the underlying materials[16]. However, as there are alternate mechanisms that could give rise for a ZBCP[157,158], it is the task of the experimenters to show that the observed ZBCPs can be traced back to ABSs

in order to prove d-wave symmetry[159]. Moreover, the absence of a ZBCP cannot be interpreted as evidence for s-wave pairing, as done primarily for $Nd_{2-x}Ce_xCuO_4$ for example[149,160]. Subsequent experiments identified $Nd_{2-x}Ce_xCuO_4$ as a d-wave superconductor[161,162], demonstrating that the ZBCP had been suppresed for some other reason, such as disorder at the S/N-interface[163] or a too thick tunneling barrier[164,165].
Besides ZBCPs, the shape of the QP tunneling curves can also serve as an indication for the order parameter symmetry. For a fully gapped order parameter, such as s-wave, the subgap conductivity is U-shaped, while for an order parameter with nodes, such as d-wave, a V-shape is obtained, which is a direct consequence of the absence or presence of QP states close to the Fermi energy, respectively[166]. Thermal smearing[167] and lifetime limiting processes[168] are rounding the spectra but do not change the substantial shape of the subgap conductivity.

To lay the foundations for all kinds of experiments based on GBJs, we fabricated the first IL GBJs and examined their electric transport properties. The CP and QP tunneling results are presented in the following section 3.2.

3.2 Summary of publication III

In this publication, we report on the fabrication and characterization of bicrystalline SLCO GBJs. CP and QP tunneling was observed. Differences and similarities to hole-doped and electron-doped (T'-compound) cuprate GBJs are discussed, giving insight into basic properties of IL compounds.

To fabricate SLCO GBJs, SLCO thin films were grown by pulsed laser deposition on BTO-buffered 24 ° [001]-tilt symmetric STO bicrystals, as described in section 1.2. As confirmed by x-ray diffraction, SLCO thin films were c-axis oriented and current flow was restricted to the a-b-plane.

Initially, **CP tunneling** was examined at various temperatures ($4.2\,\mathrm{K} \leq T \leq 19\,\mathrm{K} = T_c$) **without magnetic field**. Current-voltage $I(V)$ characteristics showed resistively and capacitively shunted junction (RCSJ)-like behavior[169,170]. Numerical RCSJ simulations including thermal noise allowed us to determine specific properties of SLCO GBJs, such as the maximum Josephson current density $j_0 = 1.4\,\mathrm{kA/cm^2}$, the capacitance per junction area $c \approx 50\,\mu\mathrm{F/cm^2}$, and the areal resistance $\rho_n = 0.13\,\mu\Omega\mathrm{cm^2}$ at $T = 4.2\,\mathrm{K}$, which shall be discussed briefly.
The j_0 value is two orders of magnitude above that of corresponding GBJs from electron-doped T'-compounds[171,172], thus, probably the highest reported j_0 value for electron-doped cuprate GBJs. Furthermore, the product $j_0\rho_n \approx 0.18\,\mathrm{mV}$ is comparable to that of electron-doped GBJs, which *did not* exhibit a ZBCP[171,172], but 1 - 2 orders of magnitude smaller than that of hole-doped and electron-doped GBJs, which *did* exhibit a ZBCP[156,173]. However, the small value of $j_0\rho_n$ falls right on the scaling line $j_0\rho_n \propto 1/{\rho_n}^{1.5}$ found for YBCO GBJs[174], which is related to the oxygen stoichiometry at the tunneling barrier[133,174]. It is thus probably a fingerprint of oxygen vacancies due to vacuum annealing right after deposition (see chapter 1). According to the intrinsically shunted juntion model[174], barrier defects act as localized states, which enable resonant QP tunneling (explaining the small value of $j_0\rho_n$) and reduce the energy gap Δ at the barrier. Furthermore, as pointed out by Deutscher *et al.*[175], reduction of Δ yields a quadratic behavior $j_0 \propto (1-T/T_c)^2$ close

to T_c, which is in accordance with our $j_0(T)$ data and hence supports the assumption that oxygen vacancies are present in the barrier.
As reported for YBCO[176] and NCCO GBJs[171], we observed a foot structure in the resistance R versus temperature T curves just below T_c, which is due to thermally activated phase slippage, as described by Ambegaokar and Halperin[177] in full consistency with our data.

CP tunneling was examined in out-of-plane **magnetic fields** H at fixed temperature $T = 4.2\,\mathrm{K}$. A Fraunhofer-like modulation pattern of the critical current j_c versus H implied homogeneous current distribution across the junctions, as usually observed for s-wave superconductors. However, regarding d-wave pairing, this observation could also be explained if the grain boundary was unfaceted[133]. By analyzing the $j_c(H)$ patterns of GBJs with various widths w, we found that the oscillation period $\Delta H \propto w^{-2}$ instead of w^{-1}, which was explained by flux focusing in thin films[178].
Finally, we observed Fiske resonances[179] and flux flow resonances[180] as magnetic field dependent features in the $I(V)$ curves*. Since both resonances are related to the propagation of electromagnetic waves in the junction, we could determine the phase velocity (Swihart velocity)[181] to $c_S \approx 3.1 \cdot 10^6\,\mathrm{m/s}$, comparable to literature values for YBCO GBJs[182,183].

The superconducting energy gap Δ was examined by means of **QP tunneling** spectroscopy. For that purpose, differential conductance curves $dI/dV(V)$ were measured with lock-in technique, giving insight into the density of states of SLCO, as explained in section 2.1. As for other cuprates, the gap was found to be V-shaped in the subgap regime, which became more pronounced for decreasing temperature, suggesting that nodes are present in the superconducting order parameter and hinting at d-wave symmetry. The zero-temperature energy gap was extrapolated to $\Delta_0 \approx 2.4\,\mathrm{meV}$ and the reduced gap ratio to $2\Delta_0/(k_B T_c) \approx 3.0$, in line with results obtained on other T'-compound thin-film GBJs, where $2\Delta_0/(k_B T_c) \approx 2.8-3.5$[156,184].
For a d-wave order parameter, we would have expected ZBCPs which, however, were absent in the QP tunneling spectra. This could be due to a suppression, e.g. by strong disorder at the barrier, or due to an order parameter without sign change, such as s-wave.

To summarize, we fabricated the first IL GBJs and found both similar and different electric transport properties as compared to GBJs made of other cuprates. Regarding the order parameter symmetry of SLCO, some data suggested s-wave, whereas others suggested d-wave pairing. Finally, the results on SLCO GBJs created the base for further experiments, such as fabrication of SLCO tetracrystal SQUIDs, which will be the topic of the following chapter 4.

*A Fiske resonance is a resonant interaction of the Josephson ac current with a standing electromagnetic wave in the cavity of the Josephson junction.
A flux flow resonance occurs, when Josephson vortices are accelerated by a bias current-induced Lorentz force up to the phase velocity of electromagnetic waves in the Josephson junction.

Chapter 4

SLCO 0- and π-SQUID

4.1 Introduction

A class of phase-sensitive experiments allowing for a determination of the order parameter symmetry makes use of flux quantization in superconducting rings[185,186]. Due to phase coherence, a superconducting ring containing one π-junction* exhibits a frustrated ground state of the wave function with a finite circulating supercurrent, creating half a flux quantum ($\pm\Phi_0/2$). Crucial to the development of a π-junction is the sign change of the order parameter. Consequently, the observation of the half-flux-quantum effect in such rings directly implies the existence of a π-junction and unambiguously implies unconventional order parameter symmetry. Wollman *et al.* fabricated the first π-SQUID, a $YBa_2Cu_3O_7$- Pb corner SQUID, which is a superconducting loop comprising one π-junction and one conventional junction (0-junction)[38]. The half-flux-quantum effect was sensed by electric transport measurements, yielding d-wave pairing in $YBa_2Cu_3O_7$. Tsuei *et al.* followed this idea and fabricated an epitaxial tricrystalline $YBa_2Cu_3O_7$ring, comprising two grain boundary 0-junctions and one π-junction[39]. For that purpose, $YBa_2Cu_3O_7$was grown epitaxially on a designed misoriented tricrystalline $SrTiO_3$ substrate, resulting in a frustrated ground state and creating half a flux quantum within the tricrystalline ring. They used scanning SQUID microscopy to image the half flux quantum and prove d-wave pairing both in hole-doped[39,187–190] and electron-doped[161] cuprates. Based on the same idea[191], other groups fabricated grain boundary π-SQUIDs on tetracrystalline substrates, both with hole-doped[192,193] and electron-doped cuprates[194]. As for tricrystalline rings, the geometry involved is designed to be frustrated for d-wave pairing, i.e. the SQUID loop comprises one 0-junction and one π-junction if the order parameter has d-wave symmetry. So far, all experiments based upon the idea of flux quantization in superconducting rings yielded d-wave order parameter symmetry for the cuprates and set an upper limit for a possible s-wave contribution to a few percent. However, regarding electron-doped cuprates, only T'-compounds[161,192,194] but no IL compounds have been examined with this method; except for the present work, all experiments on IL compounds have only been performed on polycrystalline bulk material or single crystalline thin films, but no Josephson devices, such as GBJs or SQUIDs, have been fabricated. It is thus an issue to determine whether d-wave pairing is inherent to *all* cuprate superconductors or if their simplest member exhibits a different order parameter symmetry[58–67], underscoring the need for phase-sensitive experiments on the IL compounds.

*A π-junction exhibits an inherent phase jump of π in the ground state, corresponding to a negative critical current density $j_s = j_0 \sin(\delta + \pi) = -j_0 \sin(\delta)$.

4.2 Summary of manuscript in preparation

In this section we present data of a manuscript in preparation.

J. Tomaschko, V. Leca, J. Nagel, T. Selistrovski, R. Kleiner, and D. Koelle, *Phase-sensitive evidence for $d_{x^2-y^2}$-wave order parameter symmetry in the parent structure of high-T_c cuprate superconductors $Sr_{1-x}La_xCuO_2$*

Using the same technique as presented in chapter 1, we fabricated SLCO dc SQUIDs on BTO-buffered STO tetracrystals. The tetracrystal contains three identical 30 ° [001]-tilt symmetric grain boundaries and a fourth grain boundary with misorientation angle $\vartheta = 0\,°$, as shown in Fig. 4.1. The thickness of the BTO buffer layer is 25 nm and the thickness of the SLCO film is 22 nm. Additionally, a 10 nm thick gold layer was evaporated in-situ, protecting SLCO from degradation and acting as resistive shunt for the GBJs. The midpoint of the resistive transition was $T_c = 17.5\,\mathrm{K}$ and the transition width was $\Delta T_c = 1\,\mathrm{K}$. The film was patterned by photolithography and Argon ion milling to form the SQUID structures schematically shown in Fig. 4.1. Both SQUIDs have identical geometries but are tilted by 30 ° with respect to each other. The left hand SQUID was patterned such that its two junctions are formed only along a single grain boundary. Its junctions have a width of $w = 50\,\mu\mathrm{m}$, whereas the junctions of the right hand SQUID have a width of $w = 50\,\mu\mathrm{m}/\cos(30\,°) = 58\,\mu\mathrm{m}$. The area of the rectangular hole is $A = 50\,\mu\mathrm{m} \times 75\,\mu\mathrm{m}$ in both cases. The hole of the right hand SQUID in Fig. 4.1 contains the tetracrystal point. Since the junctions along grain boundaries 1 and 4 are much wider ($\sim 1\,\mathrm{mm}$) than those along 2 and 3, the former ones do not play an active role. Furthermore, grain boundary 4 is not a Josephson junction because its misorientation angle is $\vartheta = 0\,°$. Thus, the two active junctions of the right hand SQUID are located at grain boundaries 2 and 3.
The crystallographic orientations of the tetracrystal were chosen to form a frustrated ground state for the right hand SQUID if the superconductor is a *d*-wave superconductor. In this case, one of the two active junctions is a π-junction, as indicated by the lobes of the potential *d*-wave order parameter in Fig. 4.1; we therefore refer

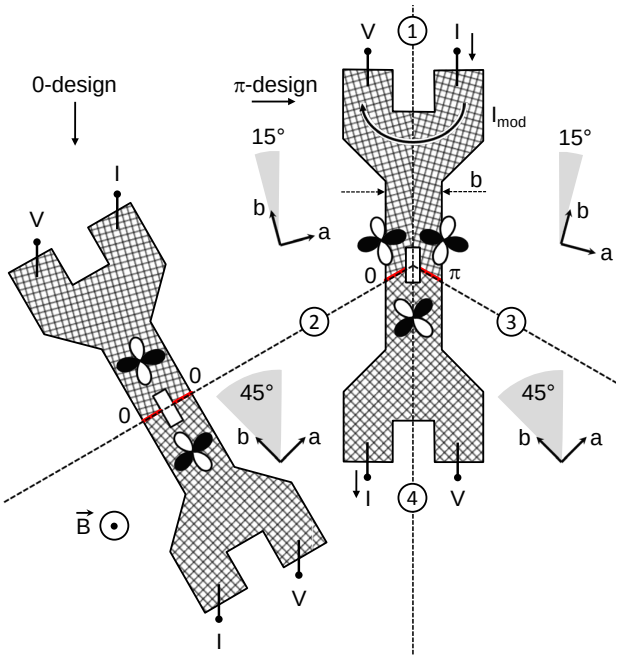

Figure 4.1: Schematic layout of the investigated SQUIDs. The π-design SQUID comprises four grain boundaries (dashed lines, 1-4). The misorientation angle of grain boundary 4 is $\vartheta = 0\,°$. The other grain boundaries are 30 ° [001]-tilt symmetric. The 0-design SQUID comprises a single grain boundary. Current I and voltage V pads are indicated. The lobes of a potential *d*-wave order parameter are also shown, where sign change is indicated by black and white.

to this SQUID as the π-design SQUID. In the case of an s-wave superconductor, this SQUID is a conventional SQUID. The left hand SQUID is made such that a conventional SQUID is formed for both d-wave and s-wave pairing; we therefore refer to this SQUID as the 0-design SQUID. Actually, two such 0-design SQUIDs were patterned, both yielding consistent data. For simplicity, we only present data of one 0-design SQUID.

Electric transport measurements were performed in a four-point configuration, with the sample mounted inside a noise-filtered and radio frequency shielded probe in a liquid-helium dewar. Magnetic μ-metal shielding yielded a background magnetic field $\mu_0 H_0 \approx 10\,\mathrm{nT}$, as described below. A SQUID amplifier was used to allow for low-noise measurements with voltage noise $S_V^{1/2} \approx 100\,\mathrm{pV}/\sqrt{\mathrm{Hz}}$. Magnetic fields were applied along the [001]-direction, i.e. perpendicular to the film plane.
On the left hand side of Fig. 4.2, typical current I vs voltage V curves are shown for two different values of an applied magnetic field, for the π-design [Fig. 4.2 (a)] and for the 0-design SQUID [Fig. 4.2 (c)]. On the right hand side of Fig. 4.2, the corresponding simulations including thermal noise are shown, yielding good agreement with the measured data. Note, that in Fig. 4.2 (b) an intrinsic phase difference $\delta\varphi = \pi$ between the two junctions was used for simulation. For the π-design SQUID, the unperturbed critical current per junction was determined as $I_0 = 12.0\,\mu\mathrm{A}$, corre-

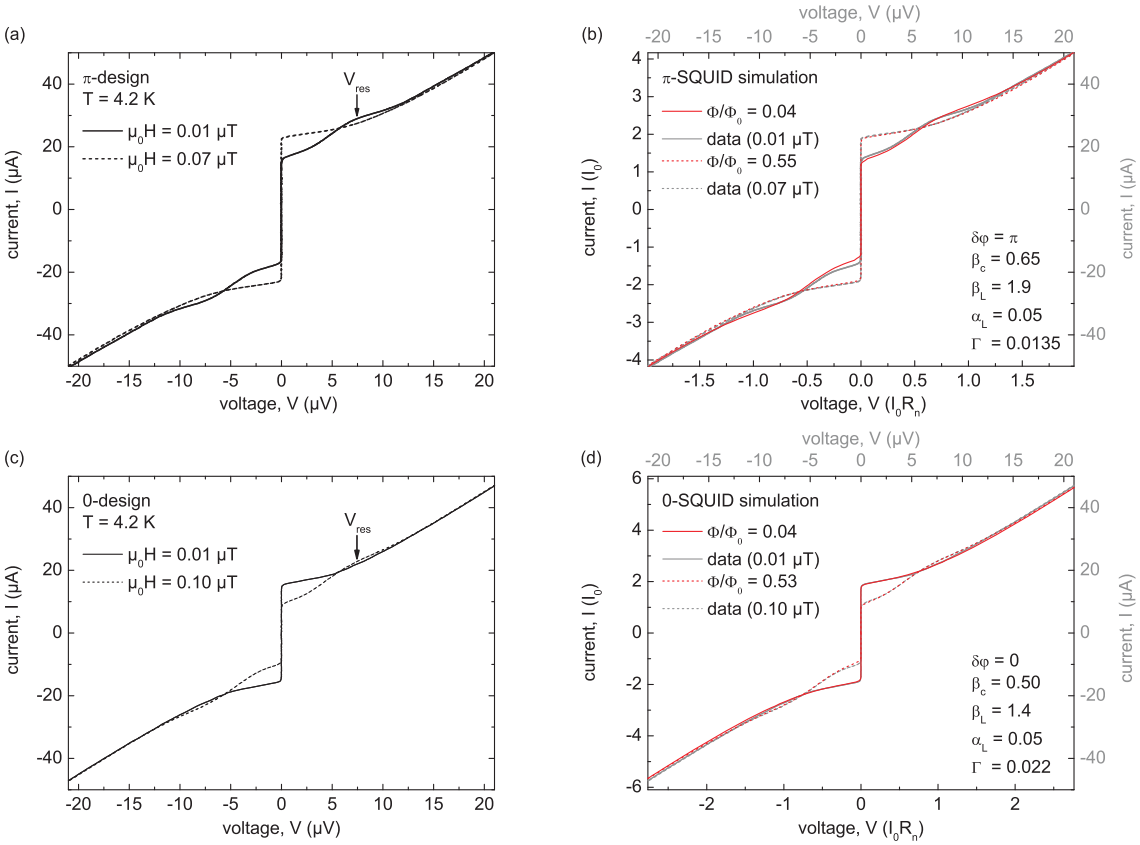

Figure 4.2: Left images show current I vs voltage V of the π-design (a) and 0-design SQUID (c) measured at $T = 4.2\,\mathrm{K}$ for an applied field $\mu_0 H = 0.01\,\mu\mathrm{T}$ that cancels out the background field and hence minimizes or maximizes the critical current (solid lines), and for the smallest magnetic field that causes a maximum or minimum of the critical current (dashed lines). Right images show corresponding simulations of $I(V)$ curves for a π-SQUID (b) and for a 0-SQUID (d). Measured data is superimposed as gray curves.

sponding to a critical current density $j_0 = 0.94\,\mathrm{kA/cm^2}$. The characteristic voltage was found to be $V_c \equiv I_0 R_n = 10.6\,\mu\mathrm{V}$, i.e. the normal state resistance of the Josephson junctions was $R_n = 0.88\,\Omega$. The Stewart–McCumber damping parameter was determined as $\beta_c \equiv 2\pi I_0 R_n^2 C/\Phi_0 = 0.65$, i.e. the Josephson junctions are overdamped and have a capacitance $C = 23\,\mathrm{pF}$. The inductance parameter was determined as $\beta_L \equiv 2LI_0/\Phi_0 = 1.9$, yielding an inductance $L \approx 160\,\mathrm{pH}$. The inductance asymmetry parameter[195] was determined as $\alpha_L = 0.05$. For the 0-design SQUID, the simulation yielded $I_0 = 8.2\,\mu\mathrm{A}$, $j_0 = 0.75\,\mathrm{kA/cm^2}$, $V_c = 7.6\,\mu\mathrm{V}$, $R_n = 0.93\,\Omega$, $\beta_c = 0.50$, $C = 23\,\mathrm{pF}$, $\beta_L = 1.4$, $L = 180\,\mathrm{pH}$, and $\alpha_L = 0.05$. The broad resonances centered at $V_{\mathrm{res}} \approx 7.0\,\mu\mathrm{V}$ and $7.5\,\mu\mathrm{V}$ for the π-design and for the 0-design SQUID, respectively, will be discussed later.

On the left hand side of Fig. 4.3, the critical current I_c vs magnetic field $\mu_0 H$ at $T = 4.2\,\mathrm{K}$ is shown for the π-design [Fig. 4.3 (a)] and for the 0-design SQUID [Fig. 4.3 (c)]. The very low voltage noise of the SQUID amplifier allowed to use a voltage criterion $V_c = 50\,\mathrm{nV}$. The simulations on the right hand side of Fig. 4.3 were performed with the same parameters as used for $I(V)$ simulations in Fig. 4.2 and show good agreement with the measured data. For the π-design SQUID, an abrupt deviation between simulated and measured data is visible at finite magnetic fields (see inset of Fig. 4.3 (b)), which will be discussed at the end of this section. Note, that for the π-design SQUID an intrinsic phase difference $\delta\varphi = \pi$ between the two junctions was used for simulation, whereas for the 0-design SQUID no such phase dif-

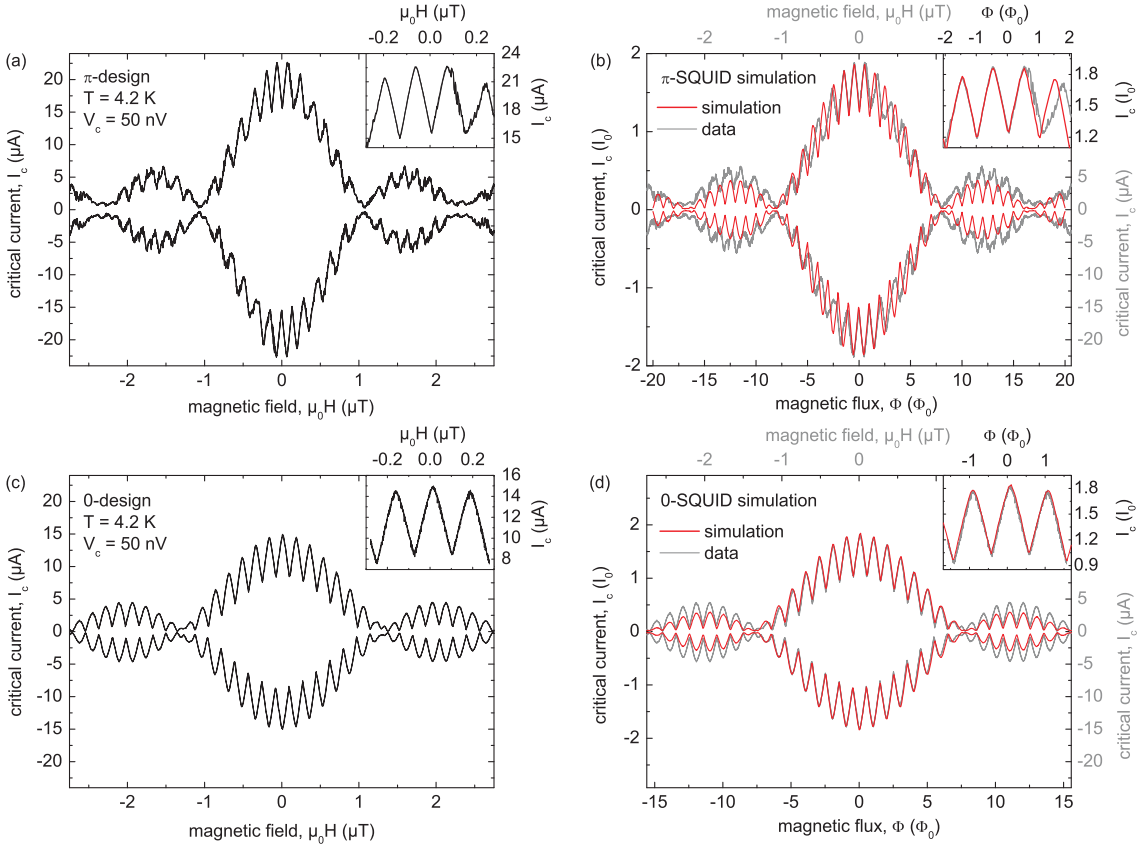

Figure 4.3: Left images show critical current I_c vs magnetic field H of the π-design (a) and 0-design SQUID (c) measured at $T = 4.2\,\mathrm{K}$ with voltage criterion $V_c = 50\,\mathrm{nV}$. Insets show an expanded view of the zero-field minimum and maximum. Right images show corresponding simulations of $I(V)$ curves for a π-SQUID (b) and for a 0-SQUID (d) with parameters as given in Fig. 4.2. Measured data is superimposed as gray curves.

ference was used. From the SQUID oscillation period $\mu_0 \Delta H = \Phi_0/A_{\text{eff}} = 0.133\,\mu\text{T}$ (π-design) and $0.176\,\mu\text{T}$ (0-design), the flux focusing factors were calculated as $F \equiv A_{\text{eff}}/A = 4.1$ and 3.1, where A_{eff} denotes the effective SQUID hole area. The oscillation period of the sinc-shaped envelope (which is due to the finite width of the Josephson junctions) was determined as $\mu_0 \Delta H \approx 1.1\,\mu\text{T}$ for the π-design and $\sim 1.4\,\mu\text{T}$ for the 0-design SQUID, which is in good agreement with theoretical values including flux focusing in thin films ($\mu_0 \Delta H = 1.84\Phi_0/w^2 = 1.13\,\mu\text{T}$ and $1.52\,\mu\text{T}$, respectively)[178]. A remarkable difference between the $I_c(H)$ patterns of the two SQUIDs is visible at approximately zero magnetic field: whereas the π-design SQUID exhibits an unconventional minimum of $I_c(H)$ at zero field, the 0-design SQUID exhibits a maximum (see also insets in Fig. 4.3 (a) and (c)). Such a behavior is indicative for a superconductor with *d*-wave order parameter symmetry, as previously demonstrated by similar experiments on other cuprates[192–194].

We next show that this unconventional behavior was not mimicked by a shift of the SQUID oscillation pattern along the magnetic field axis due to background fields, trapped flux, or asymmetries of the SQUID. From the symmetry axis of the sinc-shaped envelope of the $I_c(H)$ patterns, the background field is determined as $\mu_0 H_0 \approx 10\,\text{nT}$ for both SQUIDs[196]. As the minimum of the π-design SQUID oscillation pattern is also centered at this specific field value, the background field can be excluded as a possible origin for the unconventional behavior. Regarding trapped flux, both observed $I_c(H)$ dependencies could only be explained by the following scenario: During *any* cooling cycle, *exactly* $\Phi = (2n+1)\Phi_0/2$ has to be sensed by A_{eff} of the π-design SQUID and *exactly* $\Phi = n\Phi_0$ has to be sensed by A_{eff} of the 0-design

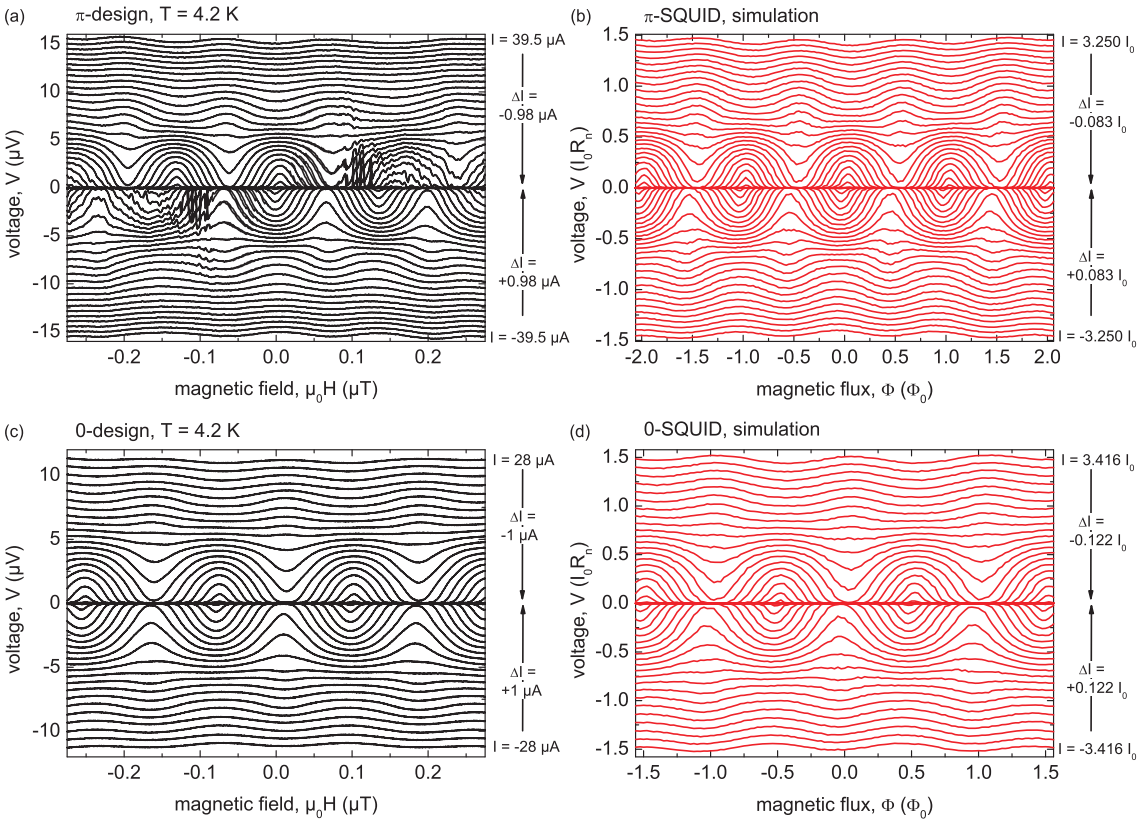

Figure 4.4: Left images show voltage V vs magnetic field H of the π-design (a) and 0-design SQUID (c) measured at $T = 4.2\,\text{K}$ for different bias currents I. Right images show corresponding simulations of $V(\Phi)$ curves for a π-SQUID (b) and for a 0-SQUID (d) with parameters as given in Fig. 4.2.

SQUID ($n \in \mathbb{N}$), *and* the Josephson junctions of both SQUIDs have to be free from flux. This scenario appears extremely unlikely and we also mention that after numerous thermal cycles the $I_c(H)$ patterns of both SQUIDs were always identical (except for small variations of the background field $\mu_0 \Delta H_0 \approx \pm 10\,\mathrm{nT}$), while trapped flux should lead to remarkable deviations of the $I_c(H)$ patterns from run to run. We thus conclude that trapped flux does not account for the observed unusual $I_c(H)$ dependence of the π-design SQUID. Finally, we can also exclude SQUID asymmetries as possible origin. As mentioned above, the inductance asymmetry parameter was determined as $\alpha_L = 0.05$, which is too small to shift the SQUID oscillation pattern of the π-design SQUID by half a period. Furthermore, the current asymmetry α_I, the resistance asymmetry α_R, and the capacitance asymmetry α_C [195] were found to be close to zero, as shown by simulation of a set of $V(\Phi)$ curves (see Fig. 4.4).
To summarize, extrinsic effects can be excluded as possible origin for the observed zero-field minimum in the $I_c(H)$ curve of the π-design SQUID. Thus, it is concluded that the intrinsic phase difference $\delta\varphi = \pi$ inherent to d-wave order parameter symmetry accounts for the abovementioned observation. This implies predominant d-wave order parameter symmetry of SLCO.

We next turn to the resonances visible in the $I(V)$ curves of Fig. 4.2. An LC resonance of the SQUID loop can be excited by the ac Josephson currents if the Josephson frequency $f_J \equiv V/\Phi_0$ matches the resonance frequency of the SQUID

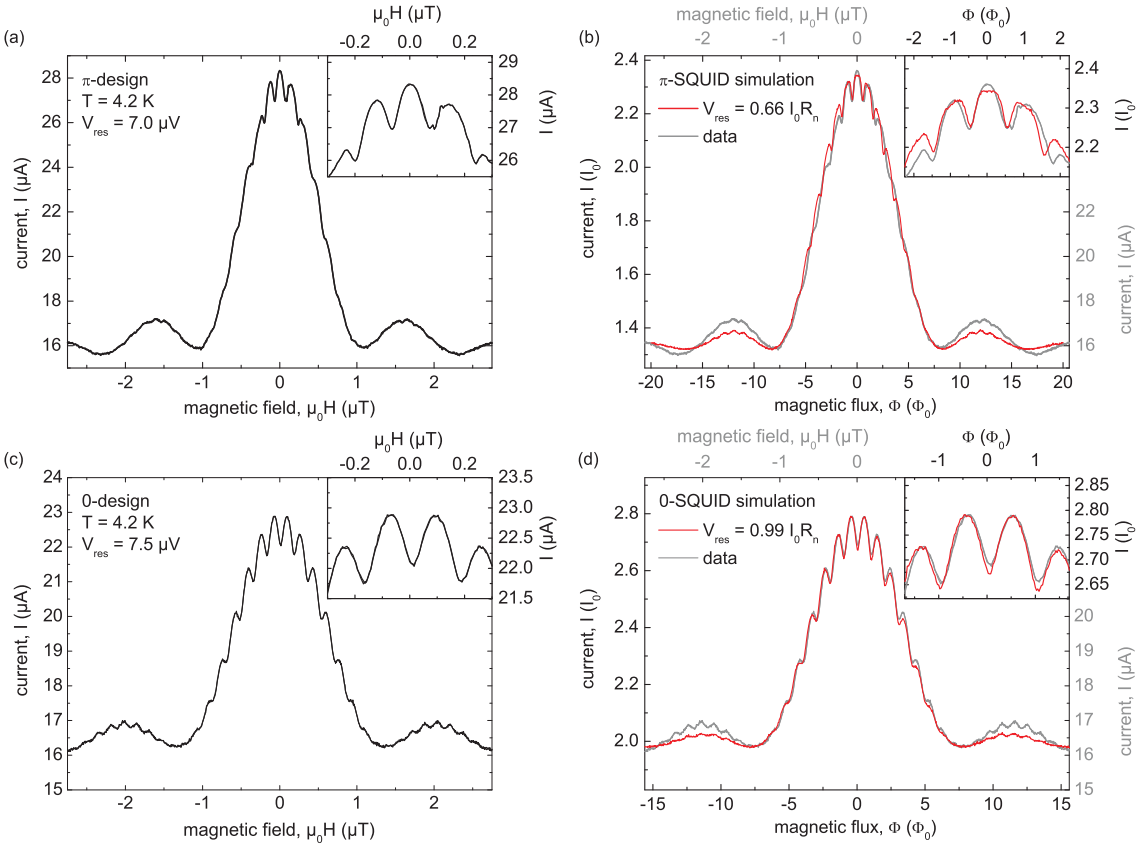

Figure 4.5: Left images show current I vs magnetic field H of the π-design (a) and 0-design SQUID (c) measured at $T = 4.2\,\mathrm{K}$ at the voltage V_{res} of the LS resonance. Insets show an expanded view of the zero-field maximum or minimum. Right images show corresponding simulations of $I(\Phi)$ curves for a π-SQUID (b) and for a 0-SQUID (d) with parameters as given in Fig. 4.2. Measured data is superimposed as gray curves.

loop $f_{\mathrm{res}} \equiv 1/(2\pi\sqrt{LC/2})$[195]. By using the simulated values for L and C, we expect a resonance at $V = 7.6\,\mu$V for the π-design and at $7.3\,\mu$V for the 0-design SQUID, which agrees well with the observed resonance voltages $V_{\mathrm{res}} \approx 7.0\,\mu$V and $7.5\,\mu$V, respectively. For a π-SQUID, the two Josephson junctions oscillate out-of-phase at zero magnetic field (due to the intrisic phase difference $\delta\varphi = \pi$) and are likely to excite the LC resonance, whereas weak coupling occurs when the junctions oscillate in-phase, as for external flux $\Phi = \Phi_0/2$. The opposite behavior is expected for a 0-SQUID due to the lack of an intrinsic phase difference ($\delta\varphi = 0$)[196,197]. As reported for tetracrystal $YBa_2Cu_3O_7$ π-SQUIDs and 0-SQUIDs before[193], we observed corresponding behavior in the SLCO π-design and 0-design SQUID, in accordance with the interpretation that the former is a π-SQUID and the latter a 0-SQUID (see Fig. 4.5). Note, that the unconventional magnetic-field dependence of the LC resonance of a π-SQUID is a proof that the phase shift of π is maintained in the dissipative voltage state of the junctions[193].

Finally, we discuss the small discontinuities visible in $I_c(H)$ and $V(H)$ curves of the π-design SQUID. The smallest magnetic field value at which a discontinuity occurs is denoted as $\mu_0 H_d$. As sketched in Fig. 4.1, the upper SQUID loop comprises an additional 30° GBJ, which does not play an active role for the functionality of the SQUID due to its large dimension ($w \approx 1.7\,$mm). In the following, we demonstrate that Josephson vortices entering or leaving this grain boundary (GB1) are responsible for the discontinuities.
According to literature, penetration of a Josephson vortex into a Josephson junction becomes favorable beginning at a certain field value $\mu_0 H_{c1} = 2\Phi_0/(\pi^2 \lambda_J d)$, where λ_J is the Josephson penetration depth and d the effective magnetic thickness of the barrier[198]. Measurements on SLCO GBJs with various widths w (not shown here) yielded deviation from short-junction behavior for $w \gtrsim 50\,\mu$m, thus, we estimate $\lambda_J \approx 20\,\mu$m. In the thin film limit, $d \approx 2\Lambda$, where $\Lambda = \lambda_L^2/t$ is the Pearl length, t the film thickness, and λ_L the London penetration depth. With the literature value $\lambda_L \approx 0.7\,\mu$m[67] and the actual film thickness $t = 22\,$nm, we calculate $d \approx 45\,\mu$m and $\mu_0 H_{c1} \approx 0.5\,\mu$T. We further estimate the flux focusing factor as $F \approx (b/2)/(2\Lambda) \approx 1.7$, where $b = 150\,\mu$m is the width of the current-voltage lead comprising GB1 (see Fig. 4.1) and calculate the expected penetration field as $\mu_0 H_{c1} F \approx 0.3\,\mu$T, which is in fair agreement with the measured value $\mu_0 H_d \approx 0.1\,\mu$T. Since an abrupt movement of a vortex is detected by the SQUID as an abrupt change of flux, we thus interpret the first discontinuity at $\mu_0 H_d$ as entering of a Josephson vortex into GB1.
Moreover, $j_c(H)$ patterns are highly point symmetric with respect to the origin (dis-

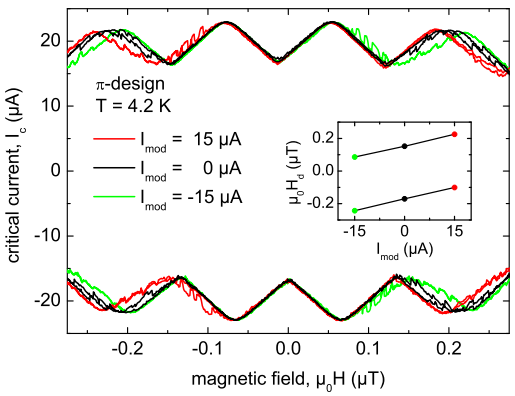

Figure 4.6: $I_c(H)$ curves of the π-design SQUID for different values of a constant modulation current I_{mod} across grain boundary 1. Inset shows the smallest magnetic field value $\mu_0 H_d$ at which a discontinuity in $I_c(H)$ occurs versus I_{mod}.

regarding the small background field) and no hysteresis is visible within the central minimum of $j_c(H)$. We can explain both observations by Josephson vortices which enter GB1 when $\mu_0 H$ exceeds $\mu_0 H_d$ and which are not pinned. In this case, the vortices change polarity when $\mu_0 H$ is reversed, in accordance with point symmetry, and they leave GB1 when $\mu_0 H$ falls below $\mu_0 H_d$, in accordance with non-hysteretic behavior.
Finally, we additionally biased GB1 with a constant current, called modulation current I_{mod} (see Fig. 4.1), and simultaneously measured $I_c(H)$ of the SQUID. We found that I_{mod} had a strong impact on the discontinuities, as depicted in Fig. 4.6. By applying I_{mod}, $I_c(H)$ patterns lost point symmetry and exhibited a pronounced mirror symmetry with respect to the magnetic field axis. This symmetry is explained as follows: For $\mu_0 H < \mu_0 H_d$, GB1 does not contain any vortices, however, a circulating current is present due to the diamagnetic behavior of the junction. The circulating current crosses GB1 at the lower edge of the junction (close to the SQUID hole) and at the upper edge (close to the pads). Since the junction is very long, I_{mod} probably crosses GB1 mainly at the upper edge of the junction. If I_{mod} was applied parallel (antiparallel) to the diamagnetic current across the upper part of the junction, penetration of a Josephson vortex was enhanced (hindered), resulting in a decrease (increase) of $|\mu_0 H_d|$. Note, that the diamagnetic current changes polarity upon reversing the magnetic field, explaining the mirror symmetry of $I_c(H)$ for finite I_{mod}.
To summarize, from the absolute value of $\mu_0 H_d$ and symmetry considerations of $I_c(H)$ with and without I_{mod}, we demonstrated that the observed discontinuities can be traced back to Josephson vortices entering (leaving) GB1 when $\mu_0 H$ exceeds (falls below) $\mu_0 H_d$. Note, that the zero-field minimum was a robust feature of *all* $I_c(H)$ curves, which was neither affected by discontinuities nor by modulation currents up to $100\,\mu$A (not shown here). Thus, Josephson vortices within GB1 can be excluded as a possible origin for the observed zero-field minimum of $I_c(H)$ and we are lead to the conclusion that the order parameter of SLCO has a dominant d-wave symmetry.

Summary and outlook

In the framework of this thesis, we present studies on the order parameter symmetry of the parent structure of high-T_c cuprate superconductors, the electron-doped infinite layer compound $Sr_{1-x}La_xCuO_2$ (SLCO). The work was motivated by the facts that SLCO has the simplest crystal structure of all cuprate superconductors and that SLCO belongs to the minor group of electron-doped cuprates. Since the pairing mechanism of high-T_c superconductors has not been revealed yet, both aspects are of fundamental importance: the simplicity of the crystal structure allows to exclude secondary effects in advance and to explore inherent properties of cuprate superconductors, and the fact that SLCO is electron-doped allows to compare it to its hole-doped counterparts, particularly with regard to the question of a common pairing mechanism. For these studies, four types of samples were fabricated, SLCO thin films, planar SLCO/gold/niobium tunnel junctions, SLCO grain boundary Josephson junctions, and an SLCO tetracrystal SQUID.

Since **SLCO thin films** form the base for various experiments, a reproducible fabrication process had to be established initially. The process described yielded SLCO films with high crystalline quality and robust superconducting properties (maximum $T_c = 22\,\mathrm{K}$). Pulsed laser deposition was used to grow films on two kinds of substrates, potassium tantalate (KTO) and strontium titanate (STO). KTO was chosen due to its large in-plane lattice constant, allowing to grow tensile strained SLCO films, promoting electron-doping of the CuO_2 planes. However, since no bi-, tri-, or tetracrystalline KTO substrates are available, STO was chosen as alternative. Prior to deposition of SLCO on STO, a barium titanate (BTO) buffer layer had to be deposited to compensate for the small in-plane lattice constant of STO. To induce superconductivity in the as-deposited SLCO films, they had to be annealed under reducing conditions, as described in detail. The main issue was to remove interstitial excess oxygen from the Sr/La planes without reducing the CuO_2 planes. Finally, a study of the influence of various process parameters on the final thin film properties was presented.
To increase T_c even further, a more reactive process gas, such as nitrous oxide (N_2O) or ozone (O_3) could help. Such gas would allow to oxidize the CuO_2 planes at substantially lower working pressure, which is known to enhance the crystalline quality of thin film samples. Furthermore, the choice of buffer layers with lattice constants close to that of bulk SLCO could help to reduce strain effects and thus to improve the structural quality and superconducting properties. For that purpose, barium strontium titanate ($Ba_{0.5}Sr_{0.5}TiO_3$) could serve. It has an in-plane lattice constant matching that of bulk SLCO and has already been deposited epitaxially on STO [199].

Motivated by the question whether c-axis tunnel currents could pass from SLCO into a conventional superconductor, **planar SLCO/Au/Nb tunnel junctions** were prepared in an in-situ trilayer process. Substantial c-axis supercurrents would

have served as evidence for a finite s-wave contribution to the order parameter of SLCO, however, no such current was observed. To check if the supercurrent was suppressed extrinsically, e.g. by a degraded surface of SLCO, x-ray photoelectron spectroscopy and x-ray Auger-electron spectroscopy on SLCO thin film reference samples were performed additionally. Thereby, a reduced copper species in the uppermost layer of SLCO was identified, indicative of a non-superconducting surface, explaining the absence of c-axis supercurrents in the planar tunnel junctions. As a consequence, an s-wave component of the order parameter of SLCO could not be excluded from the transport measurements because potential c-axis supercurrents would have been suppressed by the reduced surface layer. However, it was pointed out that the post-deposition reduction step, which is an integral part of the fabrication of all kinds of electron-doped cuprates, induces the formation of a degraded, non-superconducting surface, which is an important technological aspect, especially with regard to the application of superconductors in integrated circuits.
To induce superconductivity in the surface layer of SLCO as well, the reduced copper species has to be reoxidized. For that purpose, the vacuum annealed samples could be exposed to oxygen for a short period at moderate temperature, so that only the surface layer is oxidized but the rest of the film is unaffected. With this method, it is promising to fabricate planar tunnel junctions that can provide information on a potential s-wave component of the order parameter of SLCO.

To examine the superconducting gap of SLCO as well as potential signatures of d-wave pairing, so-called Andreev bound states (ABSs), **SLCO grain boundary Josephson junctions** (GBJs) were fabricated on BTO-buffered STO bicrystals and used for tunneling spectroscopy. No ABSs were visible in the quasiparticle (QP) tunneling spectra, which could be a signature of s-wave pairing. However, the possibility that ABSs had been suppressed by extrinsic reasons, such as oxygen vacancies at the GBJs, was discussed. Thus, the possibility of d-wave pairing was not excluded. Moreover, QP tunneling spectra revealed a V-shaped gap, which was most pronounced for lowest temperatures, suggesting that nodes are present in the order parameter of SLCO, as usually observed for d-wave superconductors. Besides QP tunneling, Cooper pair (CP) tunneling was examined at various temperatures and magnetic fields. An extraordinary high critical current density was observed. A remarkably regular modulation pattern of the critical current vs magnetic field implied homogeneous current distribution across the junctions, as usually observed for s-wave superconductors. However, regarding d-wave pairing, this observation could also be explained if the grain boundary was unfaceted. Finally, Fiske and flux flow resonances, as well as thermally activated phase slippage were observed, demonstrating the proper operation of the grain boundaries as Josephson junctions. In conclusion, both hints for s-wave and d-wave pairing have been found. However, aspects promoting s-wave symmetry could also be explained by extrinsic effects, in contrast to the observed V-shaped gap, promoting d-wave symmetry. It is possible that improved SLCO GBJs will exhibit ABSs in their tunneling spectra, which would verify d-wave pairing. For that purpose, samples with increased T_c and/or improved quality of the crystal structure at the grain boundary have to be synthesized.

To perform a phase-sensitive test of the order parameter symmetry of SLCO, an **SLCO tetracrystal superconducting quantum interference device** (SQUID) was fabricated. The crystallographic orientations of the tetracrystalline STO substrate were chosen to form a frustrated ground state of the wave function in the

SQUID if SLCO was a d-wave superconductor. An unconventional magnetic field dependence of the critical current gave strong evidence for a frustrated ground state and it was pointed out that this behavior was not mimicked by extrinsic effects, such as background magnetic fields, trapped magnetic flux, or SQUID asymmetries. These facts imply that a phase shift of π was induced intrinsically, i.e. that the SQUID was a π-SQUID with one 0-junction and one π-junction, consistent with a predominant $d_{x^2-y^2}$-wave order parameter symmetry of SLCO.
As a complementary experiment, the SQUID could be imaged by means of low-temperature scanning electron microscopy (LTSEM). On the one hand, the current density of Josephson junctions can be imaged by LTSEM. Thus, in the ground state of the SQUID, a negative critical current density should be observed for the π-junction and a positive for the 0-junction. On the other hand, LTSEM is able to image single vortices. Thus, LTSEM could help to verify that there are no votices in the vicinity of the SQUID hole and junctions which could mimick an unconventional magnetic field dependence of the critical current.

Bibliography

[1] H. Kamerlingh-Onnes. Further experiments with liquid helium. On the change of electric resistance of pure metals at very low temperatures. The disappearance of the resistance of mercury. *Comm. Phys. Lab. Univ. Leiden*, 122b, 1911. 1

[2] W. Meissner and R. Ochsenfeld. Ein neuer Effekt bei Eintritt der Supraleitfähigkeit. *Naturwiss.*, 21:787–788, 1933. 1

[3] F. London and H. London. The Electromagnetic Equations of the Supraconductor. *Proc. R. Soc. Lond. A*, 149:71–88, 1935. 1

[4] L. V. Shubnikov, V. I. Khotkevich, Yu. D. Shepelev, and Yu. N. Riabinin. *Zh. Eksp. Teor. Fiz.*, 7:221–237, 1937. 1

[5] L. V. Shubnikov, V. I. Khotkevich, Yu. D. Shepelev, and Yu. N. Riabinin. Magnetic properties of superconducting metals and alloys. *Ukr. J. Phys.*, 53:42–52, 2008. 1

[6] V. L. Ginzburg and L. D. Landau. On the Theory of superconductivity. *Zh. Eksp. Teor. Fiz.*, 20:1064–1082, 1950. 1

[7] L. D. Landau. *Phys. Z. Sowjet.*, 11:545, 1937. 1

[8] A. A. Abrikosov. On the Magnetic Properties of Superconductors of the Second Group. *Sov. Phys. JETP*, 5:1174–1182, 1957. 1

[9] J. Bardeen, L. N. Cooper, and J. R. Schrieffer. Theory of Superconductivity. *Phys. Rev.*, 108:1175–1204, 1957. 1

[10] L. N. Cooper. Bound Electron Pairs in a Degenerate Fermi Gas. *Phys. Rev.*, 104:1189–1190, 1956. 2

[11] H. Fröhlich. Theory of the Superconducting State. I. The Ground State at the Absolute Zero of Temperature. *Phys. Rev.*, 79:845–856, 1950. 2

[12] J. Bardeen. Wave Functions for Superconducting Electrons. *Phys. Rev.*, 80:567–574, 1950. 2

[13] E. Maxwell. Isotope Effect in the Superconductivity of Mercury. *Phys. Rev.*, 78:477–477, 1950. 2

[14] C. A. Reynolds, B. Serin, W. H. Wright, and L. B. Nesbitt. Superconductivity of Isotopes of Mercury. *Phys. Rev.*, 78:487–487, 1950. 2

[15] L. P. Gor'kov. Microscopic Derivation of the Ginzburg-Landau Equations in the Theory of Superconductivity. *Sov. Phys. JETP*, 9:1364–1367, 1959. 2

[16] C. C. Tsuei and J. R. Kirtley. Pairing symmetry in cuprate superconductors. *Rev. Mod. Phys.*, 72:969–1016, 2000. 2, 3, 13

[17] F. Steglich, J. Aarts, C. D. Bredl, W. Lieke, D. Meschede, W. Franz, and H. Schäfer. Superconductivity in the Presence of Strong Pauli Paramagnetism: $CeCu_2Si_2$. *Phys. Rev. Lett.*, 43:1892–1896, 1979. 2

[18] J. G. Bednorz and K. A. Müller. Possible High T_c Superconductivity in the Ba-La-Cu-O System. *Z. Phys. B*, 64:189–193, 1986. 2, 5

[19] Y. Kamihara, T. Watanabe, M. Hirano, and H. Hosono. Iron-Based Layered Superconductor $La[O_{1-x}F_x]FeAs$ ($x = 0.05 - 0.12$) with $T_c = 26\,\mathrm{K}$. *J. Am. Chem. Soc.*, 130:3296–3297, 2008. 2

[20] C. Petrovic, P. G. Pagliuso, M. F. Hundley, R. Movshovich, J. L. Sarrao, J. D. Thompson, Z. Fisk, and P. Monthoux. Heavy-fermion superconductivity in $CeCoIn_5$ at 2.3 K. *J. Phys.: Condens. Matter*, 13:L337–L342, 2001. 2

[21] C. W. Chu, L. Gao, F. Chen, Z. J. Huang, R. L. Meng, and Y. Y. Xue. Superconductivity above 150 K in $HgBa_2Ca_2Cu_3O_{8+\delta}$ at high pressures. *Nature*, 365:323–325, 1993. 2

[22] Z.-A. Ren, G.-C. Che, X.-L. Dong, J. Yang, W. Lu, W. Yi, X.-L. Shen, Z.-C. Li, L.-L. Sun, F. Zhou, and Z.-X. Zhao. Superconductivity and phase diagram in iron-based arsenic-oxides $ReFeAsO_{1-\delta}$ (Re = rare-earth metal) without fluorine doping. *Europhys. Lett.*, 83:17002, 2008. 2

[23] N. K. Sato, N. Aso, K. Miyake, R. Shiina, P. Thalmeier, G. Varelogiannis, C. Geibel, F. Steglich, P. Fulde, and T. KomatsubaraI. Strong coupling between local moments and superconducting 'heavy' electrons in UPd_2Al_3. *Nature*, 410:340–343, 2001. 2

[24] O. Stockert, J. arndt, E. Faulhaber, C. Geibel, H. S. Jeevan, S. Kirchner, M. Loewenhaupt, K. Schmalzl, W. Schmidt, Q. Si, and F. Steglich. Magnetically driven superconductivity in $CeCu_2Si_2$. *Nat. Phys.*, 7:119–124, 2011. 2

[25] P. W. Anderson. The Resonating Valence Bond State in La_2CuO_4 and Superconductivity. *Science*, 235:1196–1198, 1987. 2

[26] P. Monthoux and D. Pines. Spin-fluctuation-induced superconductivity and normal-state properties of $YBa_2Cu_3O_7$. *Phys. Rev. B*, 49:4261–4278, 1994.

[27] D. J. Scalapino. The case for $d_{x^2-y^2}$ pairing in the cuprate superconductors. *Phys. Rep.*, 250:329–365, 1995. 2

[28] J. Paglione and R. L. Greene. High-temperature superconductivity in iron-based materials. *Nature Physics*, 6:645–658, 2010. 2

[29] F. Wang and D.-H. Lee. The Electron-Pairing Mechanism of Iron-Based Superconductors. *Science*, 332:200–204, 2011. 2

[30] E. Fermi. Sulla quantizzazione del gas perfetto monoatomico. *Rendiconti Lincei*, 3:145–9, 1926. 2

[31] P. A. M. Dirac. On the Theory of Quantum Mechanics. *Proc. R. Soc. Lond. A*, 112:661–677, 1926.

[32] A. Zannoni. On the Quantization of the Monoatomic Ideal Gas. *arXiv:cond-mat [cond-mat.stat-mech]*, 9912229:12–14, 1999. 2

[33] Y. Maeno, H. Hashimoto, K. Yoshida, S. Nishizaki, T. Fujita, J. G. Bednorz, and F. Lichtenberg. Superconductivity in a layered perovskite without copper. *Nature*, 372:532, 1994. 2

[34] Y. Maeno, T. M. Rice, and M. Sigrist. The intriguing superconductivity of strontium ruthenate. *Physics Today*, 54:42–47, 2001.

[35] K. D. Nelson, Z. Q. Mao, Y. Maeno, and Y. Liu. Odd-Parity Superconductivity in Sr_2RuO_4. *Science*, 306:1151–1154, 2004. 2

[36] H. R. Ott, H. Rudigier, Z. Fisk, and J. L. Smith. UBe_{13}: An Unconventional Actinide Superconductor. *Phys. Rev. Lett.*, 50:1595–1598, 1983. 2

[37] H. R. Ott, F. Rudigier, T. M. Rice, K. Ueda, Z. Fisk, and J. L. Smith. p-Wave Superconductivity in UBe_{13}. *Phys. Rev. Lett.*, 52:1915–1918, 1984. 2

[38] D. A. Wollman, D. J. Van Harlingen, W. C. Lee, D. M. Ginsberg, and A. J. Leggett. Experimental determination of the superconducting pairing state in YBCO from the phase coherence of YBCO-Pb dc SQUIDs. *Phys. Rev. Lett.*, 71:2134–2137, 1993. 2, 17

[39] C. C. Tsuei, J. R. Kirtley, C. C. Chi, L. S. Yu-Jahnes, A. Gupta, T. Shaw, J. Z. Sun, and M. B. Ketchen. Pairing Symmetry and Flux Quantization in a Tricrystal Superconducting Ring of $YBa_2Cu_3O_{7-\delta}$. *Phys. Rev. Lett.*, 73:593–596, 1994. 17

[40] D. J. Van Harlingen. Phase-sensitive tests of the symmetry of the pairing state in the high-temperature superconductors – Evidence for $d_{x^2-y^2}$ symmetry. *Rev. Mod. Phys.*, 67:515–535, 1995. 2

[41] A. G. Sun, D. A. Gajewski, M. B. Maple, and R. C. Dynes. Observation of Josephson Pair Tunneling between a High-T_c Cuprate ($YBa_2Cu_3O_{7-\delta}$) and a Conventional Superconductor (Pb). *Phys. Rev. Lett.*, 72:2267–2270, 1994. 2, 10

[42] M. B. Walker and J. Luettmer-Strathmann. Josephson tunneling in high-T_c superconductors. *Phys. Rev. B*, 54:588–601, 1996. 2

[43] C. W. Hicks, T. M. Lippman, M. E. Huber, Z.-A. Ren, J. Yang, Z.-X. Zhao, and K. A. Moler. Limits on the Superconducting Order Parameter in $NdFeAsO_{1-x}F_y$ from Scanning SQUID Microscopy. *J. Phys. Soc. Jpn.*, 78:013708, 2008. 2

[44] X. Zhang, Y. S. Oh, Y. Liu, L. Yan, K. H. Kim, R. L. Greene, and I. Takeuchi. Observation of the Josephson Effect in $Pb/Ba_{1-x}K_xFe_2As_2$ Single Crystal Junctions. *Phys. Rev. Lett.*, 102:147002, 2009.

[45] C.-T. Chen, C. C. Tsuei, M. B. Ketchen, Z.-A. Ren, and Z. X. Zhao. Integer and half-integer flux-quantum transitions in a niobium–iron pnictide loop. *Nat. Phys.*, 6:260–264, 2010. 2

[46] I. I. Mazin, D. J. Singh, M. D. Johannes, and M. H. Du. Unconventional Superconductivity with a Sign Reversal in the Order Parameter of $LaFeAsO_{1-x}F_x$. *Phys. Rev. Lett.*, 101:057003, 2008. 2

[47] K. Kuroki, S. Onari, R. Arita, H. Usui, Y. Tanaka, H. Kontani, and H. Aoki. Unconventional Pairing Originating from the Disconnected Fermi Surfaces of Superconducting $LaFeAsO_{1-x}F_x$. *Phys. Rev. Lett.*, 101:087004, 2008.

[48] W.-Q. Chen, K.-Y. Yang, Y. Zhou, and F.-C. Zhang. Strong Coupling Theory for Superconducting Iron Pnictides. *Phys. Rev. Lett.*, 102:047006, 2009. 2

[49] H. Tou, Y. Kitaoka, K. Asayama, N. Kimura, Y. Onuki, E. Yamamoto, and K. Maezawa. Odd-Parity Superconductivity with Parallel Spin Pairing in UPt_3: Evidence from ^{195}Pt Knight Shift Study. *Phys. Rev. Lett.*, 77:1374–1377, 1996. 2

[50] C. Pfleiderer. Superconducting phases of f-electron compounds. *Rev. Mod. Phys.*, 81:1551–1624, 2009. 3

[51] M. R. Norman. The Challenge of Unconventional Superconductivity. *Science*, 332:196–200, 2011. 3

[52] A. Huxley and P. Rodière and D. McK. Paul and N. van Dijk and R. Cubitt and J. Flouquet. Realignment of the flux-line lattice by a change in the symmetry of superconductivity in UPt_3. *Nature*, 406:160–164, 2000. 3

[53] J. D. Strand, D. J. Van Harlingen, J. B. Kycia, and W. P. Halperin. Evidence for Complex Superconducting Order Parameter Symmetry in the Low-Temperature Phase of UPt_3 from Josephson Interferometry. *Phys. Rev. Lett.*, 103:197002, 2009. 3

[54] T. Siegrist, S. M. Zahurak, D. W. Murphy, and R. S. Roth. The parent structure of the layered high-temperature superconductors. *Nature*, 334:231–232, 1988. 3, 5

[55] F.-C. Hsu, J.-Y. Luo, K.-W. Yeh, T.-K. Chen, T.-W. Huang, P. M. Wu, Y.-C. Lee, Y.-L. Huang, Y.-Y. Chu, D.-C. Yan, and M.-K. Wu. Superconductivity in the PbO-type structure α-FeSe. *Proc. Natl. Acad. Sci. U.S.A.*, 105:14262–14264, 2008. 3

[56] G. Er, S. Kikkawa, F. Kanamaru, Y. Miyamoto, S. Tanaka, M. Sera, M. Sato, Z. Hiroi, M. Takano, and Y. Bando. Structural, electrical and magnetic studies of infinite-layered $Sr_{1-x}La_xCuO_2$ superconductor. *Physica C*, 196:271, 1992. 3, 5, 6, 7

[57] T. Hanaguri, S. Niitaka, K. Kuroki, and H. Takagi. Unconventional s-Wave Superconductivity in Fe(Se,Te). *Science*, 328:474–476, 2010. 3

[58] T. Imai, C. P. Slichter, J. L. Cobb, and J. T. Markert. Superconductivity and spin fluctuations in the electron-doped infinitely-layered high T_c superconductor $Sr_{0.9}La_{0.1}CuO_2$ ($T_c = 42\,\mathrm{K}$). *J. Phys. Chem. Solids*, 56:1921–1925, 1995. 3, 17

[59] C.-T. Chen, P. Seneor, N.-C. Yeh, R. P. Vasquez, L. D. Bell, C. U. Jung, J. Y. Kim, M.-S. Park, H.-J. Kim, and S.-I. Lee. Strongly Correlated s-Wave Superconductivity in the N-Type Infinite-Layer Cuprate. *Phys. Rev. Lett.*, 88:227002, 2002.

[60] G. V. M. Williams, R. Dupree, A. Howes, S. Krämer, H. J. Trodahl, C. U. Jung, Min-Seok Park, and Sung-Ik Lee. Gap anisotropy, spin fluctuations, and normal-state properties of the electron-doped superconductor $Sr_{0.9}La_{0.1}CuO_2$. *Phys. Rev. B*, 65:224520, 2002.

[61] V. S. Zapf, N.-C. Yeh, A. D. Beyer, C. R. Hughes, C. H. Mielke, N. Harrison, M. S. Park, K. H. Kim, and S.-I. Lee. Dimensionality of superconductivity and vortex dynamics in the infinite-layer cuprate $Sr_{0.9}M_{0.1}CuO_2$ (M=La,Gd). *Phys. Rev. B*, 71:134526, 2005.

[62] Z. Y. Liu, H. H. Wen, L. Shan, H. P. Yang, X. F. Lu, H. Gao, M.-S. Park, C. U. Jung, and S.-I. Lee. Bulk evidence for s-wave pairing symmetry in electron-doped infinite-layer cuprate $Sr_{0.9}La_{0.1}CuO_2$. *Europhys. Lett.*, 69:263–269, 2005.

[63] K. H. Satoh, S. Takeshita, A. Koda, R. Kadono, K. Ishida, S. Pyon, T. Sasagawa, and H. Takagi. Fermi-liquid behavior and weakly anisotropic superconductivity in the electron-doped cuprate $Sr_{1-x}La_xCuO_2$. *Phys. Rev. B*, 77:224503, 2008.

[64] R. Khasanov, A. Shengelaya, A. Maisuradze, D. Di Castro, I. M. Savić, S. Weyeneth, M. S. Park, D. J. Jang, S.-I. Lee, and H. Keller. Nodeless superconductivity in the infinite-layer electron-doped cuprate superconductor $Sr_{0.9}La_{0.1}CuO_2$. *Phys. Rev. B*, 77:184512, 2008.

[65] J. S. White, E. M. Forgan, M. Laver, P. S. Häfliger, R. Khasanov, R. Cubitt, C. D. Dewhurst, M.-S. Park, D.-J. Jang, H.-G. Lee, and S.-I. Lee. Finite gap behaviour in the superconductivity of the 'infinite layer' n-doped high-T_c superconductor $Sr_{0.9}La_{0.1}CuO_2$. *J. Phys.: Condens. Matter*, 20:104237, 2008.

[66] M. L. Teague, A. D. Beyer, M. S. Grinolds, S. I. Lee, and N.-C. Yeh. Observation of vortices and hidden pseudogap from scanning tunneling spectroscopic studies of the electron-doped cuprate superconductor $Sr_{0.9}La_{0.1}CuO_2$. *Europhys. Lett.*, 85:17004, 2009.

[67] L. Fruchter, V. Jovanovic, H. Raffy, S. Labdi, F. Bouquet, and Z. Z. Li. Penetration depth of electron-doped infinite-layer $Sr_{0.88}La_{0.12}CuO_{2+x}$ thin films. *Phys. Rev. B*, 82:144529, 2010. 3, 17, 23

[68] M.-S. Kim, M.-K. Bae, W. C. Lee, and S.-I. Lee. Thermodynamic parameters of $HgBa_2Ca_2Cu_3O_{8-x}$ from high-field magnetization. *Phys. Rev. B*, 51:3261–3264, 1995. 5

[69] Y. C. Kim, J. R. Thompson, J. G. Ossandon, D. K. Christen, and M. Paranthaman. Equilibrium superconducting properties of grain-aligned $HgBa_2Ca_2Cu_3O_{8+\delta}$. *Phys. Rev. B*, 51:11767–11772, 1995.

[70] R. Puźniak, R. Usami, K. Isawa, and H. Yamauchi. Superconducting-state thermodynamic parameters and anisotropy of $HgBa_2Ca_{n-1}Cu_nO_y$ by reversible magnetization measurements. *Phys. Rev. B*, 52:3756–3764, 1995. 5

[71] C. C. Torardi, M. A. Subramanian, J. C. Calabrese, J. Gopalakrishnan, K. J. Morrissey, T. R. Askew, R. B. Flippen, U. Chowdhry, and A. W. Sleight. Crystal Structure of $Tl_2Ba_2Ca_2Cu_3O_10$, a 125 K Superconductor. *Science*, 240:631–634, 1988. 5

[72] H. Shaked, Y. Shimakawa, B. A. Hunter, R. L. Hitterman, J. D. Jorgensen, P. D. Han, and D. A. Payne. Superconductivity in the Sr-Ca-Cu-O system and the phase with infinite-layer structure. *Phys. Rev. B*, 51(17):11784–11790, 1995. 5

[73] M. G. Smith, A. Manthiram, J. Zhou, J. B. Goodenough, and J. T. Markert. Electron-doped superconductivity at 40 K in the infinite-layer compound $Sr_{1-y}Nd_yCuO_2$. *Nature*, 351:549–551, 1991. 5

[74] G. Er, Y. Miyamoto, F. Kanamaru, and S. Kikkawa. Superconductivity in the infinite-layer compound $Sr_{1-x}La_xCuO_2$ prepared under high pressure. *Physica C*, 181:206–208, 1991. 5, 6

[75] J. D. Jorgensen, P. G. Radaelli, D. G. Hinks, J. L. Wagner, S. Kikkawa, G. Er, and F. Kanamaru. Structure of superconducting $Sr_{0.9}La_{0.1}CuO_2$ (T_c=42 K) from neutron powder diffraction. *Phys. Rev. B*, 47:14654–14656, 1993. 5, 6

[76] N. Ikeda, Z. Hiroi, M. Azuma, M. Takano, Y. Bando, and Y. Takeda. Synthesis and superconducting properties of the infinite-layer compounds $Sr_{1-x}Ln_xCuO_2$ (Ln=La, Nd, Sm, Gd) . *Physica C*, 210:367–372, 1993. 5, 6

[77] K.-I. Kubo, M. Ichikawa, N. Sugii, K. Yamamoto, and H. Yamauchi. Synthesis of the infinite-layer compounds $Ca_{1-x}Li_xCuO_2$ ($0.15 \leq x \leq 0.45$) doped with p-type carriers. *Phys. Rev. B*, 49:6919–6926, 1994. 5

[78] N. Yoshiyama, N. Sumitani, S. G. Lee, T. Takei, and H. Yamamoto. Effects of radical oxygen O* in synthesis of $Sr_{1-x}Na_xCuO_2$ infinite-layer thin film by reactive RF sputtering. *Thin Solid Films*, 334:120–124, 1998.

[79] S. Oh and J. N. Eckstein. Infinite-layer ($Ca_{1-x}Sr_xCuO_2$) film growth by molecular beam epitaxy and effect of hole doping. *Thin Solid Films*, 483:301–305, 2005. 5

[80] M. Azuma, Z. Hiroi, M. Takano, Y. Bando, and Y. Takeda. Superconductivity at 110 K in the infinite-layer compound $(Sr_{1-x}Ca_x)_{1-y}CuO_2$. *Nature*, 356:775–776, 1992. 5

[81] H. Zhang, Y. Y. Wang, H. Zhang, V. P. Dravid, L. D. Marks, P. D. Han, D. A. Payne, P. G. Radaelli, and J. D. Jorgensen. Identity of planar defects in the 'infinite-layer' copper oxide superconductor. *Nature*, 370:352–354, 1994. 5

[82] Y. Tokura, H. Takagi, and S. Uchida. A superconducting copper oxide compound with electrons as the charge carriers. *Nature*, 337:345–347, 1989. 6

[83] H. Takagi, S. Uchida, and Y. Tokura. Superconductivity produced by electron doping in CuO_2-layered compounds. *Phys. Rev. Lett.*, 62:1197–1200, 1989. 6

[84] T. Yamada, K. Kinoshita, and H. Shibata. Synthesis of Superconducting T'-$(La_{1-x}Ce_x)_2CuO_4$. *Jpn. J. Appl. Phys.*, 33:L168–L169, 1994. 6

[85] M. Naito and M. Hepp. Superconducting T'-$La_{2-x}Ce_xCuO_4$ Films Grown by Molecular Beam Epitaxy. *Jpn. J. Appl. Phys.*, 39:L485–L487, 2000. 6

[86] X. Li, M. Kanai, T. Kawai, and S. Kawai. Epitaxial Growth and Properties of $Ca_{1-x}Sr_xCuO_2$ Thin Films (x=0.18 to 1.0) Prepared by Co-Deposition and Atomic Layer Stacking. *Jpn. J. Appl. Phys.*, 31:L217–L220, 1992. 6

[87] Y. Terashima, R. Sato, S. Takeno, S.-I. Nakamura, and T. Miura. Preparation of Epitaxial $SrCuO_X$ Thin Films with an Infinite-Layer Structure. *Jpn. J. Appl. Phys.*, 32:L48–L50, 1993. 6

[88] C. Niu and C. M. Lieber. Growth of the infinite layer phase of $Sr_{1-x}Nd_xCuO_2$ by laser ablation. *Appl. Phys. Lett.*, 61:1712–1714, 1992. 6

[89] N. Sugii, M. Ichikawa, K. Kubo, T. Sakurai, K. Yamamoto, and H. Yamauchi. Growth of $Sr_{1-x}Nd_xCuO_y$ thin films by RF-magnetron sputtering and their crystallographic properties. *Physica C*, 196:129–134, 1992. 6

[90] Handbook of Chemistry and Physics, The Chemical Rubber Company, U. S. A., 52nd ed. (1971). 6

[91] N. Sugii, K. Matsuura, K. Kubo, K. Yamamoto, and M. Ichikawa. Superconducting $Sr_{0.875}Nd_{0.125}CuO_{2-\delta}$ thin films. *J. Appl. Phys.*, 74:4047–4051, 1993. 6

[92] J. T. Markert, T. C. Messina, B. Dam, J. Huijbregste, J. H. Rector, and R. Griessen. Laser-ablated thin films of infinite-layer compounds and related materials. *Proc. SPIE*, 4058:141, 2000.

[93] J. T. Markert, T. C. Messina, B. Dam, J. Huijbregste, J. H. Rector, and R. Griessen. Infinite-layer copper-oxide laser-ablated thin films: substrate, buffer-layer, and processing effects. *IEEE Trans. Appl. Supercond.*, 13:2684–2686, 2003.

[94] V. Leca, D. H. A. Blank, G. Rijnders, S. Bals, and G. van Tendeloo. Superconducting single-phase $Sr_{1-x}La_xCuO_2$ thin films with improved crystallinity grown by pulsed laser deposition. *Appl. Phys. Lett.*, 89:092504, 2006. 6, 7

[95] V. Leca, G. Visanescu, C. Back, R. Kleiner, and D. Koelle. Growth mechanism, microstructure and transport properties of $Sr_{1-x}La_xCuO_2$ (x = 0.10-0.15) thin films. *Appl. Phys. A*, 93:779–782, 2008. 6

[96] S. Karimoto, K. Ueda, M. Naito, and T. Imai. Single-crystalline superconducting thin films of electron-doped infinite-layer compounds grown by molecular-beam epitaxy. *Appl. Phys. Lett.*, 79(17):2767–2769, 2001. 6, 7

[97] S.-I. Karimoto and M. Naito. Electron-doped infinite-layer thin films with T_C over 40 K grown on $DyScO_3$ substrates. *Appl. Phys. Lett.*, 84:2136, 2004. 6, 7

[98] J. D. Jorgensen, P. G. Radaelli, H. Shaked, J. L. Wagner, B. A. Hunter, J. F. Mitchell, R. L. Hitterman, and D. G. Hinks. Roles of Oxygen Defects in Copper Oxide Superconductors. *Journal of Superconductivity*, 7:145–149, 1994. 6

[99] M. Naito, H. Sato, and H. Yamamoto. MBE growth of $(La,Sr)_2CuO_4$ and $(Nd,Ce)_2CuO_4$ thin films. *Physica C*, 293:36–43, 1997. 6

[100] H. Adachi, T. Satoh, Y. Ichikawa, K. Setsune, and K. Wasa. Superconducting $(Sr,Nd)CuO_y$ thin films with infinite-layer structure. *Physica C*, 196:14–16, 1992. 6, 7

[101] Z. Z. Li, V. Jovanovic, H. Raffy, and S. Megtert. Influence of oxygen reduction on the structural and electronic properties of electron-doped $Sr_{1-x}La_xCuO_2$ thin films. *Physica C*, 469:73–81, 2009. 6, 7

[102] X. Zhou, Y. Yao, J. Li, W. Xu, S. Jia, and Z. Zhao. Phase Transformation in the Infinite Layer Structure Compound (Sr, Nd) CuO_2 and its Effect on Superconductivity. *Chinese. Phys. Lett.*, 10:503–506, 1993. 7

[103] B. Mercey, A. Gupta, M. Hervieu, and B. Raveau. A New Ordered Oxygen-Deficient Perovskite $Sm_2Sr_6Cu_8O_{17+\delta}$: HREM Study of PLD Thin Films. *Journal of Solid State Chemistry*, 116:300–306, 1995. 7

[104] I. N. Stranski and L. Krastanov. *Akad. Wiss. Lit. Mainz Math.-Natur. Kl. IIb*, 146:797, 1939. 7

[105] T. Nishizaki, Y. Yamasaki, R. Tanaka, F. Ichikawa, T. Fukami, T. Aomine, S. Kubo, and M. Suzuki. Angular dependence of transport critical currents in magnetic fields and flux pinning properties in $Nd_{2-x}Ce_xCuO_4$ thin films. *Physica B*, 194-196:1877–1878, 1994. 7

[106] B. D. Josephson. Possible New Effects in Superconductive Tunneling. *Phys. Lett.*, 1:251–253, 1962. 9, 13

[107] K. K. Likharev. *Dynamics of Josephson junctions and circuits.* Gordon and Breach Science Publishers, New York, USA, 1986. 9, 13

[108] I. Giaever and K. Megerle. Study of Superconductors by Electron Tunneling. *Phys. Rev.*, 122:1101–1111, 1961. 9

[109] I. Giaever, H. R. Hart Jr., and K. Megerle. Tunneling into Superconductors at Temperatures below 1 °K. *Phys. Rev.*, 126:941–948, 1962. 9

[110] R. Monaco and A. Oliva. Selective trilayer deposition process for fabricating Nb/Al-AlO_x/Nb Josephson tunnel junctions. *Appl. Phys. Lett.*, 64:3042–3044, 1994. 9

[111] C. A. Hamilton. Josephson voltage standards. *Rev. Sci. Instr.*, 71:3611–3623, 2000. 9

[112] A. Mathai, D. Song, Y. Gim, and F. C. Wellstood. High resolution magnetic microscopy using a DC SQUID . *IEEE Trans. Appl. Supercond.*, 3:2609–2612, 1993. 9

[113] J. R. Kirtley. SQUID microscopy for fundamental studies. *Physica C*, 368:55–65, 2002. 9

[114] V. Pizzella, S. Della Penna, C. Del Gratta, and G. L. Romani. SQUID systems for biomagnetic imaging. *Supercond. Sci. Technol.*, 14:R79–R114, 2001. 10

[115] J. Vrba and S. E. Robinson. SQUID sensor array configurations for magnetoencephalography applications. *Supercond. Sci. Technol.*, 15:R51–R89, 2002. 10

[116] A. V. Ustinov. Solitons in Josephson junctions. *Physica D*, 123:315–329, 1998. 10

[117] Y. Tanaka. Josephson effect between s wave and $d_{x^2-y^2}$ wave superconductors. *Phys. Rev. Lett.*, 72:3871–3874, 1994. 10

[118] Pair Tunneling from c-Axis $YBa_2Cu_3O_{7-x}$ to Pb: Evidence for s-Wave Component from Microwave Induced Steps. *Phys. Rev. Lett.*, 76:2161–2164, 1996. 10

[119] J. Lesueur, M. Aprili, A. Goulon, T. J. Horton, and L. Dumoulin. Evidence for a Josephson tunnel current in all *in situ* c-$YBa_2Cu_3O_7$/Pb junctions. *Phys. Rev. B*, 55:R3398–R3401, 1997. 10

[120] S. I. Woods, A. S. Katz, T. L. Kirk, M. C. de Andrade, M. B. Maple, and R. C. Dynes. Investigation of Nd-Ce-Cu-O Planar Tunnel Junctions and Bicrystal Grain Boundary Junctions. *IEEE Trans. Appl. Supercond.*, 1998. 10

[121] M. Mößle and R. Kleiner. c-axis Josephson tunneling between $Bi_2Sr_2CaCu_2O_{8+x}$ and Pb. *Phys. Rev. B*, 59:4486–4496, 1999. 10

[122] J. Ghijsen, L. H. Tjeng, J. van Elp, H. Eskes, J. Westerink, G. A. Sawatzky, and M. T. Czyzyk. Electronic structure of Cu_2O and CuO. *Phys. Rev. B*, 38(16):11322–11330, 1988. 11

[123] S. Poulston, P. M. Parlett, P. Stone, and M. Bowker. Surface Oxidation and Reduction of CuO and Cu_2O Studied Using XPS and XAES. *Surface and Interface Analysis*, 24:811–820, 1996.

[124] P. D. Kirsch and J. G. Ekerdt. Chemical and thermal reduction of thin films of copper (II) oxide and copper (I) oxide. *J. Appl. Phys.*, 90:4256–4264, 2001. 11

[125] R. P. Vasquez, C. U. Jung, J. Y. Kim, M.-S. Park, H.-J. Kim, and S.-I. Lee. X-ray photoemission study of the infinite-layer cuprate superconductor $Sr_{0.9}La_{0.1}CuO_2$. *J. Phys.: Condens. Matter*, 13:7977–7985, 2001. 12

[126] G. Burns. *High-temperature superconductivity: an introduction.* Academic Press, Inc., San Diego, USA. 13

[127] D. Dimos, P. Chaudhari, J. Mannhart, and F. K. LeGoues. Orientation Dependence of Grain-Boundary Critical Currents in $YBa_2Cu_3O_{7-\delta}$ Bicrystals. *Phys. Rev. Lett.*, 61:219–221, 1988. 13

[128] K. Char, M. S. Colclough, S. M. Garrison, N. Newman, and G. Zaharchuk. Bi-epitaxial grain boundary junctions in $YBa_2Cu_3O_7$. *Appl. Phys. Lett.*, 59:733–735, 1991. 13

[129] A. di Chiara, F. Lombardi, F. M. Granozio, U. S. di Uccio, F. Tafuri, and M. Valentino. $YBa_2Cu_3O_{7-x}$ grain boundary Josephson junctions with a MgO seed layer. *IEEE Trans. Appl. Supercond.*, 7:3327–3330, 1997. 13

[130] K. P. Daly, W. D. Dozier, J. F. Burch, S. B. Coons, R. Hu, C. E. Platt, and R. W. Simon. Substrate step-edge $YBa_2Cu_3O_7$ rf SQUIDs. *Appl. Phys. Lett.*, 58:543–545, 1991. 13

[131] G. Friedl, B. Roas, M. Römheld, L. Schultz, and W. Jutzi. Transport properties of epitaxial $YBa_2Cu_3O_x$ films at step edges. *Appl. Phys. Lett.*, 59:2751–2753, 1991.

[132] K. Herrmann, Y. Zhang, H.-M. Muck, J. Schubert, W. Zander, and A. I. Braginski. Characterization of $YBa_2Cu_3O_7$ step-edge Josephson junctions. *Supercond. Sci. Technol.*, 4:583–586, 1991. 13

[133] H. Hilgenkamp and J. Mannhart. Grain boundaries in high-T_c superconductors. *Rev. Mod. Phys.*, 74:485–549, 2002. 13, 14, 15

[134] R. Gross. *Interfaces in High-T_c Superconducting Systems, Springer Verlag,*, pages 176–209, 1994.

[135] J. Mannhart and P. Chaudhari. High-T_c Bicrystal Grain Boundaries. *Phys. Today*, 54:48–53, 2001. 13

[136] P. Chaudhari, J. Mannhart, D. Dimos, C. C. Tsuei, J. Chi, M. M. Oprysko, and M. Scheuermann. Direct Measurement of the Superconducting Properties of Single Grain Boundaries in $Y_1Ba_2Cu_3O_{7-\delta}$. *Phys. Rev. Lett.*, 60:1653–1656, 1988. 13

[137] D. Koelle, R. Kleiner, F. Ludwig, E. Dantsker, and J. Clarke. High-transition-temperature superconducting quantum interference devices. *Rev. Mod. Phys.*, 71:631–686, 1999. 13

[138] A. G. Likhachev, V. N. Polushkin, S. V. Uchaikin, and B. V. Vasiliev. Magnetocardiometer based on a single-hole high-T_c SQUID. *Supercond. Sci. Technol.*, 3:148–150, 1990. 13

[139] D. Drung, F. Ludwig, W. Müller, U. Steinhoff, L. Trahms, H. Koch, Y. Q. Shen, M. B. Jensen, P. Vase, T. Holst, T. Freltoft, and G. Curio. Integrated $YBa_2Cu_3O_{7-x}$ magnetometer for biomagnetic measurements. *Appl. Phys. Lett.*, 68:1421–1423, 1996. 13

[140] R. C. Black, A. Mathai, F. C. Wellstood, E. Dantsker, A. H. Miklich, D. T. Nemeth, J. J. Kingston, and J. Clarke. Magnetic microscopy using a liquid nitrogen cooled $YBa_2Cu_30_7$ superconducting quantum interference device. *Appl. Phys. Lett.*, 62:2128–2130, 1993. 13

[141] C.-R. Hu. Midgap surface states as a novel signature for $d^2_{xa} - x^2_b$-wave superconductivity. *Phys. Rev. Lett.*, 72:1526–1529, 1994. 13

[142] A. F. Andreev. *Zh. Eksp. Teor. Fiz.*, 46:1823, 1964. 13

[143] D. Saint-James. Excitations élémentaires au voisinage de la surface de séparation d'un métal normal et d'un métal supraconducteur. *J. Phys. France*, 25:899–905, 1964. 13

[144] S. Kashiwaya and Y. Tanaka. Tunnelling effects on surface bound states in unconventional superconductors. *Rep. Prog. Phys.*, 63:1641–1724, 2000. 13

[145] G. Deutscher. Andreev–Saint-James reflections: A probe of cuprate superconductors. *Rev. Mod. Phys.*, 77:109–135, 2005. 13

[146] J. W. Ekin, Y. Xu, S. Mao, T. Venkatesan, D. W. Face, M. Eddy, and S. A. Wolf. Correlation between *d*-wave pairing behavior and magnetic-field-dependent zero-bias conductance peak. *Phys. Rev. B*, 56:13746–13749, 1997. 13

[147] M. Covington, M. Aprili, E. Paraoanu, L. H. Greene, F. Xu, J. Zhu, and C. A. Mirkin. Observation of Surface-Induced Broken Time-Reversal Symmetry in $YBa_2Cu_3O_7$ Tunnel Junctions. *Phys. Rev. Lett.*, 79:277–280, 1997.

[148] L. Alff, H. Takashima, S. Kashiwaya, N. Terada, H. Ihara, Y. Tanaka, M. Koyanagi, and K. Kajimura. Spatially continuous zero-bias conductance peak on (110) $YBa_2Cu_3O_{7-\delta}$ surfaces. *Phys. Rev. B*, 55:R14757–R14760, 1997.

[149] L. Alff, A. Beck, R. Gross, A. Marx, S. Kleefisch, Th. Bauch, H. Sato, M. Naito, and G. Koren. Observation of bound surface states in grain-boundary junctions of high-temperature superconductors. *Phys. Rev. B*, 58:11197–11200, 1998. 14

[150] L. Alff, S. Kleefisch, U. Schoop, M. Zittartz, T. Kemen, T. Bauch, A. Marx, and R. Gross. Andreev bound states in high temperature superconductors. *Eur. Phys. J. B*, 5:423–438, 1998.

[151] J. Y. T. Wei, N.-C. Yeh, D. F. Garrigus, and M. Strasik. Directional Tunneling and Andreev Reflection on $YBa_2Cu_3O_{7-\delta}$ Single Crystals: Predominance of *d*-Wave Pairing Symmetry Verified with the Generalized Blonder, Tinkham, and Klapwijk Theory. *Phys. Rev. Lett.*, 81:2542–2545, 1998. 13

[152] F. Hayashi, E. Ueda, M. Sato, K. Kurahashi, and K. Yamada. Anisotropy of the Superconducting Order Parameter of $Nd_{2-x}Ce_xCuO_4$ Studied by STM/STS. *J. Phys. Soc. Jpn.*, 67:3234–3239, 1998. 13

[153] A. Mourachkine. Andreev reflections and tunneling spectroscopy on underdoped $Nd_{1.85}Ce_{0.15}CuO_{4-\delta}$. *Europhys. Lett.*, 50:663–667, 2000.

[154] A. Biswas, P. Fournier, M. M. Qazilbash, V. N. Smolyaninova, H. Balci, and R. L. Greene. Evidence of a *d*- to *s*-Wave Pairing Symmetry Transition in the Electron-Doped Cuprate Superconductor $Pr_{2-x}Ce_xCuO_4$. *Phys. Rev. Lett.*, 88:207004, 2002.

[155] B. Chesca, M. Seifried, T. Dahm, N. Schopohl, D. Koelle, R. Kleiner, and A. Tsukada. Observation of Andreev bound states in bicrystal grain-boundary Josephson junctions of the electron-doped superconductor $La_{2-x}Ce_xCuO_{4-y}$. *Phys. Rev. B*, 71:104504, 2005.

[156] M. Wagenknecht, D. Koelle, R. Kleiner, S. Graser, N. Schopohl, B. Chesca, A. Tsukada, S. T. B. Goennenwein, and R. Gross. Phase Diagram of the Electron-Doped $La_{2-x}Ce_xCuO_4$ Cuprate Superconductor from Andreev Bound States at Grain Boundary Junctions. *Phys. Rev. Lett.*, 100:227001, 2008. 13, 14, 15

[157] J. Appelbaum. "*s-d*" Exchange Model of Zero-Bias Tunneling Anomalies. *Phys. Rev. Lett.*, 17:91–95, 1966. 13

[158] P. W. Anderson. Localized Magnetic and Fermi-Surface Anomalies in Tunneling. *Phys. Rev. Lett.*, 17:95–97, 1966. 13

[159] C.-R. Hu. Origin of the zero-bias conductance peaks observed ubiquitously in high-T_c superconductors. *Phys. Rev. B*, 57:1266–1276, 1998. 14

[160] S. Kashiwaya, T. Ito, K. Oka, S. Ueno, H. Takashima, M. Koyanagi, Y. Tanaka, and K. Kajimura. Tunneling spectroscopy of superconducting $Nd_{1.85}Ce_{0.15}CuO_{4-\delta}$. *Phys. Rev. B*, 57:8680–8686, 1998. 14

[161] C. C. Tsuei and J. R. Kirtley. Phase-Sensitive Evidence for *d*-Wave Pairing Symmetry in Electron-Doped Cuprate Superconductors. *Phys. Rev. Lett.*, 85:182–185, 2000. 14, 17

[162] Ariando, D. Darminto, H.-J. H. Smilde, V. Leca, D. H. A. Blank, H. Rogalla, and H. Hilgenkamp. Phase-Sensitive Order Parameter Symmetry Test Experiments Utilizing $Nd_{2-x}Ce_xCuO_{4-y}$/Nb Zigzag Junctions. *Phys. Rev. Lett.*, 94:167001, 2005. 14

[163] M. Aprili, M. Covington, E. Paraoanu, B. Niedermeier, and L. H. Greene. Tunneling spectroscopy of the quasiparticle Andreev bound state in ion-irradiated $YBa_2Cu_3O_{7-\delta}$/Pb junctions. *Phys. Rev. B*, 57:R8139–R8142, 1998. 14

[164] G. E. Blonder, M. Tinkham, and T. M. Klapwijk. Transition from metallic to tunneling regimes in superconducting microconstrictions: Excess current, charge imbalance, and supercurrent conversion. *Phys. Rev. B*, 25:4515–4532, 1982. 14

[165] F. Giubileo, S. Piano, A. Scarfato, F. Bobba, A. Di Bartolomeo, and A. M. Cucolo. Study of the pairing symmetry in the electron-doped cuprate $Pr_{1-x}LaCe_xCuO_{4-y}$ by tunneling spectroscopy. *Physica C*, 470:922–925, 2010. 14

[166] H. Won and K. Maki. *d*-wave superconductor as a model of high-T_c superconductors. *Phys. Rev. B*, 49:1397–1402, 1994. 14

[167] C. Noce and M. Cuoco. Temperature dependence of the superconducting energy gap from conductance curves. *Il Nuovo Cimento D*, 18:1449–1454, 1996. 14

[168] R. C. Dynes, V. Narayanamurti, and J. P. Garno. Direct Measurement of Quasiparticle-Lifetime Broadening in a Strong-Coupled Superconductor. *Phys. Rev. Lett.*, 41:1509–1512, 1978. 14

[169] W. C. Stewart. Current-Voltage Characteristics of Josephson Junctions. *Appl. Phys. Lett.*, 12:277–280, 1968. 14

[170] D. E. McCumber. Effect of ac Impedance on dc Voltage-Current Characteristics of Superconductor Weak-Link Junctions. *J. Appl. Phys.*, 39:3113–3118, 1968. 14

[171] S. Kleefisch, L. Alff, U. Schoop, A. Marx, R. Gross, M. Naito, and H. Sato. Superconducting $Nd_{1.85}Cu_{0.15}CuO_{4-y}$ bicrystal grain boundary Josephson junctions. *Appl. Phys. Lett.*, 72:2888–2890, 1998. 14, 15

[172] M. Wagenknecht. *Korngrenzen-Tunnelspectroskopie am elektronendotierten Kupratsupraleiter $La_{2-x}Ce_xCuO_4$*. PhD thesis, University of Tuebingen, Germany, 2008. 14

[173] H. Hilgenkamp and J. Mannhart. Superconducting and normal-state properties of $YBa_2Cu_3O_{7-\delta}$-bicrystal grain boundary junctions in thin films. *Appl. Phys. Lett.*, 73:265–267, 1998. 14

[174] R. Gross and B. Mayer. Transport process and noise in $YBa_2Cu_3O_{7-\delta}$ grain boundary junctions. *Physica C*, 180:235–242, 1991. 14

[175] G. Deutscher and K. A. Müller. Origin of Superconductive Glassy State and Extrinsic Critical Currents in High-T_c Oxides. *Phys. Rev. Lett.*, 59:1745–1747, 1987. 14

[176] R. Gross, P. Chaudhari, D. Dimos, A. Gupta, and G. Koren. Thermally Activated Phase Slippage in High-T_c Grain-Boundary Josephson Junctions. *Phys. Rev. Lett.*, 64:228–231, 1990. 15

[177] V. Ambegaokar and B. I. Halperin. Voltage due to thermal noise in the dc Josephson effect. *Phys. Rev. Lett.*, 22:1364–1366, 1969. 15

[178] P. A. Rosenthal, M. R. Beasley, K. Char, M. S. Colclough, and G. Zaharchuk. *Appl. Phys. Lett.*, 59:3482–3484, 1991. 15, 21

[179] D. D. Coon and M. D. Fiske. Josephson ac and Step Structure in the Supercurrent Tunneling Characteristic. *Phys. Rev.*, 138:A744–A746, 1965. 15

[180] R. E. Eck, D. J. Scalapino, and B. N. Taylor. Self-detection of the ac Josephson current. *Phys. Rev. Lett.*, 13:15–18, 1964. 15

[181] J. C. Swihart. Field Solution for a Thin-Film Superconducting Strip Transmission Line. *J. Appl. Phys.*, 32:461–469, 1961. 15

[182] D. Winkler, Y. M. Zhang, P. A. Nilsson, E. A. Stepantsov, and T. Claeson. Electromagnetic Properties at the Grain Boundary Interface of a $YBa_2Cu_3O_{7-\delta}$ Bicrystal Josephson Junction. *Phys. Rev. Lett.*, 72:1260–1263, 1994. 15

[183] Y. M. Zhang, D. Winkler, P.-A. Nilsson, and T. Claeson. Josephson flux-flow resonances in overdamped long $YBa_2Cu_3O_7$ grain-boundary junctions. *Phys. Rev. B*, 51:8684–8687, 1995. 15

[184] S. Kleefisch, B. Welter, A. Marx, L. Alff, R. Gross, and M. Naito. Possible pseudogap behavior of electron-doped high-temperature superconductors. *Phys. Rev. B*, 63:100507, 2001. 15

[185] V. B. Geshkenbein, A. I. Larkin, and A. Barone. Vortices with half magnetic flux quanta in "heavy-fermion" superconductors. *Phys. Rev. B*, 36:235–238, 1987. 17

[186] M. Sigrist and T. M. Rice. Paramagnetic Effect in High T_c Superconductors - A Hint for *d*-Wave Superconductivity. *J. Phys. Soc. Jpn.*, 61:4283–4286, 1992. 17

[187] C. C. Tsuei, J. R. Kirtley, M. Rupp, J. Z. Sun, A. Gupta, M. B. Ketchen, C. A. Wang, Z. F. Ren, J. H. Wang, and M. Bhushan. Pairing Symmetry in Single-Layer Tetragonal $TI_2Ba_2CuO_{6+\delta}$ Superconductors. *Science*, 271:329–332, 1996. 17

[188] J. R. Kirtley, C. C. Tsuei, H. Raffy, Z. Z. Li, A. Gupta, J. Z. Sun, and S. Megtert. Half-integer flux quantum effect in tricrystal $Bi_2Sr_2CaCu_2O_{8+\delta}$. *Europhys. Lett.*, 36:707, 1996.

[189] C. C. Tsuei, J. R. Kirtley, Z. F. Ren, J. H. Wang, H. Raffy, and Z. Z. Li. Pure $d_{x^2-y^2}$ order-parameter symmetry in the tetragonal superconductor $Tl_2Ba_2CuO_{6+\delta}$. *Nature*, 387:481–483, 1997.

[190] C. C. Tsuei and J. R. Kirtley. Tricrystal tunneling evidence for d-wave pairing symmetry in cuprate superconductors. *Journal of Alloys and Compounds*, 250:615–618, 1997. 17

[191] B. Chesca. Magnetic field dependencies of the critical current and of the resonant modes of dc SQUIDs fabricated from superconductors with $s+id_{x^2-y^2}$ order-parameter symmetries. *Ann. Phys.*, 8:511–522, 1999. 17

[192] R. R. Schulz, B. Chesca, B. Goetz, C. W. Schneider, A. Schmehl, H. Bielefeldt, H. Hilgenkamp, and J. Mannhart. Design and realization of an all d-wave dc π-superconducting quantum interference device. *Appl. Phys. Lett.*, 76:912–914, 2000. 17, 21

[193] B. Chesca, R. R. Schulz, B. Goetz, C. W. Schneider, H. Hilgenkamp, and J. Mannhart. d-Wave Induced Zero-Field Resonances in dc π-Superconducting Quantum Interference Devices. *Phys. Rev. Lett.*, 88:177003, 2002. 17, 23

[194] B. Chesca, K. Ehrhardt, M. Mößle, R. Straub, D. Koelle, R. Kleiner, and A. Tsukada. Magnetic-Field Dependence of the Maximum Supercurrent of $La_{2-x}Ce_xCuO_{4-y}$ Interferometers: Evidence for a Predominant $d_{x^2-y^2}$ Superconducting Order Parameter. *Phys. Rev. Lett.*, 90:057004, 2003. 17, 21

[195] J. Clarke, A. I. Braginski, B. Chesca, R. Kleiner, and D. Koelle. *The SQUID Handbook*, volume 1, chapter 2. WILEY-VCH Verlag GmbH & Co. KGaA, Weinheim, Germany, 2004. 20, 22, 23

[196] B. Chesca and R. Kleiner. Electronic behavior of spatially distributed junction small inductance dc π-SQUIDs. *Physica C*, 350:180–186, 2001. 21, 23

[197] B. Chesca and R. Kleiner. Order parameter phase sensitive experiments and SDJ dc SQUIDs. *Physica C*, 357:1561–1566, 2001. 23

[198] P. Müller and A. V. Ustinov. *The Physics of Superconductors*. Springer-Verlag, Berlin Heidelberg, Germany, 1997. 23

[199] K. Terai, M. Lippmaa, P. Ahmet, T. Chikyow, T. Fujii, H. Koinuma, and M. Kawasaki. In-plane lattice constant tuning of an oxide substrate with $Ba_{1-x}Sr_xTiO_3$ and $BaTiO_3$ buffer layers. *Appl. Phys. Lett.*, 80:4437–4439, 2002. 25

Appended publications

Publication I

Properties of the electron-doped infinite-layer superconductor $Sr_{1-x}La_xCuO_2$ epitaxially grown by pulsed laser deposition

J. Tomaschko,[1] V. Leca,[1,2,3,*] T. Selistrovski,[1] S. Diebold,[1] J. Jochum,[1] R. Kleiner,[1] and D. Koelle[1]

[1]*Physikalisches Institut and Center for Collective Quantum Phenomena in LISA$^+$, Universität Tübingen, Auf der Morgenstelle 14, DE-72076 Tübingen, Germany*

[2]*National Institute for Research and Development in Microtechnologies, Erou Iancu Nicolae Str. 126 A, RO-077190, Bucharest, Romania*

[3]*Faculty of Applied Chemistry and Materials Science, University Politehnica of Bucharest, Gheorghe Polizu Str. 1-7, RO-011061, Bucharest, Romania*

(Received 20 December 2011; published 11 January 2012)

Thin films of the electron-doped infinite-layer cuprate superconductor $Sr_{1-x}La_xCuO_2$ (SLCO) with doping $x \approx 0.15$ were grown by means of pulsed laser deposition. (001)-oriented $KTaO_3$ and $SrTiO_3$ single crystals were used as substrates. In case of $SrTiO_3$, a $BaTiO_3$ thin film was deposited prior to SLCO, acting as buffer layer providing tensile strain to the SLCO film. To induce superconductivity, the as-grown films were annealed under reducing conditions, which will be described in detail. The films were characterized by reflection high-energy electron diffraction, atomic force microscopy, x-ray diffraction, Rutherford backscattering spectroscopy, and electric transport measurements at temperatures down to $T = 4.2$ K. We discuss in detail the influence of different process parameters on the final film properties.

DOI: 10.1103/PhysRevB.85.024519 PACS number(s): 74.72.Ek, 74.25.F−, 81.15.Fg, 68.55.−a

I. INTRODUCTION

Cuprates exhibiting electron doping form a minor group among high-transition temperature (high-T_c) cuprate superconductors. In fact, only two families of electron-doped cuprate superconductors are known. These are the T' compounds[1,2] $Ln^{III}_{2-x}Ce_xCuO_4$ (Ln^{III} = La,Pr,Nd,Sm,Eu,Gd) with maximum $T_c \approx 30$ K[3,4] and the infinite-layer (IL) compounds[5–7] $Sr_{1-x}Ln^{III}_xCuO_2$ (Ln^{III} = La,Pr,Nd,Sm,Gd) with maximum $T_c \approx 43$ K.[6,8–10] Formally, the IL crystal is a member of the $A^{III}_2A^{II}_2Ca_{n-1}Cu_nO_{2n+4}$ high-T_c superconductors (A^{III} = Tl or Bi and A^{II} = Ca, Sr or Ba), where $n = \infty$.[5,11] The IL crystal is thus formed by alternating stacks of copper oxide planes (CuO_2) and alkaline earth metal planes (A^{II}) along the c-axis direction, forming an $A^{II}CuO_2$ crystal. To induce electron doping, the divalent alkaline earth metal A^{II} is substituted partially by a trivalent lanthanide Ln^{III} to form $A^{II}_{1-x}Ln^{III}_xCuO_2$ or, as in our case, $Sr_{1-x}La_xCuO_2$ (SLCO).[8] Common features of cuprate superconductors, such as apical oxygen or charge reservoir blocks, are not present in the ideal IL structure.[12] As the crystal structure of the IL compounds is the most simple of all cuprate superconductors, they are often denoted as "parent structure" of cuprate superconductors.[5] Due to their simplicity, they also provide a unique opportunity to explore the basic nature of high-T_c superconductivity. However, synthesizing high-quality IL samples is a challenging task, which explains that IL compounds have been examined less extensively than other superconducting cuprates. No large IL single crystals have been synthesized so far, and only high-pressure synthesis (∼1 GPa) of polycrystalline bulk material was successful.[7,9,10] To overcome this problem, single crystalline thin films were grown, where the high-pressure IL phase is stabilized by epitaxy.[13,14] However, in the first attempts, $SrTiO_3$ (STO) with an in-plane lattice constant of $a_{STO} = 3.905$ Å was most often used as substrate,[15,16] leading to compressively strained IL films (bulk $a_{IL} \approx 3.95$ Å) with inferior superconducting properties. It is known, that electron doping stretches the Cu-O bonds because antibonding $\sigma_{x^2-y^2}$ orbitals in the CuO_2 sheets are occupied.[7] Therefore the idea was to enhance the electron-doping effect by epitaxial strain. Different buffer layers, such as T' compounds ($Ln^{III}_2CuO_4$) or $BaTiO_3$ (BTO), with increased in-plane lattice constants were subsequently introduced to induce relaxed or tensile strained films.[17–21] Indeed, superconducting IL films were fabricated with this method, however, still with reduced T_c. Only one group[22] succeeded in synthesizing electron-doped IL films with T_c close to the bulk value by means of molecular beam epitaxy (MBE). The key was to choose $KTaO_3$ (KTO, with $a_{KTO} = 3.988$ Å) as substrate, supplying tensile strain and making buffer layers redundant. However, in a later work,[23] the same group showed that they could further increase T_c when they chose another substrate, (110)-oriented $DyScO_3$ (DSO), with a slightly smaller in-plane lattice constant ∼3.944 Å, which fits better the lattice constant of bulk $Sr_{0.9}La_{0.1}CuO_2$ ($a_{SLCO} \approx 3.949$ Å).[8,9] Thus growth of SLCO on DSO resulted in almost fully relaxed SLCO films with best transport properties reported, so far.

Moreover, it was found that as-grown IL films contain excess oxygen forming O^{2-} ions on interstitial sites in the $A^{II}_{1-x}Ln^{III}_x$ planes, which hampers superconductivity by localizing free charge carriers and by disturbing[24] the crystal lattice. Therefore, as for T' compounds,[25] a vacuum annealing step was introduced to remove excess oxygen and to induce superconductivity. Meanwhile, this reduction step is commonly used for synthesis of superconducting IL films grown by numerous techniques, such as sputtering,[26,27] pulsed laser deposition (PLD)[20,21] and MBE.[22,23] However, too strong reduction generates oxygen vacancies in the CuO_2 planes and destroys superconductivity.[22,27,28] A secondary phase can be formed if the oxygen vacancies arrange in an ordered structure, referred to in literature as the "long c-axis" phase or "infinite-layer-related" (IL-r) phase.[20,26,29–31] Its unit cell

$2\sqrt{2}a_{\mathrm{IL}} \times 2\sqrt{2}a_{\mathrm{IL}} \times c_s$ is a superstructure of the IL unit cell, where a_{IL} is the in-plane lattice parameter of the IL structure and c_s is the extended c-axis parameter of the superstructure (with $c_s \sim 3.6$ Å as compared to $c_{\mathrm{IL}} \sim 3.4$ Å). Hence, the main challenge in synthesizing superconducting IL compounds is to simultaneously reduce the $A^{\mathrm{II}}_{1-x}Ln^{\mathrm{III}}_{x}$ planes without reducing the CuO_2 planes.

In this work, we report on the fabrication of superconducting SLCO films (with maximum $T_c = 22$ K) with doping $x \approx 0.15$ by means of PLD. The fabrication process is described in detail. KTO and STO single crystals were used as substrates. Prior to deposition of SLCO on STO, BTO films were deposited, acting as buffer layers. The growth mode, the evolution of the in-plane lattice parameter a, and the morphology of the films was monitored *in situ* by high-pressure reflection high-energy electron diffraction (RHEED). Atomic force microscopy (AFM) revealed very flat surfaces with asperities in the range of 1–3 unit cells (uc). X-ray diffraction (XRD) was used to check the crystal quality and lattice constants of the films, revealing almost completely relaxed BTO buffer layers, moderately tensile strained SLCO films on BTO-buffered STO and highly tensile strained SLCO films on KTO. The stoichiometry of SLCO films on BTO/STO was determined by Rutherford backscattering spectroscopy (RBS), showing that the films are slightly overdoped. Current-voltage [$I(V)$] characteristics and resistivity ρ versus temperature T were examined by electric transport measurements at temperatures down to $T = 4.2$ K. Finally, we discuss the influence of different process parameters on the final film properties, such as excimer laser energy, target-to-substrate distance, deposition pressure, vacuum annealing time, and vacuum annealing temperature.

II. SAMPLE FABRICATION AND EXPERIMENTAL DETAILS

For epitaxial growth of typically 20 to 25 nm thick SLCO films, a polycrystalline target[32] with nominal doping $x = 0.125$ was used. Both, (001)-oriented KTO[33] and (001)-oriented STO[34] single crystals ($5 \times 5 \times 1$ mm^3) were used as substrates. When STO was used as substrate, a typically 25 to 30 nm thick BTO film was deposited prior to SLCO, acting as a buffer layer. For that purpose, a stoichiometric, polycrystalline target[32] was used. All films were grown in an ultrahigh vacuum system (base pressure $p_{\mathrm{vac}} \approx 10^{-6}$ Pa) by means of PLD, using a KrF excimer laser ($\lambda = 248$ nm) at a repetition rate of 2 Hz. The excimer laser energy was set to $E_L = (110–130)$ mJ and the laser spot size on the target was $A_L \approx 2$ mm^2. The growth mode and the number of deposited monolayers were monitored *in situ* by high-pressure RHEED. The sample temperature was checked with a band radiation pyrometer (1.45 to 1.80 μm) while the sample was heated with an infrared diode laser ($\lambda =$ 808 nm) irradiating the backside of the sample holder. Right after SLCO film deposition, 10 to 20 nm thick gold pads were evaporated or magnetron sputtered *ex situ* through shadow masks, to ensure low-resistive ohmic contacts. For electric transport measurements, we performed $\rho(T)$ measurements on unpatterned films in a four-point van der Pauw geometry with typical bias currents $I = (10–100)$ μA. All measured values for T_c given in the text refer to the midpoint of the resistive transition. For measurements of $I(V)$ characteristics, the films were patterned into 40 μm wide bridges (with 20 or 40 μm voltage pad separation) by photolithography and argon ion milling. $I(V)$ and $\rho(T)$ curves were recorded in a magnetically and radio frequency shielded setup using feed lines with high-frequency noise filters. The crystal structure of the films was characterized *ex situ* by XRD equipped with a Cu cathode and monochromator. The morphology was checked by AFM in contact mode. RBS was performed at a 3-MeV Van-de-Graaff accelerator to determine the stoichiometry of the films.[35,36] The accelerator can be used at energies between 0.7 and 3.7 MeV with a beam stability of ~2 keV. The pressure is $0.5–1 \times 10^{-4}$ Pa and the acceleration distance is 30 m. RBS was performed with α particles at a fixed angle of 165°. The energy resolution of the detector is 20 keV.

A. Deposition of BTO buffer layers on STO

For as-received STO substrates, we established an *in situ* annealing process prior to BTO deposition to ensure the formation of a smooth STO surface suitable for epitaxial growth of BTO. For that purpose, the STO substrates were heated in oxygen at a pressure of $p_{O_2} = 10$ Pa to $T = 1000\,^{\circ}$C with a rate of $\delta T/\delta t = 40\,^{\circ}$C/min and kept there for $t =$ 5 min. During this period, the RHEED pattern became more pronounced, exhibiting several Kikuchi lines and thin streaks and spots [cf. Fig. 1(a)], typical for smoothing of the STO surface and desorption of surface contaminants. This annealing step further helped to enhance the reproducibility of thermal coupling between substrate and sample holder, which were fixed to each other with silver paste. Moreover, if STO was heated in vacuum instead of oxygen, we observed slight intermediate streaks in the RHEED pattern (not shown here), which we explain by the formation of a superstructure, possibly an oxygen-deficient phase. After STO annealing, the substrate was cooled down in $p_{O_2} = 10$ Pa oxygen to $T = 700\,^{\circ}$C with a rate of $\delta T/\delta t = -40\,^{\circ}$C/min. The power of the heating diode laser was locked during preablation and ablation, leading to a sample temperature typically in the range of $T = (670–700)^{\circ}$C. The energy of the excimer laser was set to $E_L = 110$ mJ at a target-to-substrate distance $d_{\mathrm{TS}} = 65$ mm. Before ablation, the target was preablated with 500 laser pulses to get a clean and stoichiometric surface. Then 900 pulses at a repetition rate of $f_L = 2$ Hz were used for deposition of the BTO film. As the morphology of BTO is of great importance for the properties of the SLCO films, the as-deposited BTO films had to be annealed. Therefore the sample was heated up with $\delta T/\delta t = 40\,^{\circ}$C/min in deposition pressure $p_{O_2} = 10$ Pa to $T = 900\,^{\circ}$C and annealed for $t_a = 15$ min. We found that heating and anneling in oxygen is essential because bare vacuum annealing led to the formation of a superstructure, probably an oxygen deficient phase, as observed by the formation of intermediate streaks in the RHEED pattern (not shown here). After oxygen annealing, the oxygen was turned off and the samples were annealed additionally for $t_a = 30$ min in vacuum at $T = 900\,^{\circ}$C to remove possible excess oxygen from BTO, which could diffuse into the SLCO and hamper the reduction of the latter. An analysis of the BTO annealing procedure will be given in Sec. III A 1. After oxygen and vacuum annealing, the BTO films were cooled down in vacuum

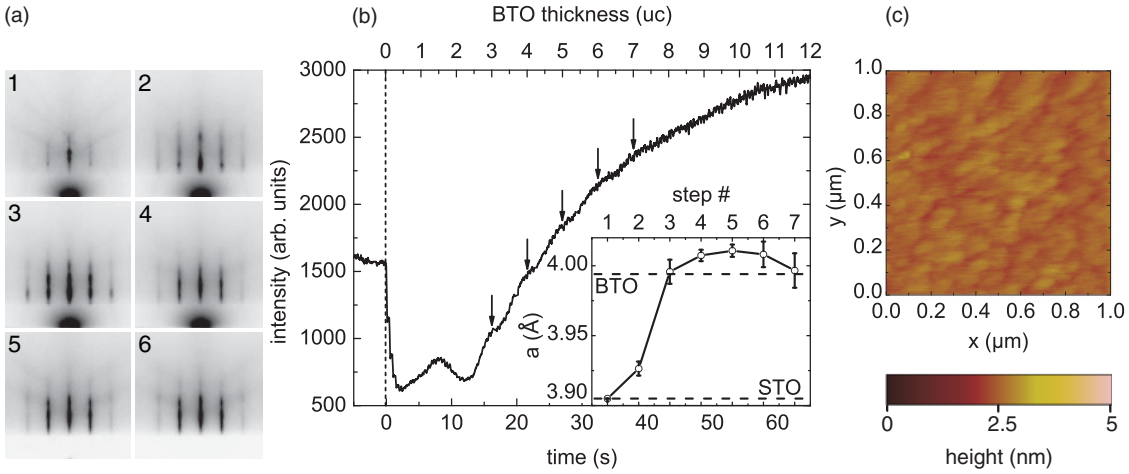

FIG. 1. (Color online) (a) RHEED patterns during preparation of BTO. (1) STO substrate before deposition, (2) BTO after growth of approximately 2 unit cells, (3) end of BTO deposition, (4) begin of BTO oxygen annealing, (5) begin of BTO vacuum annealing, and (6) end of BTO vacuum annealing. (b) Main graph shows intensity oscillations of the RHEED specular spot during growth of BTO (arrows). Inset shows the evolution of the in-plane lattice constant a_{BTO} during preparation of BTO as derived from RHEED patterns illustrated in (a). The value of step 7 was determined after cooling the sample in vacuum. Horizontal lines indicate the in-plane lattice constants of STO (literature value 3.905 Å) and BTO (determined by XRD, 3.994 Å). (c) AFM image of the BTO surface. The root mean square roughness is 0.15 nm and the maximum step height is 0.8 nm, corresponding to 2 uc BTO.

($p_{\mathrm{vac}} \lesssim 10^{-5}$ Pa) at a rate of $\delta T/\delta t = -20\,^{\circ}$C/min to the deposition temperature of SLCO.

B. Deposition of SLCO on BTO buffered STO

The SLCO films were deposited *in situ* after BTO had been deposited on STO as described in Sec. II A. At $T = 550\,^{\circ}$C, the pressure was increased to $p_{\mathrm{O_2}} = 20$ Pa. The power of the heating diode laser was locked during preablation and ablation, resulting in a temperature of $T = (575 \pm 10)\,^{\circ}$C. To minimize reoxidation of the previously vacuum annealed BTO film, the preablation of SLCO was started immediately after turning on the oxygen flow. The excimer laser was set at $f_L = 2$ Hz at an energy of $E_L = 130$ mJ and the target-to-substrate distance to $d_{\mathrm{TS}} = 60$ mm. 500 pulses were preablated and 600–850 pulses were ablated. To remove excess oxygen incorporated during SLCO growth, the oxygen flow was turned off immediately after deposition and the sample was annealed in vacuum for typically $t_a = (20 \pm 5)$ min. During vacuum annealing, the temperature increased to $T = (600 \pm 10)\,^{\circ}$C and the pressure decreased to $p_{\mathrm{vac}} \approx 10^{-5}$ Pa. The streaky RHEED pattern got more pronounced but slight intermediate streaks, formed during deposition probably due to excess oxygen, did not vanish completely [cf. Fig. 3(a)]. After vacuum annealing, the heating diode laser was turned off and the sample cooled down in vacuum to room temperature within $t \approx 1$ h.

C. Deposition of SLCO on KTO

Contrary to STO, KTO substrates were not annealed in vacuum at high T prior to deposition, because it is known that such annealing leads to the formation of a rough surface, probably due to the formation of reduced forms of tantalum oxide on the surface.[31] Thus, KTO was heated up in vacuum ($p_{\mathrm{vac}} \approx 10^{-5}$ Pa) to $T = 550\,^{\circ}$C at a heating rate of $\delta T/\delta t = 10\,^{\circ}$C/min. Then, the pressure inside the PLD chamber was increased to $p_{\mathrm{O_2}} = 20$ Pa and the power of the heating diode laser was locked, leading to a substrate temperature of $T = (580 \pm 10)\,^{\circ}$C. The target-to-substrate distance was adjusted to $d_{\mathrm{TS}} = 60$ mm and the energy of the excimer laser to $E_L = 130$ mJ at a repetition rate of $f_L = 2$ Hz; 500 and 850 pulses were preablated and ablated, respectively. To remove excess oxygen, the oxygen flow was turned off immediately after deposition and the sample was vacuum annealed for typically $t_a = (10 \pm 5)$ min. During annealing, the pressure decreased to $p_{\mathrm{vac}} \approx 10^{-5}$ Pa and the temperature increased to $T = (605 \pm 5)\,^{\circ}$C. Finally, the heating diode laser was turned off and the sample cooled down to room temperature.

III. CHARACTERIZATION OF THIN FILMS

In this section, typical properties of the BTO and SLCO films are presented. For simplicity, only representative measurements are shown and discussed. The influence of different process parameters on the final film properties will be discussed in Sec. IV.

A. Characterization of BTO on STO

1. *RHEED and atomic force microscopy*

During deposition, heating and annealing, the evolution of the in-plane lattice constant a_{BTO} and the morphology of the BTO films were analyzed by means of RHEED, as shown in Figs. 1(a) and 1(b). By use of Bragg' law ($2a \sin\theta_n = n\lambda$, where θ_n is the angle of the nth order maximum and λ the de Broglie wavelength of the diffracted electrons), a_{BTO} can be determined. Small-angle approximation yields $a_{\mathrm{BTO}}/a_{\mathrm{STO}} \approx \theta_{n,\mathrm{STO}}/\theta_{n,\mathrm{BTO}}$. With the lattice parameter $a_{\mathrm{STO}} = 3.905$ Å (see Ref. 37) and with the angles θ_n extracted from RHEED patterns, we determined a_{BTO}. The inset of Fig. 1(b)

shows the mean value of a_{BTO} determined during growth of ten comparable BTO films. Error bars denote the standard deviation. We found that the first unit cells of BTO were highly compressively strained because after deposition of ~2 uc BTO (cf. step 2 in Fig. 1), the lattice constant was determined as $a_{BTO} \approx 3.92$ Å, which is close to a_{STO}. Yet, due to the large lattice mismatch of 2.2 % between bulk BTO with $a_{BTO} = (3.992 \pm 0.002)$ Å (see Refs. 38 and 39) and STO, the BTO films relaxed during growth, which was observed as an increase of a_{BTO} from its initial value to ~3.99 Å at the end of deposition (step 3). The relaxation of BTO was further directly visible in the RHEED pattern because three-dimensional (3D) signatures occurred in the initially two-dimensional (2D) pattern during deposition (cf. steps 2 and 3). This allows us to identify the growth mode of the BTO films as a mixture of 2D layer by layer and 3D island growth, which is known as Stranski-Krastanov growth.[40] Moreover, this observation is in accordance with the disappearance of intensity oscillations of the RHEED specular spot after ~5 uc, as depicted in Fig. 3(b). During subsequent heating in oxygen (steps 3 and 4) and annealing in oxygen (steps 4 and 5), a smoothing of the BTO surface was observed because 3D admixtures diminished, leaving a mostly streaky, 2D pattern with Kikuchi lines. Moreover, a_{BTO} increased to ~4.00 Å after oxygen annealing (step 4). Such an increase of a, usually going along with a decrease of c, is a common feature observed during oxidation of oxides.[41] During vacuum annealing (steps 5 and 6) and cooling (steps 6 and 7) the BTO film was reduced, resulting in a decrease of a_{BTO} to its final value of ~3.995 Å. As RHEED is a surface sensitive method, contrary to XRD, the final in-plane lattice constant $a_{BTO} \approx 3.995$ Å indeed corresponds to the *uppermost* unit cells, which are decisive for epitaxial growth of SLCO. In conclusion, tensile strain can be provided to SLCO by use of BTO as buffer layer.

The morphology of the BTO films was furthermore examined by AFM. As shown in Fig. 1(c), AFM revealed a very smooth surface with a root mean square roughness RMS ≈ 0.15 nm and a maximum step height of ~0.8 nm. This result corresponds to steps of 1 to 2 uc and is in accordance with a smooth BTO surface as observed by RHEED.

2. *X-ray diffraction*

Figure 2 shows XRD data of a typical BTO film on STO. The film is aligned along the *a*/*b* axis of STO, as found by Φ scans around the sample normal (not shown here). The BTO (002) peak yields a *c* axis constant of 4.041 Å. Interference fringes around the (002) peak of BTO in Fig. 2(a), known as Laue oscillations,[42] indicate high crystalline quality along the film normal and a flat surface. Narrow rocking curves with typical full width at half maximum FWHM ≈ 0.1 ° [cf. inset of Fig. 2(a)] confirm the high crystalline quality of the films.

The reciprocal space map in the main graph of Fig. 2(b) yields an in-plane lattice constant of $a_{BTO} = 3.989$ Å. As XRD provides integral information on the crystal structure, the very sharp BTO (303) peak without any extension along the (100) direction shows that the major part of the film is relaxed. This observation is in accordance with the RHEED results presented in Sec. III A 1, which showed that the film was almost fully relaxed after annealing.

The inset of Fig. 2(b) displays the correlation of the lattice parameters a_{BTO} and c_{BTO} for ~60 BTO films prepared under varying conditions. In particular, the deposition temperature was varied between $T = 650$ and 750 K and some films were only annealed in oxygen, whereas others were additionally annealed in vacuum. These variations most likely result in BTO films with varying oxygen content. As commonly known, an increase of a_{BTO} leads to a decrease of c_{BTO}, which is ascribed to an increasing degree of oxidation. This assumption will be confirmed in Sec. IV A. We determined mean values of $a_{BTO} = (3.994 \pm 0.006)$ Å and $c_{BTO} = (4.026 \pm 0.011)$ Å, which are close to the bulk lattice constants $a_{BTO} = (3.992 \pm 0.002)$ Å and $c_{BTO} = (4.031 \pm 0.002)$ Å,[38,39] confirming that the BTO films are relaxed. Note that the XRD value of a_{BTO} coincides with the *surface* value determined by RHEED (cf. Sec. III A 1). Thus the surface layer is coherently relaxed with the bulk. However, RHEED oscillations of the specular spot, observed at the beginning of deposition, yielded an extrapolated film thickness of (79 ± 4) uc, i.e., $t_{BTO} = (32 \pm 2)$ nm, whereas Laue oscillations of XRD Θ-2Θ scans revealed a film thickness typically 2–3 nm smaller than the value determined by RHEED. This points to a thin layer, which

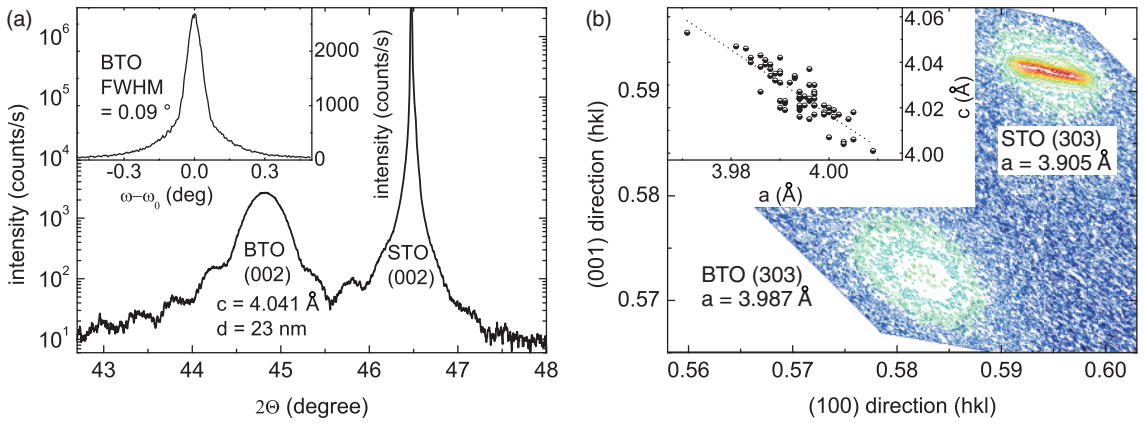

FIG. 2. (Color online) XRD data of BTO on STO. (a) Main graph shows the (002) region of a Θ-2Θ scan and inset shows the rocking curve of the BTO (002) peak. (b) Main graph shows reciprocal space mapping of the (303) region of SLCO and BTO. Inset displays the linear dependence of the BTO lattice parameters a_{BTO} and c_{BTO}. The dashed line is a linear fit.

is noncoherently strained with the bulk. We interpret this as a compressively strained BTO layer close to the interface with STO. As known from literature, such an interface layer does exist and it comprises most of the dislocations.[43] It is likely that such a strained interface layer does not contribute to Laue oscillations.

To conclude Sec. III A, we found that the BTO films have a flat and relaxed surface, which makes them suitable to be used as buffer layers for epitaxial growth of tensile strained SLCO films.

B. Characterization of SLCO on BTO/STO

1. RHEED and atomic force microscopy

For SLCO films deposited on BTO/STO, typically (20 ± 10) intensity oscillations of the RHEED specular spot could be observed before they vanished [cf. Fig. 3(b)]. The RHEED oscillations revealed a growth rate of (8.2 ± 0.5) pls/uc, yielding a film thickness of $t_{SLCO} = (26 \pm 2)$ nm for 600 pulses. At the end of deposition, sharp and streaky RHEED patterns with some fade 3D dots as a result of increased surface disorder were observed as illustrated in Fig. 3(a). As in the case of BTO, this implies a Stranski-Krastanov growth mode. However, weak intermediate streaks in the RHEED pattern could be observed during film growth that did not vanish during annealing [cf. Fig. 3(a)]. Note that for identical settings, those streaks did not appear when SLCO was deposited on KTO. The possible origin of the streaks will be discussed in Sec. IV C 1, hinting at excess oxygen that could not be removed.

The inset of Fig. 3(b) illustrates the evolution of the in-plane lattice constant a_{SLCO} during deposition and annealing of SLCO, where step 7 corresponds to step 7 of Fig. 1. The data were acquired from ten samples fabricated under similar conditions and the error bars represent the standard deviation. As derived from step 8, SLCO begins to relax immediately. At the end of deposition, it has an in-plane lattice constant of $a_{SLCO} \approx 3.93$ Å, which is remarkably small as compared to the bulk value of 3.967 Å determined by XRD after vacuum annealing (cf. Sec. III B 2). We explain this as follows. During deposition, excess oxygen is incorporated in the SLCO film, leading to an elongated c axis and a shortened a axis. During vacuum annealing, excess oxygen desorbs, leading to an increase of the a axis, as observed by RHEED in steps 10 and 11. However, the SLCO bulk value determined by XRD is not reached. This discrepancy is supposedly due to the fact that RHEED is a surface-sensitive method, yielding different lattice parameters than found for the bulk because of different surface structure or composition. Indeed, in a recent paper, we have proven the existence of a thin (∼3 nm), oxygen deficient SLCO surface layer, which most probably forms during vacuum annealing.[44] Such a reduced SLCO surface layer explains well the small in-plane parameter a_{SLCO} observed by RHEED.

Additionally to RHEED, we checked the morphology of the SLCO films with AFM. A typical AFM image is shown in Fig. 3(c). The RMS was determined as 0.35 nm and the maximum step height as 1.0 nm, corresponding to 3 uc SLCO. Therefore the film is quite flat, confirming the RHEED results.

2. X-ray diffraction

Figure 4(a) shows an XRD Θ-2Θ scan of a typical BTO-buffered SLCO film. From the position of the SLCO (002) reflection, the c-axis parameter is calculated as 3.412 Å. A set of comparable films with T_c close to 20 K [cf. inset of Fig. 4(b)] revealed a mean value of $c_{SLCO} = (3.408 \pm 0.002)$ Å, which is close to the value reported for $Sr_{0.9}La_{0.1}CuO_2$ films on DSO substrates (∼3.410 Å).[23] As deduced from Laue oscillations of the SLCO (002) peak and from narrow rocking curves [cf. Fig. 4(a)], the films have a high crystalline quality and a flat surface. Large angle Θ-2Θ scans (2Θ = 0–90 °) revealed only

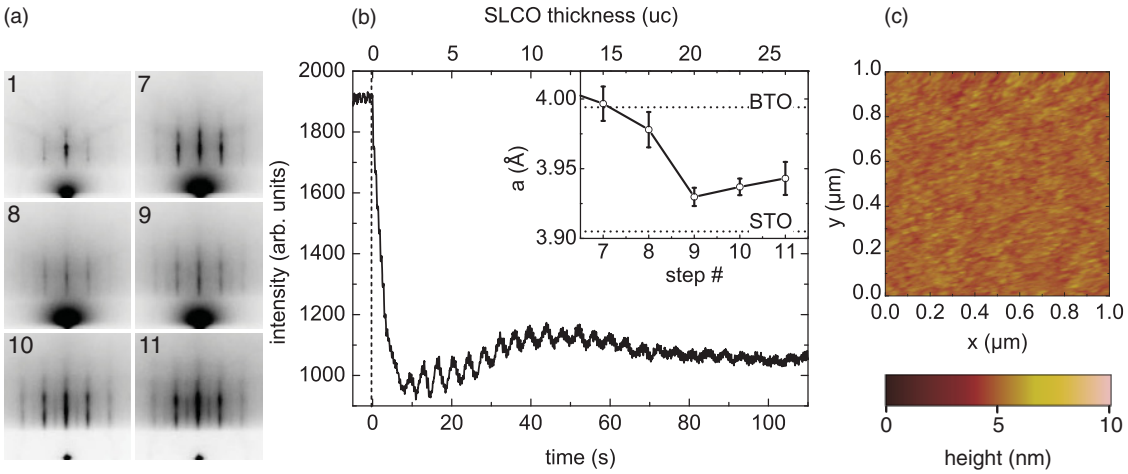

FIG. 3. (Color online) (a) RHEED patterns during preparation of SLCO on BTO/STO. (1) STO substrate before deposition, (7) BTO buffer layer before SLCO deposition, (8) SLCO after growth of ∼2 unit cells, (9) end of SLCO deposition, (10) begin of SLCO vacuum annealing, and (11) end of SLCO vacuum annealing. (b) Main graph shows intensity oscillations of the RHEED specular spot during growth of SLCO on BTO/STO. Deposition started at $t = 0$. Inset shows the evolution of the in-plane lattice constant a_{SLCO} during preparation of SLCO as derived from RHEED patterns illustrated in (a). Steps 1–7 are discussed in Sec. III A1. Horizontal lines indicate the in-plane lattice constants of STO (literature value 3.905 Å) and BTO (mean value determined by XRD, 3.994 Å). (c) AFM image of the SLCO surface. The root mean square roughness is 0.35 nm and the maximum step height is 1.0 nm, corresponding to 3 uc SLCO.

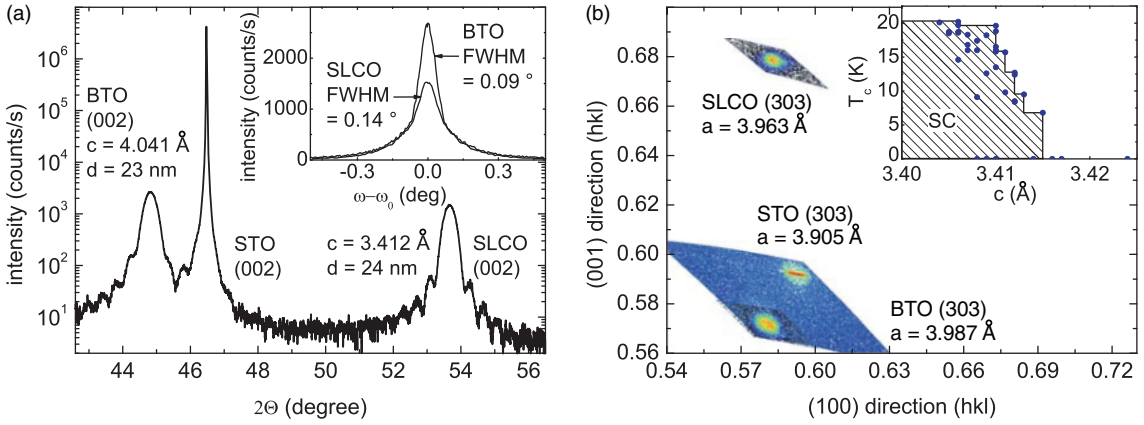

FIG. 4. (Color online) XRD data of SLCO on BTO/STO. (a) Main graph shows the (002) region of a Θ-2Θ scan and inset shows the rocking curve of the SLCO (002) and BTO (002) peaks. (b) Main graph shows reciprocal space mapping of the (303) region. Inset displays T_c vs c-axis parameter for a set of SLCO films grown under comparable conditions. Superconductivity (SC) is expected only to occur within the shaded region.

one phase, confirming that the SLCO film is single phase with IL crystal structure. All films are aligned along the *a*/*b* axis of STO, as found by Φ scans around the sample normal (not shown here).

With the aid of two-axes scans around the SLCO (303) reflection, as shown in the main graph of Fig. 4(b), we determined the in-plane lattice constant $a_{\mathrm{SLCO}} = 3.963$ Å. The films with T_c close to 20 K exhibited a mean value of $a_{\mathrm{SLCO}} = (3.967 \pm 0.002)$ Å, which is somewhat larger than the reported value of 3.955 Å for $Sr_{0.1}La_{0.9}CuO_2$ films on DSO.[23] However, as compared to the BTO buffer layers with a mean value of $a_{\mathrm{BTO}} = 3.994$ Å (cf. Sec. III A 2), a_{SLCO} is rather small. We explain this difference primarily by the interplay of lattice mismatch (between BTO and SLCO) inducing tensile strain, and excess oxygen inducing compressive strain. Other influences, such as (off-)stoichiometry (different ionic radii) might also contribute to the final value of a_{SLCO}. Altogether, this results in SLCO films on BTO/STO with inferior tensile strain, as illustrated in the main graph of Fig. 4(b), where a shift of the SLCO (303) peak along the (100) direction with respect to the BTO (303) peak is visible.

The inset of Fig. 4(b) shows the correlation of the transition temperature T_c and the out-of-plane lattice constant c_{SLCO} for a set of SLCO films fabricated under comparable conditions. No superconducting transition was observed for $c_{\mathrm{SLCO}} > 3.415$ Å and T_c was highest for smallest c_{SLCO}. This observation is explained by the amount of incorporated excess oxygen, which expands the c axis and hampers superconductivity, as described in Sec. I. We explain data points well inside the shaded region by nonideal process conditions, e.g., by too high vacuum annealing temperature, leading to oxygen vacancies in the CuO_2 planes, which again decreases T_c. We note that more films followed this trend, however, for clarity, we only show data points for films prepared under comparable conditions as described in Sec. II B.

3. *Rutherford backscattering spectroscopy*

To determine the stoichiometry of the BTO-buffered SLCO films, we performed RBS on two samples.[36] The first sample had a thickness of 24 nm and a T_c of 14.9 K. As determined by XRD, the lattice parameters were $a_{\mathrm{SLCO}} = 3.963$ Å and $c_{\mathrm{SLCO}} = 3.411$ Å, i.e., the film had a slight amount of excess oxygen. Simulations showed that the separation of the La and the Ba peak in the backscattering spectrum is stronger for lower α energies.[36,45] For this reason, measurements were performed at 1213 keV. The resolution of the detector at this energy is 20 keV 1213 keV = 1.6 %. Two independent measurements yielded consistent data and were performed to allow for a deduction of the double standard deviation 2σ. The data were fitted numerically using a simplex algorithm.[45] The measurements are shown in Fig. 5 and the results are summarized in Table I. Note, that the Sr peak (at ∼1000 keV) stemming from the SLCO film is separate from the Sr box (ending at ∼970 keV) stemming from the STO substrate because of the energy loss of α particles crossing the intermediate BTO film.

For stoichiometric SLCO with a sum formula $Sr_{1-x}La_xCuO_2$, the sum of Sr and La atoms equals the number of Cu atoms. In our case, it is $(29.4 + 5.3) \times 10^{15}$ atoms/cm^2 $= 34.7 \times 10^{15}$ atoms/cm^2, which is

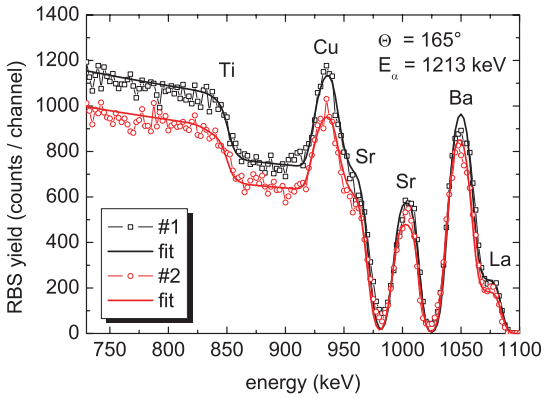

FIG. 5. (Color online) Two Rutherford backscattering spectra (open symbols) of an SLCO film on BTO/STO measured in two independent runs (1 and 2). Solid lines are numerical fits to the data. The determined stoichiometry is given in Table I.

TABLE I. Areal density (in units of 10^{15} atoms/cm^2) as determined by numerical fits of RBS data measured on a BTO-buffered SLCO film on STO. The two independent measurements are labeled as 1 and 2. Errors of the numerical fits are denoted in parentheses. The error of the mean value is the double standard deviation 2σ.

Meas.	Sr	La	Cu
1	29.34(9.78)	5.40(0.13)	36.21(12.07)
2	29.46(9.77)	5.11(0.14)	34.57(11.47)
mean	29.39[0.11]	5.25[0.29]	35.39[1.64]

very close to the determined amount of Copper (35.4×10^{15} atoms/cm^2). Therefore an off-stoichiometry between (Sr/La) and Cu can be excluded within experimental accuracy. Thus, from RBS data, we extract a sum formula $Sr_{0.84}La_{0.16}CuO_2$, showing that the sample is overdoped with respect to the doping level of the target ($x = 0.125$). The second sample examined by RBS yielded similar results with $x = 0.14$. Note that RBS fits have only been performed on the high-energy part of the spectrum where the peaks of Ti, Cu, Sr, Ba, and La are visible and not for the low-energy part where the oxygen peak is visible. To summarize our RBS measurements, we determined the doping level of BTO-buffered SLCO films as $x \approx 0.15$, i.e., the samples are overdoped with respect to the doping level reported for SLCO films exhibiting maximum T_c ($x_{opt} = 0.10$)[22] and to the solid solution level reported for polycrystalline bulk SLCO ($x_{sol} = 0.10$).[8] Note that the maximum T_c of our SLCO films was 22 K, which can be explained by overdoping. However, other influences such as excess oxygen or defects may also contribute to a reduction of T_c from its maximum value of 43 K.

4. Electric transport measurements

Figure 6 shows a typical $\rho(T)$ curve of an unpatterned SLCO film on BTO/STO. The superconducting transition at $T_c = 16.8$ K has a width of $\Delta T_c \approx 1$ K. The highest T_c achieved was 22 K. The room-temperature resistivity is $\rho_{300K} \approx 0.2$ mΩcm, which is comparable to the values reported for $YBa_2Cu_3O_{7-\delta}$ single crystals and high-quality thin films. We further observed an almost linear $\rho(T)$ dependence for $T \gtrsim 100$ K, which was explained by scattering due to spin fluctuations in the CuO_2 planes in case of $YBa_2Cu_3O_{7-\delta}$.[46] The residual resistance ratio is RRR ≈ 2, which is somewhat lower than the value reported for optimally doped $Sr_{0.90}La_{0.10}CuO_2$ films on KTO, where RRR ≈ 3.[22] Possible explanations for the reduced T_c and RRR are excess oxygen in the (Sr/La) planes, oxygen deficiency in the CuO_2 planes, lattice defects, impurities, or off-stoichiometry. As shown in Sec. IV, both excess oxygen and oxygen deficiency lead to semiconducting or insulating $\rho(T)$ behavior. Moreover, lattice defects or impurities lead to a finite resistance at low temperatures, where electron-phonon scattering is negligible, leading to a reduced RRR. After $\rho(T)$ measurement, the SLCO film was patterned to allow for determination of the critical current density $j_c(T)$. The $\rho(T)$ behavior measured with these bridges (not shown here) coincided with the $\rho(T)$ behavior determined by van der Pauw measurement prior to patterning, which confirms that patterning did not affect the properties of SLCO. We measured

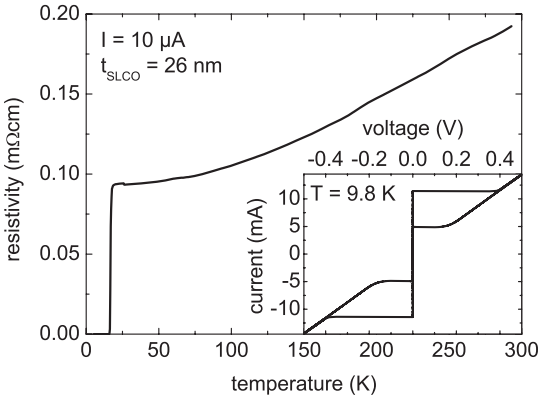

FIG. 6. Resistivity vs temperature of an unpatterned SLCO film on BTO/STO. Inset shows the current-voltage characteristics of a 40 μm wide bridge at $T = 9.8$ K.

$I(V)$ curves in the temperature range $4.2\,\mathrm{K} \leqslant T \leqslant T_c$, as shown in the inset of Fig. 6 for $T = 9.8$ K. The $I(V)$ curves were hysteretic, probably due to heating. At $T = 4.2$ K, we found a critical current density $j_c(4.2\,K) = 2.1 \times 10^6$ A/cm^2, which is 1 to 2 orders of magnitude lower than the values reported for YBCO at $T = 4.2$ K but coincides with that of T' compounds such as $Nd_{2-x}Ce_xCuO_4$.[47]

C. Characterization of SLCO on KTO

1. RHEED and atomic force microscopy

During initial growth of SLCO on KTO, typically (10 ± 5) RHEED oscillations could be observed, as displayed in Fig. 7(b). This value is somewhat lower than what is found for SLCO on BTO/STO (cf. Sec. III B 1). A possible explanation is given by the fact that KTO was not vacuum annealed before deposition of SLCO, leading to enhanced island growth (increased step density) due to worse substrate-film interface and thus to a faster disappearance of RHEED oscillations. The oscillations revealed a growth rate of (8.5 ± 1.0) pls/uc, corresponding to a film thickness of $t_{SLCO} = (34 \pm 4)$ nm for 850 pulses. At the end of deposition, the RHEED pattern revealed a 2D surface with fade 3D admixtures, possibly due to 3D islands or small droplets on the surface [cf. Fig. 7(a)]. Together with the intensity evolution of the specular spot, we can thus identify a Stranski-Krastanov growth mode.[40] Note, that for SLCO films on KTO, no intermediate streaks were observed, which is different from what we found for SLCO films on BTO/STO.

Figure 7(c) shows an AFM image of SLCO on KTO. The root mean sqaure roughness is RMS = 0.35 nm and the maximum step height is $\sim$1.0 nm, i.e., the maximum roughness is caused by asperities of 3 uc. The morphology of SLCO on KTO is thus comparable to the morphology of SLCO on BTO/STO. Note that extra structures visible in the AFM image, i.e., bright lines and dark holes, stem from the KTO substrate, which was not annealed prior to deposition.

2. X-ray diffraction

A typical XRD Θ-2Θ scan of SLCO on KTO is shown in the main graph of Fig. 8(a), indicating that the film is single phase with an IL crystal structure. About ten Laue oscillations can be

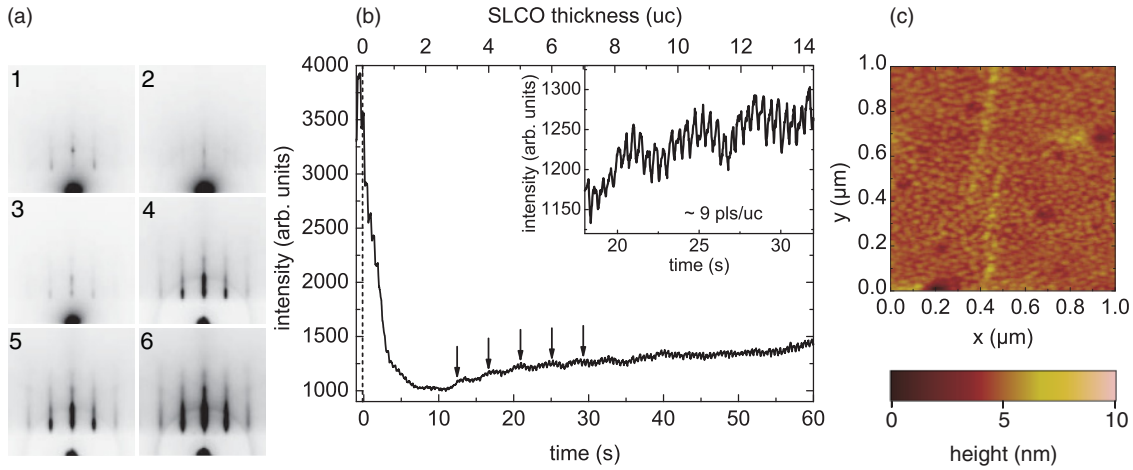

FIG. 7. (Color online) (a) RHEED patterns during preparation of SLCO on KTO. (1) KTO substrate before deposition, (2) SLCO after growth of ∼2 unit cells, (3) end of SLCO deposition, (4) begin of SLCO vacuum annealing, (5) end of SLCO vacuum annealing, and (6) sample at room temperature. (b) Intensity oscillations of the RHEED specular spot during growth of SLCO on KTO (marked by arrows). Deposition started at $t = 0$. Inset presents a zoom, showing growth of ∼3 uc in detail. (c) AFM image of the SLCO surface. The root mean square roughness is 0.35 nm and the maximum step height is 1.0 nm, corresponding to 3 uc SLCO. The darker regions stem from holes in the as-received KTO substrate.

identified, pointing to a uniform crystal structure along the c axis and a flat film surface. Moreover, the narrow rocking curve with FWHM $= 0.09^\circ$ demonstrates high crystalline quality of the film. The c-axis parameter is calculated as 3.400 Å. For comparable films, exhibiting T_c close to 20 K, the mean value was $c_{\mathrm{SLCO}} = (3.401 \pm 0.005)$ Å, which coincides well with the value $c = (3.400 \pm 0.003)$ Å reported for $Sr_{0.9}La_{0.1}CuO_2$ films on KTO.[23,48]

Reciprocal space mapping around the (303) reflection was used to determine the in-plane lattice parameter a_{SLCO}. As displayed in Fig. 8(b), the SLCO film is under tensile epitaxial strain with $a_{\mathrm{SLCO}} = 3.986$ Å, which is close to the substrate parameter $a_{\mathrm{KTO}} = 3.988$ Å. The mean value for films with T_c close to 20 K was $a_{\mathrm{SLCO}} = (3.982 \pm 0.004)$ Å, which is somewhat larger than the value (3.972 ± 0.006) Å reported for $Sr_{0.9}La_{0.1}CuO_2$ films on KTO.[23,48]

The inset of Fig. 8(b) shows the dependence of T_c on the lattice constant c_{SLCO}. As found for SLCO on BTO/STO (cf. Sec. III B2), an upper limit for c_{SLCO} where superconductivity occurs can be identified empirically ($c_{\mathrm{SLCO}} \leqslant 3.415$ Å).

We now compare the XRD data of SLCO films on BTO/STO (cf. Sec. II B2) with XRD data of SLCO films on KTO. Table II comprises a summary of XRD data typically measured for SLCO films grown on both types of substrates. It is obvious that SLCO films on KTO show higher peak intensities, narrower rocking curves and more Laue oscillations, i.e., better crystalline quality. More important, the a axis (c axis) is larger (smaller) for SLCO films on KTO, resulting in a smaller ratio $c/a = 0.854$ for SLCO films on KTO, compared to 0.859 for SLCO films on BTO/STO, i.e., SLCO films on KTO are more tensile strained. It is thus remarkable that both kinds of samples exhibit similar electric transport properties

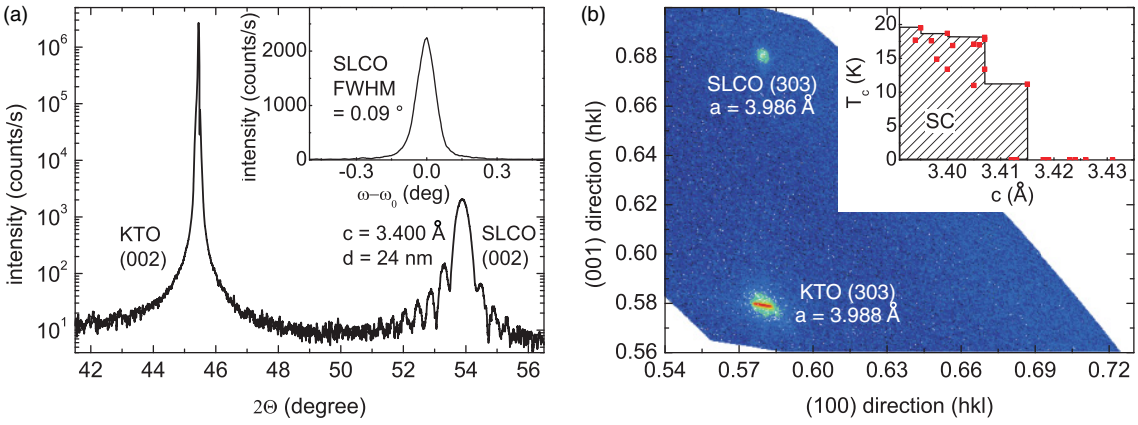

FIG. 8. (Color online) XRD data of SLCO on KTO. (a) Main graph shows the (002) region of a Θ-2Θ scan and inset shows the rocking curve of the SLCO (002) peak. (b) Main graph shows reciprocal space mapping of the (303) region. Inset displays T_c vs c-axis parameter for a set of SLCO films grown under comparable conditions. Superconductivity (SC) is only observed within the shaded region.

TABLE II. Comparison of typical XRD data for SLCO films grown on different substrates. All data refer to the (002) reflection. The FWHM corresponds to the rocking curve and the number of Laue oscillations (osc.) to the Θ-2Θ scan. c_{SLCO} and a_{SLCO} are the mean values of films with $T_c \approx 20$ K.

Substrate	Intensity (cps)	FWHM (deg)	osc.	c_{SLCO} (Å)	a_{SLCO} (Å)
BTO/STO	∼1000	∼0.15	∼4	3.408	3.967
KTO	∼2000	∼0.11	∼8	3.401	3.982

(cf. Sec. III C 3), in particular the same maximum $T_c \approx 20$ K, whereupon tensile strain was believed to enhance electron doping of the CuO_2-planes and therefore increase T_c.[7,17,19,22] For illustration, Fig. 9 shows the correlation of the transition temperature T_c vs c/a ratio for SLCO films deposited on both kinds of substrates. It is obvious, that SLCO films on BTO/STO are superconducting for $c/a \lesssim 0.862$, whereas SLCO films on KTO are superconducting for $c/a \lesssim 0.858$. To explain this difference, we refer to the work of Karimoto *et al.*; on the one hand, they showed that *compressively strained* SLCO films on STO are not superconducting,[17,22] whereas *tensile strained* SLCO films on KTO are superconducting with $T_c^{zero} = 39$ K. On the other hand, they found that *relaxed* SLCO films on DSO exhibit slightly improved electric transport properties with $T_c^{zero} = 41$ K.[23] Thus, whereas compressive strain hampers superconductivity, both relaxed and tensile strained films exhibit comparable superconducting properties. Therefore despite exhibiting different degrees of tensile strain, it is in accordance with literature that our SLCO films show comparable electric transport properties.

3. Electric transport measurements

Figure 10 shows $\rho(T)$ of an SLCO film on KTO with $T_c = 18.0$ K. The transition width is $\Delta T_c \approx 1$ K. The room-temperature resistivity is $\rho_{300K} = 0.16$ mΩcm and RRR ≈ 2. We observed hysteretic $I(V)$ curves, as shown in the inset of Fig. 10 for $T = 10$ K. At $T = 4.2$ K, we found a critical current density $j_c(4.2\,K) = 2.0 \times 10^6$ A/cm^2, which is comparable to the value found for SLCO on BTO/STO, cf.

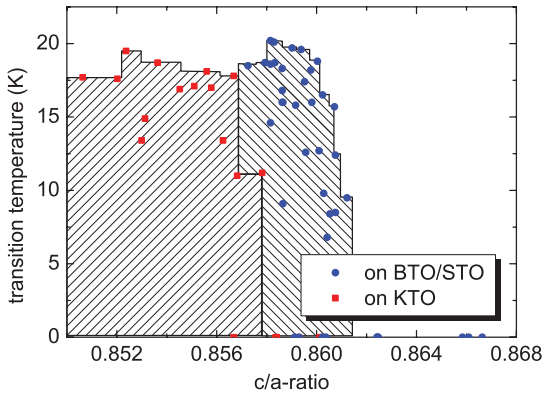

FIG. 9. (Color online) Transition temperature T_c vs c/a ratio for SLCO on BTO/STO and on KTO. The shaded regions, where superconductivity is found to occur, clearly reveal two different regimes of tensile strain.

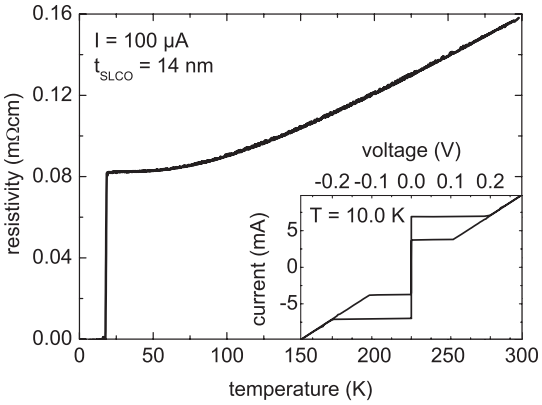

FIG. 10. Resistivity vs temperature of an unpatterned SLCO film on KTO. Inset shows current-voltage characteristics of a 40 μm wide bridge at $T = 10.0$ K.

Sec. III B 4. Altogether, despite of slightly superior crystalline properties of SLCO films on KTO, their electric transport properties are quite similar to those of SLCO films on BTO/STO.

IV. DISCUSSION OF PROCESS PARAMETERS AND VACUUM ANNEALING

In this chapter, the influence of different process parameters on structural and electric properties of BTO and SLCO films are discussed.

A. Influence of process parameters on BTO

1. Substrate temperature

We examined the influence of the substrate temperature T_{BTO} during deposition of BTO on its final lattice parameters. BTO films grown at comparable temperatures $T_{BTO} = (670 \pm 15)\,^\circ$C and oxygen pressure $p_{O_2} = 10$ Pa were analyzed by means of XRD. The lattice parameters were determined as $a_{BTO} = (3.994 \pm 0.003)$ Å and $c_{BTO} = (4.021 \pm 0.003)$ Å. Another set of samples grown at higher substrate temperature $T_{BTO} = (760 \pm 15)\,^\circ$C revealed lattice parameters of $a_{BTO} = (3.988 \pm 0.006)$ Å and $c_{BTO} = (4.033 \pm 0.007)$ Å. Thus, for increasing substrate temperature, the c axis increases and the a axis decreases. As known from literature, reduction of BTO results in an increased c/a ratio. We therefore interpret our result as follows. At high T, oxygen is more mobile than at low T, leading to an enhanced desorption of oxygen already during film growth. The films deposited at high T are consequently more reduced and have a larger c/a ratio than those grown at low T.

Moreover, by means of RHEED, we found that a superstructure emerged when BTO was deposited at $T_{BTO} \lesssim 650\,^\circ$C, which may be the result of surface defects. Therefore, for the deposition pressure $p_{O_2} = 10$ Pa, T_{BTO} values higher than 650 °C were used.

2. Vacuum annealing

As described in Sec. II A, BTO films were annealed at $T_a \approx 900\,^\circ$C in oxygen ($p_{O_2} = 10$ Pa) for $t_a = 15$ min and subsequently at the same temperature in vacuum ($p_{vac} \lesssim$

10^{-5} Pa) for $t_a = 30$ min. To examine the influence of this vacuum annealing step on the lattice constants, we also fabricated some reference samples that were only annealed in oxygen but not in vacuum. Those films revealed a larger in-plane lattice constant $a_{\mathrm{BTO}} = (3.992 \pm 0.005)$ Å and a smaller out-of-plane lattice constant $c_{\mathrm{BTO}} = (4.026 \pm 0.013)$ Å as compared to the films *with* additional vacuum annealing [$a_{\mathrm{BTO}} = (3.988 \pm 0.006)$ Å and $c_{\mathrm{BTO}} = (4.033 \pm 0.007)$ Å]. From this observation we can conclude that reduction by vacuum annealing leads to an increase of the c/a ratio, in accordance with literature. Furthermore, it supports the interpretation given in Sec. IV A 1.

B. Influence of process parameters on SLCO

1. Excimer laser energy

In this section, we report on the influence of the excimer laser energy E_L on SLCO films. For that purpose, we fixed all other parameters and varied E_L. By analyzing the RHEED oscillations during deposition of ~30 SLCO films on BTO/STO, we found that the number of pulses needed to deposit one unit cell SLCO (pls/uc) decreased approximately linearly with increasing laser energy. For a target-to-substrate distance $d_{\mathrm{TS}} = 60$ mm, the values determined during deposition were (9.3 ± 0.5) pls/uc at 110 mJ, (8.2 ± 0.5) pls/uc at 130 mJ, and (6.7 ± 0.5) pls/uc at 150 mJ, as displayed in Fig. 11. It is obvious that higher E_L yields a higher plasma density and thus an increased growth rate.

To analyze the impact of varying laser energy on the lattice parameters, we compare two representative SLCO films on BTO/STO, prepared identically except for E_L. One film was prepared with $E_L = 130$ mJ and the other with $E_L = 150$ mJ. As the growth rate increased with increasing E_L, 550 and 400 pulses were deposited, respectively, to end up with the same film thickness. The resulting lattice parameters were $c_{\mathrm{SLCO}} = 3.410$ Å and $a_{\mathrm{SLCO}} = 3.965$ Å for $E_L = 130$ mJ as well as $c_{\mathrm{SLCO}} = 3.419$ Å and $a_{\mathrm{SLCO}} = 3.962$ Å for $E_L = 150$ mJ,

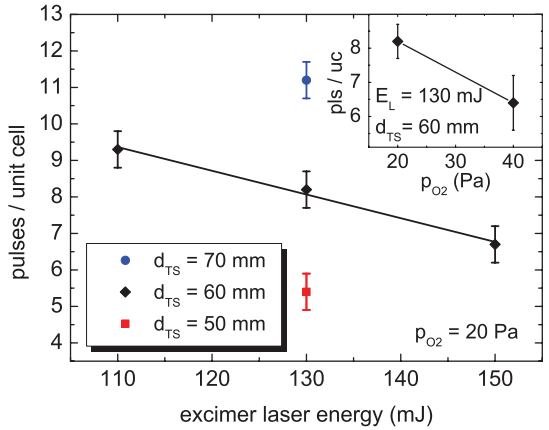

FIG. 11. (Color online) Number of laser pulses needed to deposit one monolayer (determined by RHEED oscillations) of SLCO on BTO/STO at an oxygen pressure $p_{\mathrm{O_2}} = 20$ Pa vs excimer laser energy. The solid line is a linear fit to the data acquired at a target-to-substrate distance $d_{\mathrm{TS}} = 60$ mm. Inset shows the dependence of the growth rate on the oxygen pressure (for fixed $E_L = 130$ mJ and $d_{\mathrm{TS}} = 60$ mm).

i.e., the c/a ratio increased with increasing laser energy. This effect can be attributed to an enhanced incorporation of excess oxygen: a laser pulse with higher E_L creates more high energetic particles in the plasma. Therefore more oxygen is activated in the surrounding process gas and incorporated into the SLCO, which would well explain the increased c/a ratio. However, we can only speculate about this dependence and further examination is needed to verify this assumption.

2. Target-to-substrate distance

Another degree of freedom is given by the distance d_{TS} between target and substrate. It is obvious that an increase of d_{TS} should reduce the growth rate because of the dilution of the plasma in outer regions. Indeed, we observed such behavior by analyzing RHEED oscillations of 25 SLCO films deposited on BTO/STO at similar conditions but with varying d_{TS}. The values for $d_{\mathrm{TS}} = 50, 60$, and 70 mm at fixed $E_L = 130$ mJ were (5.4 ± 0.5), (8.2 ± 0.5), and (11.2 ± 0.5) pls/uc, respectively, as displayed in Fig. 11. As discussed in Sec. IV B 1, higher E_L probably leads to an enhanced incorporation of oxygen. We want to interpret this result in another way: higher E_L leads to an expansion of the plume and consequently to a change of the *relative* position of the substrate within the plume. Actually, this corresponds to a situation, where the laser energy was kept constant but the substrate was moved closer to the target. Thus we expect that the oxygen concentration should increase with decreasing d_{TS}, too. To check this idea, we deposited a film at $d_{\mathrm{TS}} = 50$ mm and another at $d_{\mathrm{TS}} = 70$ mm and compared their lattice parameters. To end up with the same film thickness ($t_{\mathrm{SLCO}} \approx 23$ nm), 350 and 770 pls were ablated, respectively. The resulting lattice parameters were $c_{\mathrm{SLCO}} = 3.410$ Å and $a_{\mathrm{SLCO}} = 3.966$ Å as well as $c_{\mathrm{SLCO}} = 3.406$ Å and $a_{\mathrm{SLCO}} = 3.969$ Å, supporting the above-mentioned idea. To conclude, we found that smaller d_{TS} results in an increased c/a ratio, probably due to enhanced incorporation of excess oxygen.

To remove excess oxygen, we prepared a sample identical to that deposited at $d_{\mathrm{TS}} = 50$ mm but with additional *in situ* vacuum annealing ($t_a = 40$ min) at lower temperature ($T_a \approx 350\,^{\circ}$C). The lattice constants of this sample were $c_{\mathrm{SLCO}} = 3.408$ Å and $a_{\mathrm{SLCO}} = 3.969$ Å, which is close to the parameters of the sample prepared at 70 mm *without* additional low-temperature annealing. This confirms that excess oxygen was indeed responsible for the increase of the c/a ratio, which is both dependent on E_L and on d_{TS}. Finally, we want to mention that the Sr and/or La concentration, i.e., the doping level x, is probably also dependent on E_L and d_{TS}; in a naive approach, the heavier La ($m_{\mathrm{La}} = 138.91$ u)[37] should dominate the inner regions of the plasma because of its high inertia, whereas the lighter Sr ($m_{\mathrm{Sr}} = 87.62$ u)[37] should dominate the outer regions. Yet, a validation of this idea goes beyond the scope of this work.

3. Deposition pressure

To analyze the influence of oxygen pressure on the SLCO films, we prepared films at $p_{\mathrm{O_2}} = 20$ Pa and $p_{\mathrm{O_2}} = 40$ Pa and compared their properties. RHEED oscillations of 25 SLCO films on BTO/STO revealed an increase of the growth rate with increasing $p_{\mathrm{O_2}}$. The values were (8.2 ± 0.5) and (6.4 ± 0.5) pls/uc, respectively, which is illustrated in the inset

of Fig. 11. However, not only the growth rate but also the lattice constants changed. The lattice parameters of a film grown at $p_{O_2} = 20$ Pa were $c_{SLCO} = 3.408$ Å and $a_{SLCO} = 3.969$ Å, while for a film grown at $p_{O_2} = 40$ Pa these values were $c_{SLCO} = 3.412$ Å and $a_{SLCO} = 3.965$ Å. Again, we attribute this increase of the c/a ratio to enhanced incorporation of excess oxygen, which is plausible, because higher oxygen pressure provides more active oxygen during film growth.

C. Vacuum annealing

1. Vacuum annealing time

A series of SLCO films deposited on BTO/STO under similar conditions but with varying vacuum annealing time t_a showed that there is an optimum annealing time $t_a^{opt} = 22$ min. As shown in Fig. 12(a), T_c increases with increasing annealing time and reaches a maximum value of 17.1 K after 22 min, before decreasing again. The room-temperature resistivity ρ_{300K} shows the opposite behavior with a minimum at $t_a^{opt} = 22$ min, which we explain as follows. For $t_a < t_a^{opt}$, excess oxygen is removed from SLCO. As excess oxygen forms O^{2-} ions on interstitial sites, it traps free charge carriers from the CuO_2 planes, which increases the resistivity and suppresses superconductivity. Therefore ρ_{300K} decreases and T_c increases with the removal of excess oxygen, as reported before.[27,48] We further observed the reduction process by analyzing the evolution of the lattice constants with proceeding t_a, as displayed in Fig. 12(b). In accordance with literature[27,48] we found that the c axis decreases and the a axis increases monotonically during reduction. Furthermore, we found that the unit cell volume V increases as well [cf. inset of Fig. 12(b)], which is a well-known behavior of various oxides when being reduced.[41] The decrease of T_c and the increase of ρ_{300K} for $t_a > 22$ min is attributed to the formation of oxygen vacancies in the CuO_2-planes. In hole-doped cuprates, oxygen vacancies in the CuO_2 planes are known to decrease the charge carrier concentration and to weaken the antiferromagnetic spin fluctuation/correlation of the d-electrons, suppressing T_c.[49,50] For the IL compounds, however, it has been shown that oxygen vacancies in the CuO_2 planes can even induce superconductivity.[51,52] The idea is that those vacancies lead to electron doping of the CuO_2 planes, even without trivalent cation doping. However, as oxygen vacancies are lattice defects at the same time, too strong reduction of the CuO_2 planes finally leads to suppression of superconductivity.

In the case of IL, a secondary phase can be formed if oxygen vacancies arrange in an ordered structure, which is called "infinite-layer-related" (IL-r) phase. It can be easily identified by means of XRD due to its elongated c axis of $c_{IL-r} \approx 3.6$ Å. Figure 13(a) shows $\rho(T)$ and an XRD Θ-2Θ scan of the (002) reflection of an SLCO film containing both phases, i.e., the IL and IL-r phase. The c-axis constants are determined as $c_{SLCO} = 3.405$ Å and $c_{IL-r} = 3.614$ Å. The widths of the corresponding rocking curves are $\Delta\omega_{SLCO} = 0.11^\circ$ and $\Delta\omega_{IL-r} = 0.12^\circ$ (not shown here). Laue oscillations of the (002) reflection are visible for both phases, allowing to determine their thickness. For each phase, we found a thickness of (22 ± 1) nm, which is close to the total film thickness determined by RHEED oscillations ($t_{SLCO} \approx 25$ nm). This implies that both phases coexist side by side and not on top of each other. We reported on the same observation in a recent paper.[44] In conclusion, the formation of the IL-r phase is a process that develops laterally on distinct nuclei and not along the film normal. Furthermore, we found that the IL and the IL-r phase can be imaged by optical microscopy due to different optical reflection. Figure 13(b) shows optical micrographs of a single phase SLCO film (with IL crystal structure, top images) and of a double phase SLCO film (with IL and IL-r crystal structure, bottom images). Whereas on top of the single phase film only droplets are visible (black spots with a diameter of a few micrometers), the double phase film shows several gray regions with an average size of $\sim 30 \times 30\,\mu m^2$. As these regions were always correlated to signatures of the IL-r phase in XRD scans, we identify them as the IL-r phase. Furthermore, the micrographs verify the proposed lateral formation process of the IL-r phase, as deduced from XRD measurements. As illustrated in Fig. 13(a), the IL-r phase is semiconducting, which supports the findings of Zhou *et al.*[29] but contradicts the interpretation of Karimoto *et al.*[23,53] who suggest metallic behavior for the IL-r phase. As in our sample the IL-r and

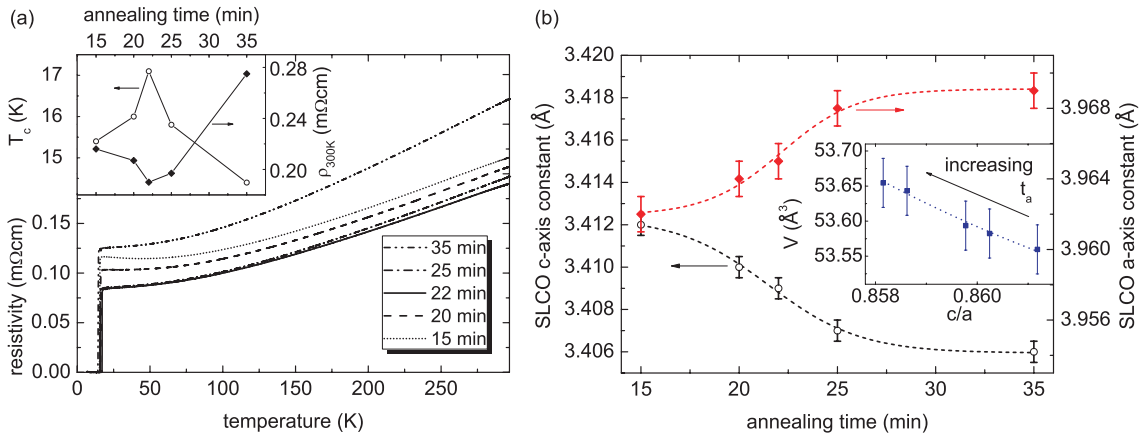

FIG. 12. (Color online) (a) Resistivity vs temperature of SLCO films deposited on BTO/STO with varying vacuum annealing time t_a. Inset shows the dependence of the transition temperature and of the room-temperature resistivity vs t_a. (b) Dependence of the lattice parameters a_{SLCO} and c_{SLCO} vs t_a. Inset shows the evolution of the unit cell volume $V = a_{SLCO}^2 \times c_{SLCO}$ with t_a. Lines are guides to the eyes.

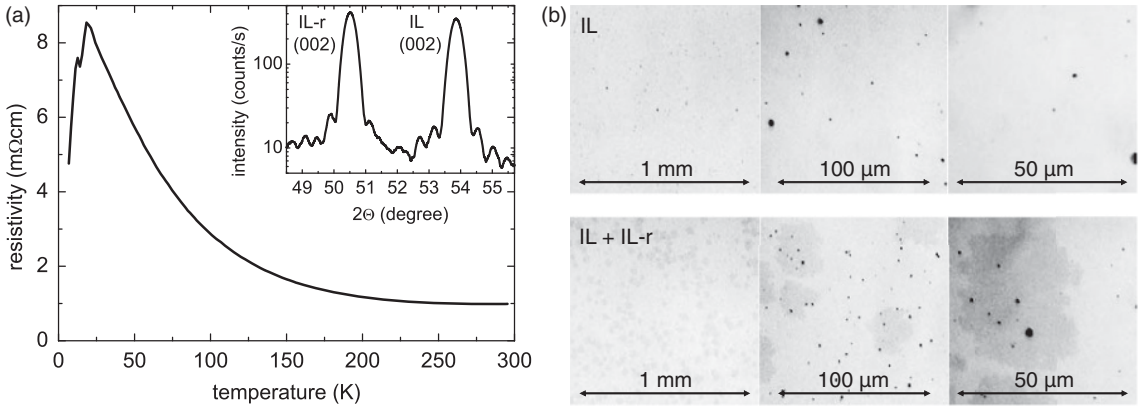

FIG. 13. (a) Resistivity vs temperature of SLCO on BTO/STO, exhibiting both IL and IL-r phase, as confirmed by XRD Θ-2Θ scans of the (002) region (cf. inset). (b) Optical micrographs of a single phase IL film (top) and of a film with both phases, IL and IL r (bottom). The regions with IL-r phase are visible as gray islands (cf. text), droplets are visible as black spots.

the IL phase coexist side by side, we can also observe the fingerprint of the latter as onset of superconductivity at $T \approx 18$ K. Yet, a full transition was not observed. With further reduction of the sample, the superconducting signature vanished completely, resulting in a dominantly IL-r phase thin film with more pronounced semiconducting/insulating transport properties (not shown here).

All results reported in Sec. IV C 1 concerning vacuum annealing of SLCO on BTO/STO could be verified qualitatively for SLCO on KTO, too. For simplicity, we will therefore only give a summary of the most important data and point out the main differences to SLCO on BTO/STO. A series with vacuum annealing time varying between 5 and 20 min showed, that T_c was highest ($T_c = 18.3$ K) when the room-temperature resistivity was lowest ($\rho_{300K} = 0.16$ mΩcm). However, we found a remarkable difference to SLCO on BTO/STO concerning the optimum annealing time. Whereas SLCO on BTO/STO had an optimum annealing time $t_a^{opt} = 22$ min, SLCO on KTO required an annealing time of $t_a^{opt} = 10$ min, which corresponds to the value reported by Karimoto *et al.*.[22,48] As discussed in Sec. III C, SLCO films on BTO/STO exhibit less tensile strain, as compared to the films grown on $KTaO_3$ substrates. Karimoto *et al.*[22] proposed that it is difficult to remove excess oxygen from compressively strained SLCO films. This is due to a reduced in-plane lattice constant a_{SLCO}, hindering the large O^{2-} ions to diffuse and desorb from the crystal. Regarding SLCO films on BTO/STO, this implies that longer annealing time is necessary to obtain a comparable degree of reduction as in the case of SLCO on KTO, conforming to our observation. We further want to note, that RHEED patterns of SLCO on BTO/STO exhibited intermediate streaks [cf. Fig. 3(a)], pointing to a superstructure, possibly due to excess oxygen, which would well support the above-mentioned interpretation.

For SLCO on KTO, the lattice constants and the unit cell volume showed the same monotonic behavior as found for SLCO on BTO/STO, i.e., with increasing vacuum annealing time, the a axis increased, the c axis decreased, and the unit cell volume V increased.

Finally, too long vacuum annealing of SLCO on KTO ended up in the formation of an IL-r phase, which showed semiconducting electric transport behavior and was visible in optical micrographs.

2. *Vacuum annealing temperature*

In this section, we analyze the influence of vacuum annealing temperature T_a on the properties of SLCO films. We prepared two sets of SLCO films on KTO that were annealed at $T_a = 550\,^{\circ}$C and $600\,^{\circ}$C, respectively. Figure 14(a) shows the $\rho(T)$ behavior of those films. Regarding $T_a = 550\,^{\circ}$C, it is obvious that an increase of t_a from 5 to 25 min leads to a decrease of $\rho(T)$, in accordance with the results presented in Sec. IV C 1, which was explained by removal of excess oxygen. However, to induce a superconducting transition, $t_a \gg 25$ min is required at this reduced annealing temperature. For comparison, two films annealed for $t_a = 5$ and 10 min at $T_a = 600\,^{\circ}$C are additionally plotted in Fig. 14(a). Already after $t_a = 5$ min vacuum annealing a superconducting transition with $T_c = 14.5$ K was observed, which reached its maximum value of $T_c = 17.5$ K after $t_a = 10$ min. In conclusion, removal of excess oxygen is strongly dependent on T_a, in accordance with literature.[22,27] For SLCO on BTO/STO, we observed the qualitatively same behavior (not shown here), yet with double vacuum annealing time necessary, as described in Sec. IV C 1.

Finally, we want to describe a combination of high- and low-temperature vacuum annealing as introduced by Li *et al.*[27] As found by XRD and electric transport measurements, some films still contained too much excess oxygen, although having been vacuum annealed at $T_a = 600\,^{\circ}$C. To remove the residual excess oxygen, those samples were additionally annealed in vacuum ($p_{vac} \lesssim 10^{-5}$ Pa) at $T_a \approx 340\,^{\circ}$C for $t_a = 40$ min. In most cases, the second low-temperature vacuum annealing step was sufficient to enhance or induce superconductivity, as shown in Fig. 14(b). This can be explained by the fact that excess oxygen only occupies weakly bond interstitial sites and can thus diffuse and desorb even at low T_a. Yet, it requires further examination whether *all* excess oxygen can be removed at low T_a or if a (previous) annealing step at high T_a is crucial. Furthermore, it was not essential if the low T_a annealing step was performed after the sample had been exposed to *ex situ*

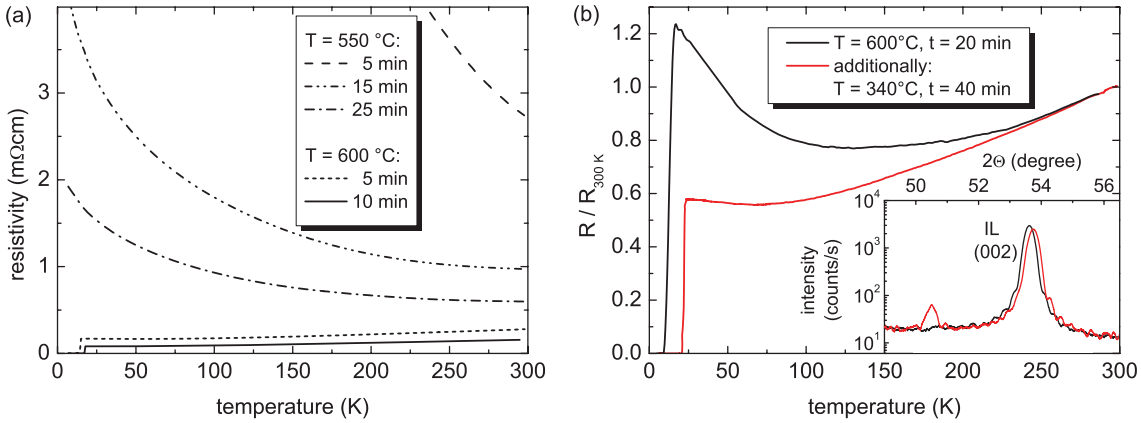

FIG. 14. (Color online) (a) Resistivity vs temperature for SLCO on KTO vacuum annealed under different conditions. The films of the first series were annealed at $T_a = 550\,^{\circ}$C for 5, 15, and 25 min, and the films of the second set were annealed at $T_a = 600\,^{\circ}$C for 5 and 10 min. (b) Normalized resistance vs temperature of an SLCO film on BTO/STO after 20 min vacuum annealing at $T_a = 600\,^{\circ}$C and after additional 40 min vacuum annealing at $T_a = 340\,^{\circ}$C. The inset shows XRD Θ-2Θ scans before and after the second annealing step, yielding a c-axis constants of 3.415 and 3.407 Å, respectively. A small contribution of the IL-r phase is visible at $2\Theta \approx 50.5\,^{\circ}$, after the additional vacuum annealing.

conditions or if it was performed *in situ* directly after high-T_a annealing; both methods lead to comparable results.

V. CONCLUSIONS

To summarize, we report in detail on the fabrication of single-crystalline thin films of the electron-doped infinite-layer superconductor $Sr_{1-x}La_xCuO_2$ (SLCO) by means of pulsed laser deposition and on their characterization by *in situ* and *ex situ* techniques. (001)-oriented $SrTiO_3$ (STO) and $KTaO_3$ (KTO) single crystals were used as substrates. Prior to deposition of SLCO on STO, a single-crystalline $BaTiO_3$ (BTO) thin film was deposited, acting as a buffer layer. In case of KTO, no buffer layers were deposited. The growth mode, the evolution of the in-plane lattice constant a, and the morphology of the BTO and SLCO films were monitored *in situ* by high-pressure reflection high-energy electron diffraction. We observed a Stranski-Krastanov growth mode, both for BTO and SLCO films and found that BTO films relaxed after growth of a few unit cells. Atomic force microscopy revealed very flat surfaces of BTO and SLCO with asperities in the range of a few unit cells. X-ray diffraction was used to determine the lattice constants of the films. Fringes and narrow rocking curves indicated high crystalline quality. A comparison of our thin film lattice constants a and c with literature bulk values showed that BTO buffer layers were (almost) relaxed, SLCO films on BTO-buffered STO (BTO/STO) moderately tensile strained, and SLCO films on KTO highly tensile strained. However, SLCO films on both kinds of substrates showed comparable electric transport properties. Furthermore, the stoichiometry of SLCO films on BTO/STO was determined by Rutherford backscattering spectroscopy. It revealed slight overdoping ($x \approx 0.15$) as compared to optimally doped SLCO polycrystals ($x = 0.10$). Moreover, we determined a critical current density of $j_c^{4.2\mathrm{K}} \approx 2 \times 10^6$ A/cm^2 and a maximum T_c of ~ 22 K $\approx \frac{1}{2} T_c^{\mathrm{bulk}}$. Finally, we discussed the influence of various process parameters on the thin film properties, such as varying excimer laser energy E_L, target-to-substrate distance d_{TS}, deposition pressure $p_{\mathrm{O_2}}$, vacuum annealing time t_a, and vacuum annealing temperature T_a and show that these parameters directly influence the oxygen content of the SLCO films and hence their electric transport properties.

ACKNOWLEDGMENTS

J.T. gratefully acknowledges support by the Evangelisches Studienwerk e.V. Villigst. V.L. acknowledges partial financial support by a grant of the Romanian National Authority for Scientific Research, CNCS UEFISCDI, project number PN-II-ID-PCE-2011-3-1065. The authors thank Marcel Kimmerle for technical assistance with RBS measurements. This work was funded by the Deutsche Forschungsgemeinschaft (project KL 930/11).

*leca@uni-tuebingen.de

[1] Y. Tokura, H. Takagi, and S. Uchida, Nature (London) **337**, 345 (1989).
[2] H. Takagi, S. Uchida, and Y. Tokura, Phys. Rev. Lett. **62**, 1197 (1989).
[3] T. Yamada, K. Kinoshita, and H. Shibata, Jpn. J. Appl. Phys. **33**, L168 (1994).
[4] M. Naito and M. Hepp, Jpn. J. Appl. Phys. **39**, L485 (2000).
[5] T. Siegrist, S. M. Zahurak, D. W. Murphy, and R. S. Roth, Nature (London) **334**, 231 (1988).
[6] M. G. Smith, A. Manthiram, J. Zhou, J. B. Goodenough, and J. T. Markert, Nature (London) **351**, 549 (1991).
[7] G. Er, Y. Miyamoto, F. Kanamaru, and S. Kikkawa, Physica C **181**, 206 (1991).

[8]G. Er, S. Kikkawa, F. Kanamaru, Y. Miyamoto, S. Tanaka, M. Sera, M. Sato, Z. Hiroi, M. Takano, and Y. Bando, Physica C **196**, 271 (1992).
[9]J. D. Jorgensen, P. G. Radaelli, D. G. Hinks, J. L. Wagner, S. Kikkawa, G. Er, and F. Kanamaru, Phys. Rev. B **47**, 14654 (1993).
[10]N. Ikeda, Z. Hiroi, M. Azuma, M. Takano, Y. Bando, and Y. Takeda, Physica C **210**, 367 (1993).
[11]C. C. Torardi, M. A. Subramanian, J. C. Calabrese, J. Gopalakrishnan, K. J. Morrissey, T. R. Askew, R. B. Flippen, U. Chowdhry, and A. W. Sleight, Science **240**, 631 (1988).
[12]H. Shaked, Y. Shimakawa, B. A. Hunter, R. L. Hitterman, J. D. Jorgensen, P. D. Han, and D. A. Payne, Phys. Rev. B **51**, 11784 (1995).
[13]X. Li, M. Kanai, T. Kawai, and S. Kawai, Jpn. J. Appl. Phys. **31**, L217 (1992).
[14]Y. Terashima, R. Sato, S. Takeno, S.-I. Nakamura, and T. Miura, Jpn. J. Appl. Phys. **32**, L48 (1993).
[15]C. Niu and C. M. Lieber, Appl. Phys. Lett. **61**, 1712 (1992).
[16]N. Sugii, M. Ichikawa, K. Kubo, T. Sakurai, K. Yamamoto, and H. Yamauchi, Physica C **196**, 129 (1992).
[17]N. Sugii, K. Matsuura, K. Kubo, K. Yamamoto, and M. Ichikawa, J. Appl. Phys. **74**, 4047 (1993).
[18]J. T. Markert, T. C. Messina, B. Dam, J. Huijbregste, J. H. Rector, and R. Griessen, Proc. SPIE **4058**, 141 (2000).
[19]J. T. Markert, T. C. Messina, B. Dam, J. Huijbregste, J. H. Rector, and R. Griessen, IEEE Trans. Appl. Supercond. **13**, 2684 (2003).
[20]V. Leca, D. H. A. Blank, G. Rijnders, S. Bals, and G. van Tendeloo, Appl. Phys. Lett. **89**, 092504 (2006).
[21]V. Leca, G. Visanescu, C. Back, R. Kleiner, and D. Koelle, Appl. Phys. A **93**, 779 (2008).
[22]S. Karimoto, K. Ueda, M. Naito, and T. Imai, Appl. Phys. Lett. **79**, 2767 (2001).
[23]S.-I. Karimoto and M. Naito, Appl. Phys. Lett. **84**, 2136 (2004).
[24]J. D. Jorgensen, P. G. Radaelli, H. Shaked, J. L. Wagner, B. A. Hunter, J. F. Mitchell, R. L. Hitterman, and D. G. Hinks, J. Supercond. **7**, 145 (1994).
[25]M. Naito, H. Sato, and H. Yamamoto, Physica C **293**, 36 (1997).
[26]H. Adachi, T. Satoh, Y. Ichikawa, K. Setsune, and K. Wasa, Physica C **196**, 14 (1992).
[27]Z. Z. Li, V. Jovanovic, H. Raffy, and S. Megtert, Physica C **469**, 73 (2009).
[28]S. Bals, G. V. Tendeloo, G. Rijnders, M. Huijben, V. Leca, and D. H. A. Blank, IEEE Trans. Appl. Supercond. **13**, 2834 (2003).
[29]X. Zhou, Y. Yao, J. Li, W. Xu, S. Jia, and Z. Zhao, Chin. Phys. Lett. **10**, 503 (1993).
[30]B. Mercey, A. Gupta, M. Hervieu, and B. Raveau, J. Solid State Chem. **116**, 300 (1995).
[31]V. Leca, Ph.D. thesis, University of Twente, Enschede, The Netherlands, 2003.
[32]Chemco GmbH, Germany.
[33]Crystal GmbH, Germany.
[34]CrysTec GmbH, Germany.
[35]Rosenau accelerator, Physikalisches Institut, Universität Tübingen, Germany.
[36]S. Diebold, Master' thesis, Universität Tübingen, Germany, 2010.
[37]*Handbook of Chemistry and Physics*, 52nd ed. (Chemical Rubber Company, USA, 1971).
[38]R. H. Dungan, D. F. Kane, and J. L. R. Bickford, J. Am. Cer. Soc. **35**, 318 (1952).
[39]J. Donohue, S. J. Miller, and R. F. Cline, Acta Cryst. **11**, 693 (1958).
[40]I. N. Stranski and L. Krastanov, Akad. Wiss. Lit. Mainz Math.-Natur. Kl. IIb **146**, 797 (1939).
[41]R. Werner, C. Raisch, V. Leca, V. Ion, S. Bals, G. VanTendeloo, T. Chassé, R. Kleiner, and D. Koelle, Phys. Rev. B **79**, 054416 (2009).
[42]B. E. Warren, *X-Ray Diffraction* (Addison-Wesley, Reading, MA, 1989).
[43]K. Terai, M. Lippmaa, P. Ahmet, T. Chikyow, T. Fujii, H. Koinuma, and M. Kawasaki, Appl. Phys. Lett. **80**, 4437 (2002).
[44]J. Tomaschko, C. Raisch, V. Leca, T. Chassé, R. Kleiner, and D. Koelle, Phys. Rev. B **84**, 064521 (2011).
[45]SIMNRA, Max-Planck-Institut für Plasmaphysik, Garching, Germany.
[46]T. Ito, K. Takenaka, and S. Uchida, Phys. Rev. Lett. **70**, 3995 (1993).
[47]T. Nishizaki, Y. Yamasaki, R. Tanaka, F. Ichikawa, T. Fukami, T. Aomine, S. Kubo, and M. Suzuki, Physica B **194-196**, 1877 (1994).
[48]S. Karimoto, K. Ueda, M. Naito, and T. Imai, Physica C **378–381**, 127 (2002).
[49]X. Gaojie, P. Qirong, Z. Zengming, and D. Zejun, J. Supercond. **14**, 509 (2001).
[50]D. Matsunaka, E. T. Rodulfo, and H. Kasai, Solid State Commun. **134**, 355 (2005).
[51]J. C. Nie, P. Badica, M. Hirai, A. Sundaresan, A. Crisan, H. Kitô, N. Terada, A. Iyo, Y. Tanaka, and H. Ihara, Supercond. Sci. Technol. **16**, L1 (2003).
[52]J. C. Nie, P. Badica, M. Hirai, Y. Kodama, A. Crisan, A. Sundaresan, Y. Tanaka, and H. Ihara, Physica C **388-389**, 441 (2003).
[53]S. Karimoto and M. Naito, Physica C **412-414**, 1349 (2004).

Publication II

Electric transport across $Sr_{1-x}La_xCuO_2$/Au/Nb planar tunnel junctions and x-ray photoelectron and Auger-electron spectroscopy on $Sr_{1-x}La_xCuO_2$ thin films

J. Tomaschko,[1] C. Raisch,[2] V. Leca,[1,3] T. Chassé,[2] R. Kleiner,[1] and D. Koelle[1,*]

[1]*Physikalisches Institut–Experimentalphysik II and Center for Collective Quantum Phenomena in LISA$^+$, Universität Tübingen, Auf der Morgenstelle 14, 72076 Tübingen, Germany*

[2]*Physikalische Chemie and LISA$^+$, Universität Tübingen, Auf der Morgenstelle 18, 72076 Tübingen, Germany*

[3]*Faculty of Applied Chemistry and Materials Science, University Politehnica of Bucharest, Gheorghe Polizu Street 1-7, Bucharest 011061, Romania*

(Received 10 March 2011; revised manuscript received 8 June 2011; published 24 August 2011)

Thin-film planar tunnel junctions with the electron-doped infinite-layer superconductor $Sr_{1-x}La_xCuO_2$ (SLCO) with $x \sim 0.15$ as bottom electrode, a thin Au interlayer, and Nb as top electrode were fabricated and characterized. Measurements of electric transport across these junctions provide information on the interface and surface properties of the SLCO thin films. No Cooper pair tunneling is observed; however, nonlinear current-voltage characteristics give evidence for quasiparticle (QP) tunneling across a thin insulating SLCO barrier at the SLCO/Au interface, with a single gap value ~1.4 meV, originating from superconducting Nb. The absence of a superconducting SLCO gap in the QP conductance curves indicates a thin normal-conducting SLCO layer below the insulating SLCO barrier. To examine its origin, x-ray photoelectron spectroscopy (XPS) and x-ray Auger-electron spectroscopy (XAES) on SLCO thin films were performed. We observe a Cu valence of +1 in the SLCO surface layer (within ~3 nm thickness) and of +2 in deeper regions, as expected for fully oxidized CuO_2 planes in the bulk. Hence, the XPS and XAES results for the SLCO films are consistent with the QP tunneling spectra observed for our planar SLCO/Au/Nb junctions.

DOI: 10.1103/PhysRevB.84.064521 PACS number(s): 74.72.Ek, 74.50.+r, 74.78.Fk, 82.80.Pv

I. INTRODUCTION

Both, hole- and electron-doped high-transition-temperature (T_c) cuprate superconductors have been synthesized and investigated intensively throughout the past two decades. On the electron-doped side only two families of cuprate compounds are known. These are the T' compounds[1,2] $L_{2-x}Ce_xCuO_4$ (L = La,Pr,Nd,Sm,Eu) with maximum T_c = 30 K and the infinite-layer (IL) compounds[3,4] $Sr_{1-x}L_xCuO_2$ (L = La,Pr,Nd,Sm,Gd) with maximum T_c = 43 K. The IL crystal structure is formed by alternating stacks of CuO_2 and $Sr_{1-x}(L_x)$ (a-b) planes along the c-axis direction. The charge reservoir block, commonly present in cuprate superconductors, as well as apical oxygen do not exist in the ideal IL crystal lattice.[5] Electron doping is suggested because the nominal Sr and L valences are +2 and +3, respectively.[4] As the crystal structure of the IL compounds is the simplest of all cuprate superconductors, they provide a unique opportunity to explore the fundamental nature of high-T_c superconductivity. For the same reason, they are often referred to as the "parental structure" of cuprate superconductors.[6] However, due to severe difficulties in the synthesis of high-quality samples, the IL cuprates have been much less examined than any other cuprate superconductors. In particular, no large single crystals of the IL compounds have been synthesized so far, and the synthesis of polycrystalline bulk material requires high pressure (≈1 GPa).[7–9] To overcome this problem, epitaxially grown, single-crystal IL thin films have been fabricated, where the pressure is supplied by epitaxial strain.[10,11] Karimoto *et al.*[12] succeeded in synthesizing electron-doped IL thin films with T_c close to the bulk value by molecular beam epitaxy (MBE) on $KTaO_3$ (KTO) substrates, supplying tensile strain, which is believed to support the electron-doping effect for the CuO_2 planes. Moreover, they confirmed that, under the oxidizing conditions generally used during deposition, vacuum annealing of the as-grown film is essential for superconductivity to emerge. Without this reduction step, excess oxygen occupies interstitial sites in the Sr(L) planes and localizes electrons, which in turn hampers superconductivity. This reduction step was established in T' compounds before[13] and is nowadays a common synthesis step for IL thin films grown by various techniques, such as sputtering,[11,14] pulsed laser deposition (PLD)[15,16] and MBE.[12,17] Yet, too strong reduction ends up in the formation of ordered oxygen vacancies in the CuO_2 planes. This phase is called the "long-c-axis" phase or the "infinite-layer-related" (IL-r) phase,[15,18] which suppresses superconductivity.[12,14] The unit cell of the IL-r phase is a superstructure of the IL unit cell with lattice parameters $2\sqrt{2}a_p \times 2\sqrt{2}a_p \times c_s$, where a_p is the in-plane parameter of the perovskite-type IL structure with tetragonal symmetry and c_s is the superstructure-extended c-axis parameter with $c_s \approx 3.6$ Å (compared to $c \approx 3.4$ Å for the IL structure).

To examine the influence of vacuum annealing on the surface of our PLD-grown $Sr_{1-x}La_xCuO_2$ (SLCO) thin films, we performed surface-sensitive electric transport measurements, x-ray photoelectron spectroscopy (XPS) and x-ray Auger-electron spectroscopy (XAES). Our transport measurements were carried out on planar SLCO/Au/Nb tunnel junctions. Quasiparticle tunneling was observed, which we attribute to an insulating barrier at the SLCO/Au interface and a thin normal-conducting SLCO layer below this barrier. To identify its origin, XPS studies on SLCO thin films were performed, revealing a reduced Cu species with valence +1 in the surface layer (~3 nm thick) of SLCO. This result is consistent with the findings of other groups[19–21] who performed corresponding studies on CuO and Cu_2O samples.

Moreover, to our knowledge, we performed the first XPS and XAES studies on the (insulating) IL-r phase, allowing us to pinpoint the spectral lines of the superconducting IL phase by comparing the spectra with each other. Furthermore, x-ray diffraction studies indicate the presence of an approximately 3-nm-thick disordered SLCO surface layer, supporting our planar tunneling, XPS, and XAES results.

II. SAMPLE FABRICATION AND EXPERIMENTAL DETAILS

A polycrystalline $Sr_{1-x}La_xCuO_2$ ($x = 0.125$) target[22] was used for epitaxial growth of 25- to 30-nm-thick SLCO films on (001) KTO substrates[23] at 580 °C and 20 Pa oxygen pressure, by pulsed laser deposition, using a KrF ($\lambda = 248$ nm) excimer laser with a repetition rate of 2 Hz. The base pressure of the PLD chamber was 10^{-6} Pa. *In situ* high-pressure reflection high-energy electron diffraction (RHEED) was used to monitor the growth mode and growth rate by counting the number of deposited monolayers within the first 5 to 30 unit cells. In order to remove excess oxygen from the Sr/La planes, after thin-film deposition the samples were annealed in vacuum (10^{-5} Pa) at 580 °C for 5–10 min before cooling down to room temperature.

For the fabrication of planar tunnel junctions, the samples were transferred in vacuum ("*in situ*") to an electron beam evaporation chamber, where a 5-nm-thick Au layer was evaporated on top of SLCO. The Au thickness was sufficient to cover all asperities of the underlying SLCO layer; atomic force microscopy in contact mode on SLCO thin-film reference samples revealed a root mean square roughness of 0.3 to 0.7 nm. Subsequently, the samples were transferred *in situ* to a magnetron sputtering chamber where a 21-nm-thick Nb film was sputtered on top of the Au layer. The SLCO/Au/Nb trilayers were removed from the deposition system and patterned to form planar SLCO/Au/Nb junctions with lateral dimensions of $5 \times 30\ \mu m^2$ by standard photolithography and Ar ion milling. This involved sputtering of an additional 5-nm-thick Au layer and subsequently a 100-nm-thick Nb layer, which was etched down to 75 nm thickness later on during the patterning process (see Fig. 1). For a detailed description of the fabrication process see Ref. 24. Altogether, we fabricated two chips, each of which had five SLCO/Au/Nb junctions with nominally identical geometry. Electric transport properties were measured in the temperature range $T =$ (4.2–300) K in a magnetically and radio frequency shielded setup using feed lines with high-frequency-noise filters.

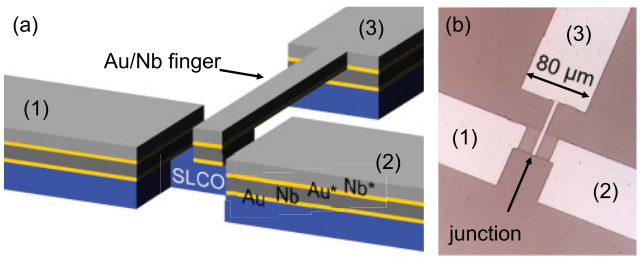

FIG. 1. (Color online) Schematic layout (a) and micrograph (b) of planar SLCO/Au/Nb junction. The stacking sequence from bottom to top is SLCO (26 nm)/Au (5 nm)/Nb (21 nm)/Au* (5 nm)/Nb* (75 nm). The first three layers forming the junction were deposited *in situ*. The uppermost two layers (labeled with *) are required for the patterning process (Ref. 24).

In order to obtain element-specific information regarding the chemical state (valence) of SLCO, XPS and XAES were performed. For these studies, two SLCO thin films—SLCO-1 and SLCO-2—were grown under the same conditions, with the same thickness, as described above and transferred to the XPS/XAES setup immediately after growth to minimize surface contamination. The system (base pressure 5×10^{-8} Pa) consists of a SPECS XR 50 Mg $K\alpha$ x-ray source and a SPECS Phoibos 100 hemispherical energy analyzer. The pass energy was set to 20 eV for all experiments, yielding an energy resolution of ≈1 eV. By tilting the sample about an angle θ, the information depth could be further reduced by a factor of $\cos\theta$. In our experiments the samples were measured at $\theta = 0°$ (normal incidence) and $\theta = 60°$ (grazing incidence), corresponding to an information depth of ≈6 and ≈3 nm, respectively. The samples could be heated in the XPS/XAES setup to examine the effect of vacuum annealing. After initial XPS analysis, sample SLCO-1 was annealed at low temperature ($T \approx 350$ °C, $t = 30$ min) and sample SLCO-2 at high temperature ($T \approx 550$ °C, $t = 5$ min) and then measured again. For data obtained after annealing in the XPS/XAES setup we refer to these samples as SLCO-1a and SLCO-2a. After XPS analysis, the crystal structures of the SLCO thin films were characterized by x-ray diffraction (XRD) using a Panalytical X'Pert system equipped with a Cu cathode and monochromator.

III. ELECTRIC TRANSPORT PROPERTIES

In this section we present and discuss results obtained on the electric transport properties of one of the planar SLCO/Au/Nb junctions. A second junction on the same chip and two other junctions on the second chip showed very similar behavior.

A. Technical aspects

For electric transport measurements, the sample was contacted in a two-point arrangement, with bias current I flowing from pad 1 along the SLCO layer, through the SLCO/Au/Nb junction and the Au/Nb finger to pad 3 (see Fig. 1); the voltage V was detected across the same two pads. For T below the Nb transition temperature $T_{c,Nb}$, the Au layers are expected to become superconducting due to the proximity effect. In this case, we have a four-point arrangement. Electrodes 1 and 2 were used for characterization of the 39-μm-long and 30-μm-wide bottom SLCO layer (see Fig. 1).

To sort out parasitic signals from the upper Au layer, we checked the above-mentioned proximity effect by fabricating a reference Nb/Au/Nb junction, which had the same geometry as the SLCO/Au/Nb junction. The fabrication process for this reference sample was nominally identical to the process for the upper Nb-Au-Nb layers in the SLCO/Au/Nb/Au/Nb samples, i.e., the Au layer and the upper Nb layer were deposited after exposing the bottom Nb layer to *ex situ* conditions. Below $T_{c,Nb}$, the reference sample showed no voltage drop up to the critical current $I_{c,Nb}$ of the Au/Nb finger. Thus, for $T < T_{c,Nb}$ and $I < I_{c,Nb}$, any voltage signal detected

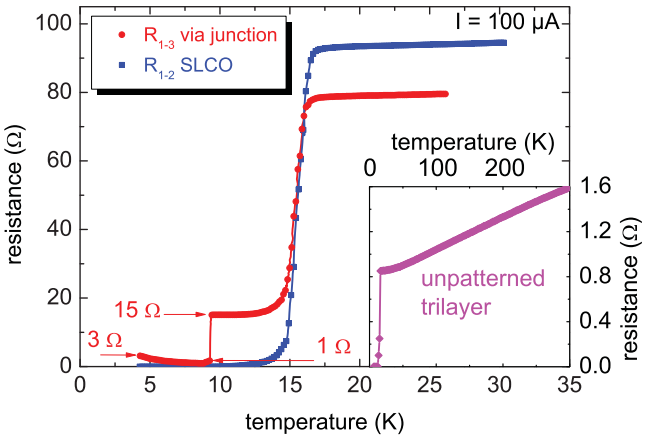

FIG. 2. (Color online) Resistance R vs temperature T measured across the SLCO/Au/Nb junction ($R_{1\text{-}3}$) and along the SLCO bottom layer ($R_{1\text{-}2}$). Inset: $R(T)$ of the unpatterned SLCO/Au/Nb trilayer.

for the SLCO/Au/Nb/Au/Nb samples must stem from the SLCO/Au/Nb junction.

B. Resistance vs temperature

Figure 2 shows measurements of the resistance $R_{1\text{-}3}$ [from (1) to (3)] and of the resistance $R_{1\text{-}2}$ [from (1) to (2)] vs temperature T. For $R_{1\text{-}3}$ (across the SLCO/Au/Nb junction), two resistive transitions are visible, which we attribute to the transitions of SLCO ($T_{c,\mathrm{SLCO}} = 15.5$ K) and Nb ($T_{c,\mathrm{Nb}} = 8.7$ K) with transition widths $\Delta T_{c,\mathrm{SLCO}} \approx 2$ K and $\Delta T_{c,\mathrm{Nb}} \approx 0.1$ K, respectively. From Rutherford backscattering spectroscopy we determined a doping of $x \sim 0.15$, which is slightly above the doping of our target.[25] Hence, our films are overdoped, which explains the reduced T_c as compared to optimally doped SLCO with $x \sim 0.10$.[4,12] The residual resistance below $T_{c,\mathrm{Nb}}$ has to be assigned to the SLCO/Au/Nb junction (cf. Sec. III A), which will be discussed in Sec. III C.

The $R_{1\text{-}2}(T)$ curve for the bottom SLCO layer yields a $T_{c,\mathrm{SLCO}}$ which coincides with the SLCO transition measured across the junction, as expected. The inset of Fig. 2 shows $R(T)$ of the unpatterned SLCO/Au/Nb trilayer from the same chip measured prior to junction pattering in a van der Pauw geometry. The resistive transition occurs at 15.5 K, which demonstrates that $T_{c,\mathrm{SLCO}}$ is not affected by the junction patterning process.

For the resistance measurement on the unpatterned trilayer, we expect the normal-state resistance to be dominated by the Au/Nb layer with much lower resistivity as compared to the SLCO layer. Neglecting the contribution from the thin Au layer gives a lower bound for the normal-state resistivity of the Nb film in the trilayer of $\rho_{n,\mathrm{Nb}} \approx 8\ \mu\Omega$ cm. This value is slightly larger than typical $\rho_{n,\mathrm{Nb}}$ values for our Nb thin films; however, this is consistent with the relatively small residual resistance ratio of 2 as determined from the inset shown in Fig. 2.

From the Au/Nb normal-state resistivity as determined above, we can estimate the normal-resistance contribution $R_{n,\mathrm{Au/Nb}}$ of the Au/Nb finger (75 μm long and 5 μm wide) connecting the SLCO/Au/Nb junction with pad 3 (see Fig. 1). This yields $R_{n,\mathrm{Au/Nb}} = 15\ \Omega$, which is in very good agreement with the residual resistance $R_{1\text{-}3}$ measured across the patterned junction in the range $T_{c,\mathrm{Nb}} < T < T_{c,\mathrm{SLCO}}$ (see Fig. 2).

Finally, comparing the values $R_{n,1\text{-}3} = 79\ \Omega$ and $R_{n,1\text{-}2} = 93\ \Omega$ of the normal resistance R_n slightly above $T_{c,\mathrm{SLCO}}$, we find $R_{n,\mathrm{SLCO}} = 58\ \Omega$ for the normal resistance of the bottom SLCO film between pads 1 and 2 and normal-resistance values for the three pads $R_{n,i} = 17.5\ \Omega$ ($i = 1,2,3$), if we assume that they are identical and if we take into account that $R_{n,\mathrm{SLCO}}/2$ will contribute in series with $R_{n,\mathrm{Au/Nb}}$ to $R_{n,1\text{-}3}$. From $R_{n,\mathrm{SLCO}}$ we calculate a normal-state resistivity of the SLCO film $\rho_{n,\mathrm{SLCO}} = 0.12$ mΩ cm, which is within the range of typical values 0.1 to 0.2 mΩ cm for our SLCO films; i.e., the patterning process seems not to severely affect $\rho_{n,\mathrm{SLCO}}$.

C. Current-voltage characteristics

Figure 3(a) shows (current-biased) $I(V)$ characteristics of the SLCO/Au/Nb junction, in the temperature range $4.2 \leqslant T \leqslant 8.9$ K. Two main transitions are visible, the first to $R_{1\text{-}3} = 15\ \Omega$ and the second to $R_{1\text{-}3} = 44\ \Omega$. According to the above discussion of the $R(T)$ curves in Fig. 2, the first transition can be identified as the switching of the Au/Nb finger to the normal state and the second transition to the switching of the SLCO film between pads 1 and 3 to the normal state (with resistance $R_{n,\mathrm{SLCO}}/2 = 29\ \Omega$), which is also consistent with the observation that the second transition persists to temperatures above 8.7 K, i.e., it has to be attributed to SLCO.

In Fig. 3(b), the low-voltage behavior of the $I(V)$ curves is displayed. Two main features are obvious: (i) Cooper pair tunneling is not observed, and (ii) the $I(V)$ curves are nonlinear, possibly due to the presence of an insulating tunneling barrier. This explains the residual resistance below 8.7 K as observed in the $R_{1\text{-}3}(T)$ curve shown in Fig. 2. Both points will be discussed in the following.

1. *Absence of Cooper pair tunneling*

If the barrier between superconducting Nb and SLCO was (electrically) too thick, no Cooper pair tunneling could be observed. However, a too thick Au interlayer between Nb and SLCO can be ruled out because of the previously described proximity effect. Instead, a plausible explanation might be based on the formation of an oxygen gradient along the c axis of the SLCO film. As described in Sec. II, a reduction step right after SLCO film growth is necessary to obtain superconducting properties. This reduction step possibly generates a gradient, with decreasing oxygen concentration toward the SLCO surface. As shown elsewhere,[25] an oxygen-deficient phase has normal conducting or even insulating electric properties. Such an insulating SLCO surface could act as a tunneling barrier.

2. *Nonlinear tunneling curves*

By numerical differentiation, the low-voltage regime of the $I(V)$ curves was transformed into differential conductance $dI/dV(V)$ curves, which are shown in Fig. 3(c). A superconducting gap $\Delta \approx 1.4$ meV is visible, which can be assigned to Nb. The presence of the Nb gap is a clear indication for *quasiparticle* tunneling from the superconducting Au/Nb electrode through a tunneling barrier, which is formed near

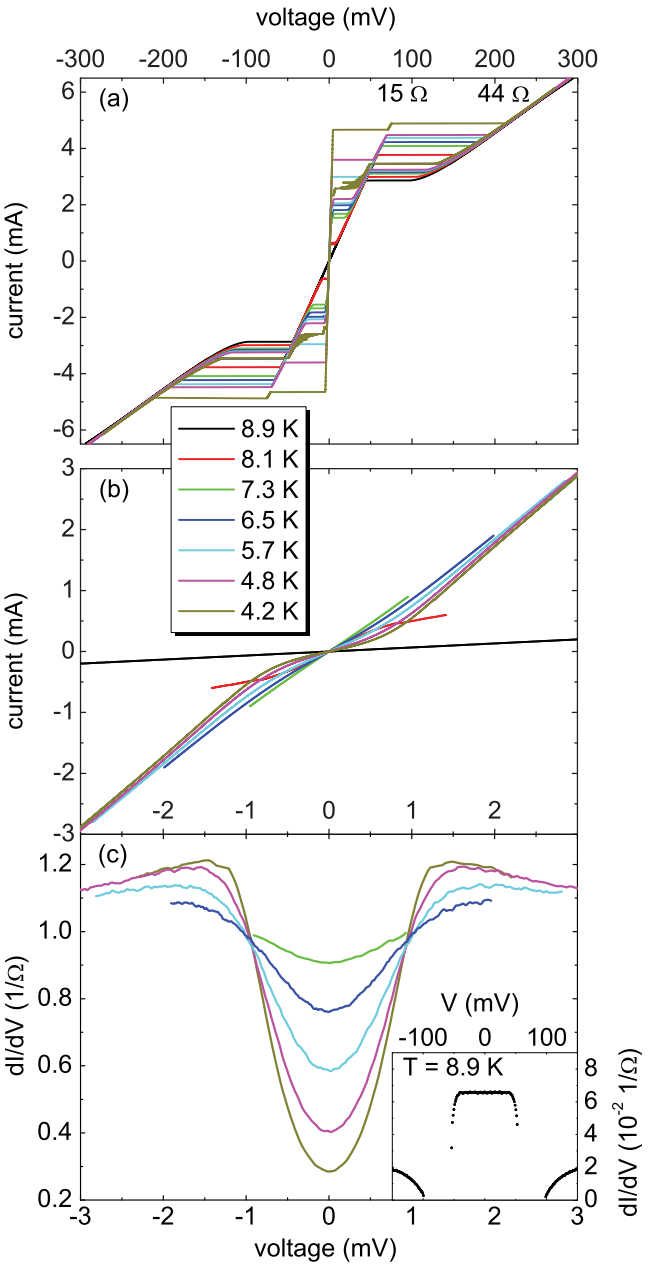

FIG. 3. (Color online) Transport characteristics of a planar SLCO/Au/Nb junction for different temperatures: (a) $I(V)$ curves over large voltage range $|V| \leqslant 300$ mV and (b) zoom-in of low-voltage regime $|V| \leqslant 3$ mV. (c) Differential conductance curves $dI/dV(V)$. Inset shows $dI/dV(V)$ at $T = 8.9$ K on a larger voltage scale.

the SLCO/Au interface, into *normal-conducting* SLCO. We did not find any indication for the presence of an SLCO gap in the $dI/dV(V)$ curves for $T < T_{c,\mathrm{Nb}}$. Furthermore, the inset of Fig. 3(c) shows the $dI/dV(V)$ curve at $T = 8.9\ \mathrm{K} > T_{c,\mathrm{Nb}}$ with a constant conductance and no gaplike feature up to $|V| = 53$ mV. Thus, we have to conclude that there is no tunneling from superconducting SLCO across the barrier. Our data suggest a "stacking" of superconducting SLCO/normal-conducting SLCO/insulating SLCO (tunneling barrier)/superconducting Au/Nb along the sample normal.

IV. X-RAY PHOTOELECTRON SPECTROSCOPY

To examine the chemical state of the SLCO surface, XPS and XAES were performed on the two SLCO thin-film reference samples (SLCO-1 and SLCO-2), which were transferred to the XPS/XAES setup immediately after growth. For data taken after annealing in the XPS/XAES setup we refer to those samples as SLCO-1a and SLCO-2a. The adventitious carbon 1*s* line was used to calibrate the binding-energy scale, assuming a binding energy of 284.6 eV for hydrocarbons. For all XPS data shown below, the peak centers, Gaussian widths, and intensity ratios were determined by numerical fits.[26] For better clarity we do not show the fitting curves in the graphs below. Instead, all fitting results are summarized in Table I.

A. XPS of the infinite-layer phase

Figure 4 shows XP spectra of the O 1*s* (a), the Sr 3*d* (b), and the Cu 2*p* (c) orbitals, for both normal (0°) and grazing (60°)

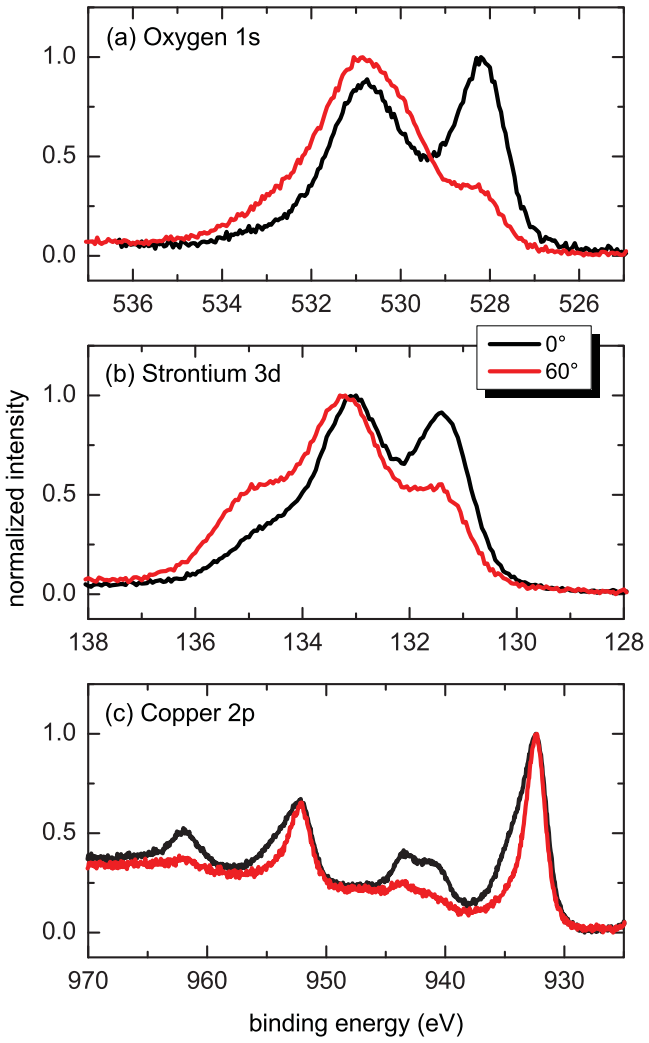

FIG. 4. (Color online) XPS data from SLCO-1 (with IL crystal structure) showing relevant photoemission signals for O 1*s* (a), Sr 3*d* (b), and Cu 2*p* (c) lines at normal incidence 0° and tilt angle 60°, corresponding to information depths of 6 and 3 nm, respectively.

TABLE I. Core-level binding energies (eV) as determined by numerical fitting of the XPS data. The two components (see text) are labeled as 1 and 2, respectively. The Gaussian peak width is denoted in parentheses. The intensity ratio I_1/I_2 is determined by the ratio of the areas beneath the according peaks. For Sr, ΔE denotes the splitting of the doublet ($j = 3/2$ and $5/2$). The superconducting IL bulk component is marked with an asterisk (∗) and the insulating IL-r bulk component with a dagger (†) (see text). All unmarked components are surface components.

		Cu $2p_{3/2}$			Sr $3d_{5/2}$					O $1s$		
Sample		1	2	I_1/I_2	1	ΔE	2	ΔE	I_1/I_2	1	2	I_1/I_2
SLCO-1	(0°)	932.3(1.6)	934.3(1.5)*	3.5	131.3(1.0)*	1.8	132.7(1.8)	1.7	1.3	528.2(1.1)*	530.7(1.4)	0.6
	(60°)	932.4(1.3)	934.1(1.7)*	8.6	131.4(1.2)*	2.0	133.0(1.4)	1.9	0.5	528.2(0.8)*	530.7(2.8)	0.1
SLCO-2a	(0°)	932.4(1.6)†	933.8(1.5)†	0.8	131.8(1.0)†	1.8	132.8(1.4)	1.8	0.5	528.6(1.0)†		
	(60°)	932.4(1.6)†	934.0(2.0)†	1.4	131.9(1.1)†	1.9	133.0(1.4)	1.8	0.3	528.9(1.5)†	530.5(0.8)	1.3

incidence. The data were collected on the superconducting thin film SLCO-1, which had a single-phase IL crystal structure even after annealing in the XPS/XAES setup, as confirmed by subsequent XRD measurements (see Sec. VI).

1. Oxygen 1s

In Fig. 4(a) two components can be identified in the spectrum. By tilting the sample to 60°, the high-energy peak increased whereas the low-energy one decreased. Thus, the first one is identified as a surface component and the second one as a bulk component.

Vasquez *et al.*[27] showed that the peak at rather low binding energy of 528.2 eV belongs to oxygen in the CuO_2 planes of common electron-doped cuprate superconductors, where copper has a valence of +2. The surface component at 530.7 eV is a mixture of adsorbed oxygen-containing species, mostly water, and compounds like $Sr(OH)_2$ and $SrCO_3$, which may have formed when the sample was in contact with ambient air. Also, surface species of the CuO_2 planes (which are not charge neutral due to the reduced symmetry in the uppermost layer) could contribute to the high-energy peak. We found that this peak drastically decreased upon heating the sample to around (300–350) °C (not shown here), hinting at water contamination because all other compounds are not volatile under the prevailing conditions. However, the high-energy peak did not disappear completely after annealing, supporting the fact that other surface compounds are present.

2. Strontium 3d

Due to spin-orbit coupling, the strontium $3d$ orbital is split into a doublet with $j = 3/2$ and 5/2. The XPS data shown in Fig. 4(b) reveal a superposition of two doublets. The two peaks within each doublet show a separation of (1.8 ± 0.1) eV and an intensity ratio of 3:2, as expected. For the high- and the low-binding-energy doublets, the $j = 5/2$ line is located at 132.7 and 131.3 eV, respectively. Under grazing incidence, the high-binding-energy doublet gains intensity at the expense of the low-binding-energy doublet. Thus, the first one is identified as a surface component and the second one as a bulk component.

According to Vasquez *et al.*,[27] the bulk doublet originates from the superconducting SLCO phase and the surface doublet from a carbonate ($SrCO_3$). Nevertheless, a hydroxide such as $Sr(OH)_2$ and an oxide such as SrO are also candidates for this surface component. In other studies[28–31] the Sr $3d_{5/2}$ peak for the hole-doped cuprate superconductor $Bi_2Sr_2CaCu_2O_8$ was found at a binding energy of (132.3 ± 0.5) eV, which is close to our result. Compared to the binding energy of elemental Sr at 134.2 eV or of bulk SrO at 135.1 eV,[32] the binding energy found in cuprate superconductors is quite low. This shift toward lower binding energy, as compared to the corresponding metal or simple oxide, is a common feature of various elements in cuprate superconductors.[29] It is the environment and the electronic correlation in these complex materials that lead to this shift.

Upon annealing the sample at (300–350) °C, the half-width of the surface peak increased, but no substantial change in the strontium spectra was observed (not shown here). As mentioned above, Sr-containing contaminations are not volatile under these conditions. The broadening is usually attributed to effects such as charging or nonstoichiometry.

3. Copper 2p

From the Cu $2p$ core-level spectra, the oxidation state of copper can be derived, as found by XPS studies on Cu, Cu_2O, and CuO samples[19,20] as well as on complex high-temperature superconductors like Bi-Sr-Ca-Cu-O (Refs. 28,33) and Y-Ba-Cu-O.[34] In fact, the main lines are known to stem from the screened Cu $2p^5 3d^{10}\underline{L}$ final state of Cu^{2+}, where $\underline{L}$ stands for a hole on the ligand oxygen, and from the screened Cu $2p^5 3d^{10}$ final state of Cu^{1+}, whereas the satellites are known to stem from the unscreened Cu $2p^5 3d^9$ final state of Cu^{2+}. In the latter case, the d shell is not full and the satellite line shape is governed by multiplet splitting, resulting in a broad peak structure.[34,35] The absence of the satellite is thus a fast and reliable sign that there are no Cu^{2+} ions in the compound. Note that the center position of the Cu $2p^{3/2}$ main line is only weakly dependent on the oxidation state of copper: As Tobin *et al.*[36] have shown, the $2p_{3/2}$ peaks of Cu, Cu_2O, and CuO are centered at 932.6, 932.4, and 933.6 eV, corresponding to Cu^0, Cu^{1+}, and Cu^{2+} valences, respectively. This allows us to distinguish Cu^{2+} from a reduced species, Cu^{1+} or Cu^0, but not to distinguish Cu^{1+} from Cu^0. For that purpose, we refer to the Auger-emission studies presented in Sec. V.

The Cu $2p$ spectrum of our sample shown in Fig. 4(c) has a doublet with main lines at 932.3 eV (Cu $2p_{3/2}$) and 952.2 eV (Cu $2p_{1/2}$). A closer look reveals a shoulder on the high-binding-energy side of these lines, indicating the presence of a second copper species. The lines of this species are situated at 934.3 and 954.2 eV. Moreover, satellites at

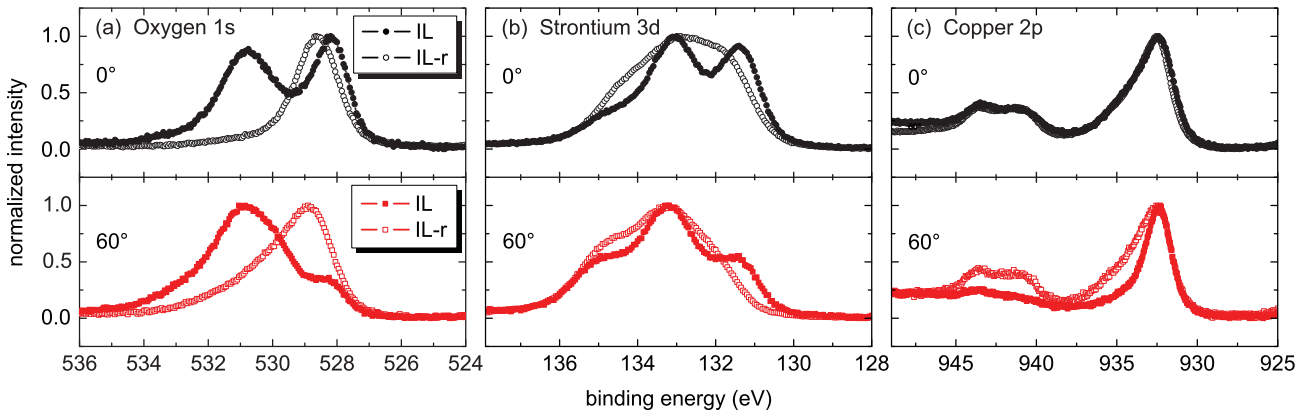

FIG. 5. (Color online) Comparison of XP spectra of the superconducting IL (full symbols) and the insulating IL-r sample (open symbols). Upper graphs show normal (0°) and lower graphs grazing incidence (60°) for O 1*s* (a), Sr 3*d* (b), and Cu 2*p* (c). The clear differences between the spectra allow us to exactly identify the superconducting phase as well as surface contaminations.

around 942 and 962 eV are visible. Tilting our sample, i.e., decreasing the information depth, leads to the disappearance of the satellites and the high-energy doublet. Accordingly, the surface component is identified as a (strongly) reduced copper species with Cu^{1+} or Cu^{0} valence, whereas the bulk component is clearly identified as the oxidized phase with Cu^{2+} valence, which is expected for CuO_2 planes in common cuprate superconductors. Note, that electric transport measurements on our SLCO thin films[25] showed that excessive vacuum annealing of a previously superconducting film leads to loss of superconductivity. This allows us to interpret the oxidized bulk phase as the superconducting phase and the reduced surface phase as a normal-conducting phase. This is an important result because it goes hand in hand with the results of the planar tunneling measurements described in Sec. III C.

In addition to SLCO-1 and SLCO-2, we investigated another sample (not shown here), called SLCO-3, which was not vacuum annealed right after deposition. Instead, it was immediately cooled down *in situ* (while the pressure was reduced to 10^{-5} Pa) to room temperature and was hence less reduced as compared to SLCO-1. This was confirmed by means of XPS: Under normal incidence, both the satellites and the main lines characteristic for Cu^{2+} were more strongly developed in SLCO-3 as compared to SLCO-1. Furthermore, after annealing SLCO-1 at (300–350) °C in the XPS chamber, the Cu^{2+} species decreased slightly (not shown here). Thus, comparing the Cu 2*p* XP spectra of SLCO-1, SLCO-1a, and SLCO-3, we find that the Cu^{2+} lines decreased with increasing annealing time, i.e., we clearly see the effect of vacuum annealing on the Cu valence.

B. XPS of the infinite-layer-related phase

Sample SLCO-2a was vacuum annealed in the XPS/XAES setup at 550 °C for 5 min. During this procedure, a substantial secondary phase emerged, as shown in Sec. VI by means of XRD. This oxygen-deficient phase is called the long-*c*-axis phase or infinite-layer-related phase. It is characterized by ordered oxygen vacancies.[15,18] As shown elsewhere,[25] the IL-r phase is electrically insulating and not superconducting.

For simplicity, in the following the sample SLCO-1 is referred to as "IL" (because of its single-phase IL crystal structure) and the annealed sample SLCO-2a is referred to as "IL-r" (because of its dominant IL-r crystal structure). The XP spectra of the IL-r phase differ strongly from those of the IL phase. For comparison, both spectra are shown in Fig. 5. Additionally, the relevant XPS data of the IL-r phase are summarized in Table I, labeled as SLCO-2a, allowing a direct comparison with the XPS data of the IL phase, labeled as SLCO-1.

1. *Oxygen 1s*

The IL-r spectra in Fig. 5(a) exhibit two components, a weak surface component at high binding energy (530.5 eV) and a strong bulk component at low binding energy (528.8 ± 0.2 eV). The bulk peak of the IL phase at 528.2 eV is absent in the IL-r spectra. Note that superconductivity is also absent in the IL-r phase. Thus, we can definitely assign the peak at 528.2 eV to the superconducting phase, confirming the discussion of Sec. IV A. The IL-r surface component at 530.5 eV was also present on the surface of the IL sample. As discussed before, this component can possibly be identified as $SrCO_3$ or $Sr(OH)_2$. However, as the spectral weight of this surface component decreased strongly upon vacuum annealing at 550 °C, some of the adsorbates must have been evaporated. At these elevated temperatures, water may no longer be found and also $Sr(OH)_2$ should have desorbed.

2. *Strontium 3d*

As for oxygen, the Sr spectra of the IL-r phase differ strongly from those of the IL phase, as shown in Fig. 5(b). The IL-r spectra exhibit two doublets, i.e., two components, with the high-energy one at $E_{5/2} = (132.9 \pm 0.1)$ eV on the surface and the low-energy one at $E_{5/2} = (131.9 \pm 0.1)$ eV in the bulk. The two peaks (for $j = 5/2$ and $j = 3/2$) within each doublet are separated by (1.8 ± 0.1) eV. The bulk doublet of superconducting IL at $E_{5/2} = (131.4 \pm 0.1)$ eV is absent in the spectra of the nonsuperconducting IL-r phase. Thus, we can pinpoint this doublet to the superconducting phase, confirming the discussion of Sec. IV A. Instead, the bulk component of the IL-r phase shows a positive chemical shift of +0.5 eV compared to SLCO. This result is consistent with the findings of Nagoshi *et al.*[37] They showed that the core-level energies of

$Bi_2Sr_2CaCu_2O_8$, $YBa_2Cu_3O_7$, and related cuprates are lower in the superconducting and higher in the normal-conducting phase. They attribute this to a different Madelung potential due to changes in bond length with varying charge carrier concentrations in the copper oxide planes. Moreover, the absolute binding energies are comparable to our results, both for superconducting and for normal-conducting samples. Finally, the IL-r surface doublet was also present in the IL surface phase. As discussed before, this component can possibly be ascribed to $SrCO_3$ or $Sr(OH)_2$, i.e., to surface adsorbates.

3. *Copper 2p*

Figure 5(c) shows that the 0° *and* 60° spectra of the IL-r phase are very similar to the 0° spectrum of the IL phase. As discussed in Sec. IV A, the 0° spectrum of the IL phase shows two components, an oxidized bulk component with Cu^{2+} valence and a reduced surface component with Cu^{1+} or Cu^0 valence. As the IL-r spectrum does not show a pronounced dependence on the information depth, we can conclude that Cu of different valences is distributed throughout the *entire* IL-r sample and none of them is restricted to the surface, in contrast to the IL sample.

To identify the valence of the reduced species, either Cu^{1+} or Cu^0, we performed x-ray Auger-electron spectroscopy. The results for both samples, IL and IL-r, are presented in Sec. V.

V. X-RAY AUGER-ELECTRON SPECTROSCOPY

While the satellite in the Cu $2p$ XP spectrum is a clear indication for Cu^{2+}, it is much harder to distinguish between Cu^0 and Cu^{1+}, because the main lines are overlapping. For this purpose, we examined the Cu $L_3M_{45}M_{45}$ Auger signal, which changes not only its position depending on the valence, but also its shape. The initial states of the Cu $L_3M_{45}M_{45}$ Auger process are the final states of the Cu $2p$ XP process, i.e., $2p^53d^{10}\underline{L}$ and $2p^53d^9$ for divalent copper and $2p^53d^{10}$ for monovalent copper. The corresponding Auger final states are $3d^8\underline{L}$ and $3d^7$ for divalent copper and $3d^8$ for monovalent copper.[19] In CuO, Cu_2O, and Cu samples, the Auger main lines were detected at kinetic energies of (918.0 ± 0.2), (916.7 ± 0.2), and (918.6 ± 0.2) eV, corresponding to divalent, monovalent, and elemental Cu, respectively.[21,36,38,39] However, in superconducting cuprates like Bi-Sr-Ca-Cu-O (Refs. 28 and 29) and Y-Ba-Cu-O,[34] the Cu $L_3M_{45}M_{45}$ lines are typically shifted by +0.5 eV due to the more complex chemical environment.

In Fig. 6 we present XAES data of the IL phase, the IL-r phase, and a Cu foil.[40] The Cu foil, serving as a reference for Cu^0, had a purity of 99.9 % and was cleaned *in situ* by sputtering prior to measurement. For all spectra, the intensities are normalized to zero at a kinetic energy of 930 eV and to unity at 910 eV. For better clarity, the different curves are shifted equidistantly along the vertical axis (normalized intensity) by 1. The dashed lines at 917.2, 918.5, and 919.1 eV indicate the values for Cu^{1+}, Cu^{2+}, and Cu^0 according to the literature, shifted by the above-mentioned +0.5 eV to account for the effect of the chemical environment. For the same reason, the Cu^0 spectrum was shifted by +0.5 eV as well. The characteristic structure of the Cu^0 spectrum from the Cu foil with its sharp main line and its multiplet features[41] allows for an unambiguous identification of elemental Cu.

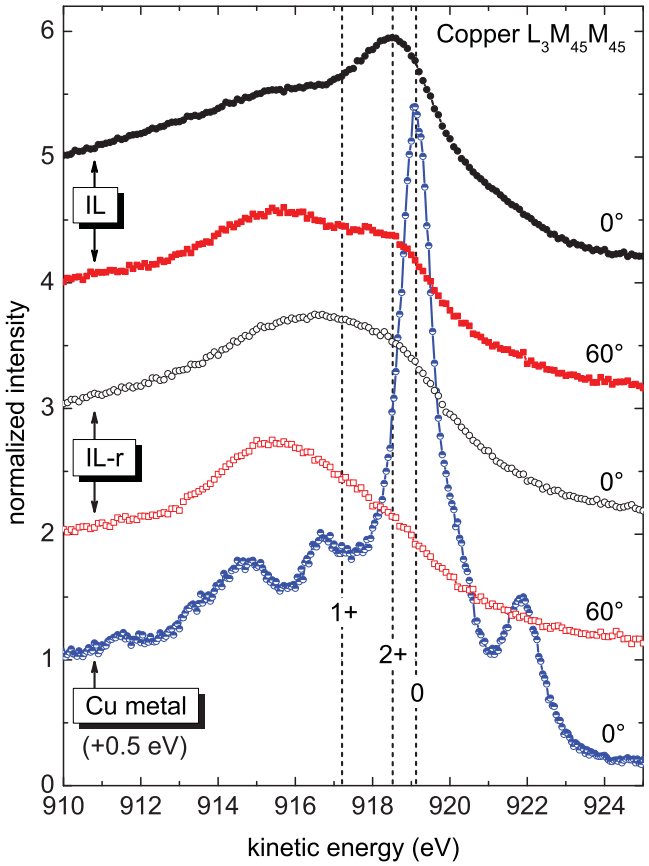

FIG. 6. (Color online) X-ray excited Cu $L_3M_{45}M_{45}$ Auger spectra of superconducting IL, insulating IL-r, and Cu reference sample, for normal (0°) and grazing incidence (60°). Curves are shifted equidistantly along the vertical axis by 1. The dashed lines indicate the peak positions of Cu^0, Cu^{1+}, and Cu^{2+} as expected for cuprate superconductors according to the literature (see text).

In the IL and IL-r spectra shown in Fig. 6, two main peaks are visible, one centered at ∼915 eV and the other at 918.5 eV. The two peaks are clearly separate in the IL phase but broadened and overlapping in the IL-r phase. We want to point out that a satellite, typically centered at 912–915 eV, is a common Auger feature of copper, copper oxides, copper dihalides, and superconducting cuprates. As the discussion of the satellite goes beyond the scope of this work, we refer to the work of Ramaker[42] and the literature cited therein. In the following, we will therefore focus on the main line.

A. XAES of the infinite-layer phase

As in our XP spectra, we can identify an XAES peak in Fig. 6 related to the superconducting phase, now at 918.5 eV, which is most prominent in the IL sample at normal emission. This peak has also been observed at the same energy in hole-doped cuprate superconductors like Y-Ba-Cu-O (Ref. 34) and Bi-Sr-Ca-Cu-O.[28,29] There, the Cu valence relating to this peak was determined as +2, in accordance with our XPS studies presented in Sec. IV A. We can further rule out the possibility that this peak stems from elemental Cu

because it is not possible to generate elemental Cu by an annealing step similar to ours[20,21] and because elemental Cu is highly susceptible to reoxidation in ambient air, even at room temperature. Furthermore, in contrast to the sharp main line of Cu^0, the main line of our IL sample is much broader. This broadening is generally observed in various copper oxides, such as Cu_2O, CuO, Bi-Sr-Ca-Cu-O, or Y-Ba-Cu-O, and it is attributed to Cu d–O p hybridization.[35]

Together with our XPS results (cf. Sec. IV A), we can now identify the valence of the reduced surface species as +1 and rule out elemental Cu due to its absence in the Auger spectra. As described above, we expect a line relating to Cu^{1+} in our Auger spectra at a kinetic energy of 917.2 eV. Indeed, a shift of the spectral weight toward lower kinetic energy was observed upon tilting the sample, hinting at Cu^{1+}. Yet a clear peak was not observed.

B. XAES of the infinite-layer-related phase

The XPS analysis on the IL-r phase did not reveal a remarkable variation of the Cu valence with information depth [cf. Fig. 5 (c)]. Again, XAES gives some more insight into this system, showing that there is some difference between bulk and surface (cf. Fig. 6). The broad XAES bulk spectrum with its maximum at 916.6 eV can only be explained by a superposition of peaks stemming from Cu^{2+} and Cu^{1+} as well as the satellite, in full agreement with our XPS results. Upon tilting, the spectral weight shifted toward lower kinetic energy, pointing to a dominant Cu^{1+} species on the surface. However, a weak signal relating to Cu^{2+} is still visible in the surface spectrum, again in agreement with our XPS results.

We can finally calculate the Auger parameter,[43] which is defined as the sum of the core-level binding energy (e.g., Cu $2p_{3/2}$) and the kinetic energy of the appropriate Auger electron (e.g., Cu $L_3M_{45}M_{45}$). For Cu^{2+} we find $934.1 + 918.5 = 1852.6$ eV and for Cu^{1+} $932.4 + 916.6 = 1849.0$ eV. Note that those values are even more strongly separated from each other than those reported for Bi-Sr-Ca-Cu-O (1851.8 and 1848.9 eV),[28] or for CuO and Cu_2O (1851.7 and 1848.9 eV).[36]

To conclude with Secs. IV and V, we detected divalent Cu in the bulk of the IL and mono- and divalent Cu in the bulk of the IL-r samples. Upon increasing the surface sensitivity, we found dominantly monovalent Cu on top of all samples.

VI. X-RAY DIFFRACTION

A. XRD of the infinite-layer phase

Figure 7 shows XRD data of the two films SLCO-1a and SLCO-2a that were previously examined by XPS and XAES (see Secs. IV and V). Both samples are c-axis oriented, as found by ϕ scans (not shown here). For SLCO-1a, which was vacuum annealed at 350 °C, no secondary phase could be identified, even in high-resolution Θ-2Θ scans, i.e., the sample is single phase with IL crystal structure and a c-axis parameter of 3.402 Å. Laue oscillations are visible, indicating high crystallographic quality along the film normal. The film thickness calculated from these oscillations is 23 ± 1 nm, corresponding to 68 ± 3 unit cells (uc). Reciprocal space mapping of the SLCO (303) peak showed a very sharp peak

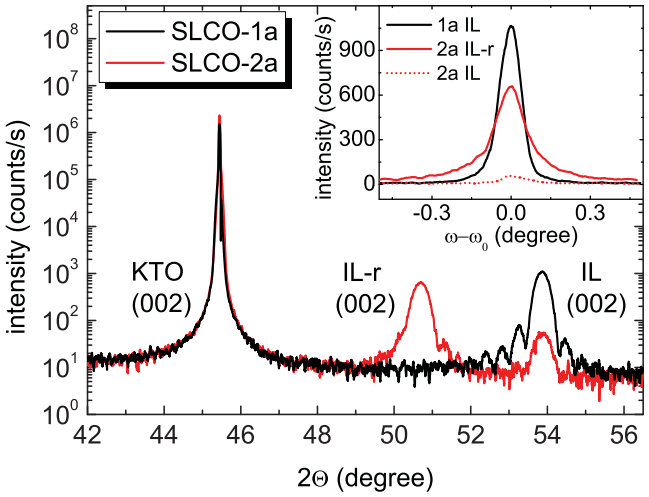

FIG. 7. (Color online) XRD data of (single-phase) IL thin-film SLCO-1a and of the strongly vacuum-annealed thin-film SLCO-2a with dominant IL-r phase. Main graph shows Θ-2Θ scans. Inset shows rocking curves around the (002) peaks.

without any extensions along the (100) direction (not shown here), i.e., the film is coherently strained. The in-plane lattice parameter was determined as 3.987 ± 0.002 Å which is close to the lattice parameter of the cubic KTO template, 3.9883 Å.

RHEED oscillations during film growth indicated a film thickness of 76 ± 3 uc, corresponding to 26 ± 1 nm, in contrast to the thickness determined by Laue oscillations. The thickness difference of a few nanometers can be attributed either to a defect-rich interface region close to the substrate or to a disordered film surface. Indeed, by means of XPS and XAES (see Secs. IV and V), a reduced SLCO surface layer with dominantly monovalent Cu was identified. We therefore favor the latter interpretation. Yet the absence of any signs of an IL-r phase in the XRD data of SLCO-1a implies that the reduced surface is *not* the IL-r phase. One possible explanation would be that the reduced surface still has an IL crystal structure but with (unordered) oxygen vacancies in the CuO_2 planes.

B. XRD of the infinite-layer-related phase

SLCO-2a, which was vacuum annealed at 550 °C, has an IL-r phase as major component and the IL phase as minor component. The c-axis parameters were determined as 3.598 Å for the major and 3.400 Å for the minor component. Again, Laue oscillations indicate high crystallographic quality along the film normal. With the aid of these oscillations, the film thickness was determined as 23 ± 2 nm for IL-r and 22 ± 2 nm for the infinite layer, i.e., the two phases coexist side by side and not on top of each other.

These results imply that the formation of the IL-r phase is not a process that develops along the film normal (from the surface to the bottom or vice versa) but it develops laterally on distinct nuclei. As shown elsewhere,[25] the coexistence of those two phases can even be imaged with an optical microscope due to their different optical reflection. We observed islandlike areas, which supports our interpretation of the XRD data described here. Moreover, the rocking curve of the IL-r (002) peak (for SLCO-2a) shows an increased full width at half

maximum $\Delta\omega = 0.14^\circ$ compared to the single-phase IL (002) peak (for SLCO-1a) with $\Delta\omega = 0.10^\circ$. We interpret this as a fingerprint of lattice distortions due to the coexistence of the two phases.

VII. CONCLUSIONS

We fabricated *in situ*–grown planar thin-film SLCO/Au/Nb junctions and investigated their electric transport properties. Our in-plane transport data show that below the Nb transition temperature, both electrodes are in the superconducting state. Regarding out-of-plane electric transport across the junctions, the absence of Cooper pair tunneling and the presence of quasiparticle tunneling from superconducting Nb (identified by a clear gap feature) to normal-conducting SLCO clearly indicates the presence of an insulating SLCO barrier layer on top of a normal conducting SLCO layer at the interface between the superconducting bottom SLCO electrode and the Au interlayer. Such an insulating/normal-conducting SLCO surface layer is likely to be formed during vacuum annealing of the infinite layer cuprate superconductor SLCO after film growth.

In order to check the interpretation of our electric transport data, we examined the electronic structure and valence states of the SLCO surface layer. This was done by performing XPS and XAES measurements on two SLCO thin films, which were fabricated under nominally identical conditions as for the bottom SLCO electrode in the SLCO/Au/Nb junctions. After high-temperature vacuum annealing in the XPS/XAES setup, one of the two SLCO films was reduced, which transformed this film predominantly into the infinite-layer-related phase, while the other film was examined as representative for the IL phase. Upon tilting the IL sample (reducing the XPS/XAES information depth from ~6 to ~3 nm), we identified a reduced surface (with Cu valence +1 or 0) and oxidized bulk (with Cu valence +2) component via XPS measurements. In order to determine the Cu valences at the surface, XAES measurements were performed, which identified Cu^{1+} on the surface of both the IL and IL-r samples. The comparison of XP spectra of superconducting IL and nonsuperconducting IL-r samples allows us to relate the bulk signals for Sr, O, and Cu in the IL sample to the superconducting IL phase. Moreover, this comparison also allows us to identify the signatures of the IL-r component in the XP/XAE spectra and shows that the unit cell of the IL-r compound contains mixed Cu valences (+1 and +2). X-ray diffraction data indicate a disordered surface layer of ~3 nm thickness, which is consistent with both the XPS/XAES data and the out-of-plane transport data.

We can consistently interpret all our data, if we assume that the SLCO surface layer with Cu valence +1 is insulating. A likely scenario for its formation is the formation of a gradient of disordered oxygen vacancies along the SLCO film normal within the uppermost few nanometers. This could be due to the annealing step right after film deposition, and hence should occur for the SLCO films as well as for the SLCO films within the SLCO/Au/Nb trilayer structures. On the one hand, such a gradient of oxygen vacancies can explain the XPS/XAES data (i.e., change in Cu valence states from +2 in the bulk to +1 on the surface). On the other hand, such a gradient can be assumed to change the SLCO films from superconducting to normal conducting and finally insulating, along the surface normal, close to the SLCO film surface or SLCO/Au interface. This is supported by our out-of-plane transport data. Hence, our electric transport data for the SLCO/Au/Nb junctions are fully consistent with the XPS/XAES and XRD data on our SLCO thin films.

ACKNOWLEDGMENTS

J.T. gratefully acknowledges support by the Evangelisches Studienwerk e. V. Villigst. V.L. acknowledges partial financial support by the Romanian Ministry of Education and Research (Human Resources Reintegration Project No. 1476/2006) and by CNCSIS-UEFISCSU (Project No. PNII-IDEI ID_743/2007). This work was funded by the Deutsche Forschungsgemeinschaft (Project No. KL 930/11).

*koelle@uni-tuebingen.de

[1] Y. Tokura, H. Takagi, and S. Uchida, Nature (London) **337**, 345 (1989).
[2] H. Takagi, S. Uchida, and Y. Tokura, Phys. Rev. Lett. **62**, 1197 (1989).
[3] M. G. Smith, A. Manthiram, J. Zhou, J. B. Goodenough, and J. T. Markert, Nature (London) **351**, 549 (1991).
[4] G. Er, S. Kikkawa, F. Kanamaru, Y. Miyamoto, S. Tanaka, M. Sera, M. Sato, Z. Hiroi, M. Takano, and Y. Bando, Physica C **196**, 271 (1992).
[5] H. Shaked, Y. Shimakawa, B. A. Hunter, R. L. Hitterman, J. D. Jorgensen, P. D. Han, and D. A. Payne, Phys. Rev. B **51**, 11784 (1995).
[6] T. Siegrist, S. M. Zahurak, D. W. Murphy, and R. S. Roth, Nature (London) **334**, 231 (1988).
[7] G. Er, Y. Miyamoto, F. Kanamaru, and S. Kikkawa, Physica C **181**, 206 (1991).
[8] N. Ikeda, Z. Hiroi, M. Azuma, M. Takano, Y. Bando, and Y. Takeda, Physica C **210**, 367 (1993).
[9] J. D. Jorgensen, P. G. Radaelli, D. G. Hinks, J. L. Wagner, S. Kikkawa, G. Er, and F. Kanamaru, Phys. Rev. B **47**, 14654 (1993).
[10] C. Niu and C. M. Lieber, Appl. Phys. Lett. **61**, 1712 (1992).
[11] H. Adachi, T. Satoh, Y. Ichikawa, K. Setsune, and K. Wasa, Physica C **196**, 14 (1992).
[12] S. Karimoto, K. Ueda, M. Naito, and T. Imai, Appl. Phys. Lett. **79**, 2767 (2001).
[13] M. Naito, H. Sato, and H. Yamamoto, Physica C **293**, 36 (1997).
[14] Z. Z. Li, V. Jovanovic, H. Raffy, and S. Megtert, Physica C **469**, 73 (2009).
[15] V. Leca, D. H. A. Blank, G. Rijnders, S. Bals, and G. van Tendeloo, Appl. Phys. Lett. **89**, 092504 (2006).
[16] V. Leca, G. Visanescu, C. Back, R. Kleiner, and D. Koelle, Appl. Phys. A **93**, 779 (2008).

[17]S. I. Karimoto and M. Naito, Appl. Phys. Lett. **84**, 2136 (2004).
[18]B. Mercey, A. Gupta, M. Hervieu, and B. Raveau, J. Solid State Chem. **116**, 300 (1995).
[19]J. Ghijsen, L. H. Tjeng, J. van Elp, H. Eskes, J. Westerink, G. A. Sawatzky, and M. T. Czyzyk, Phys. Rev. B **38**, 11322 (1988).
[20]S. Poulston, P. M. Parlett, P. Stone, and M. Bowker, Surf. Interface Anal. **24**, 811 (1996).
[21]P. D. Kirsch and J. G. Ekerdt, J. Appl. Phys. **90**, 4256 (2001).
[22]Chemco GmbH, Germany.
[23]Crystal GmbH, Germany.
[24]See Supplemental Material at http://link.aps.org/supplemental/10.1103/PhysRevB.84.064521 for Electric transport across $Sr_{1-x}La_xCuO_2$/Au/Nb planar tunnel junctions and x-ray photoelectron and Auger-electron spectroscopy on $Sr_{1-x}La_xCuO_2$ thin films.
[25]V. Leca *et al.* (unpublished).
[26]Computer code UNIFIT, Spectrum Processing, Analysis and Presentation Software for Photoelectron Spectra, Unifit Scientific Software GmbH, University Leipzig, Germany.
[27]R. P. Vasquez, C. U. Jung, J. Y. Kim, M.-S. Park, H.-J. Kim, and S.-I. Lee, J. Phys.: Condens. Matter **13**, 7977 (2001).
[28]S. Kohiki, K. Hirochi, H. Adachi, K. Setsune, and K. Wasa, Phys. Rev. B **38**, 9201 (1988).
[29]F. U. Hillebrecht, J. Fraxedas, L. Ley, H. J. Trodahl, J. Zaanen, W. Braun, M. Mast, H. Petersen, M. Schaible, L. C. Bourne *et al.*, Phys. Rev. B **39**, 236 (1989).
[30]P. Kulkarni, S. K. Kulkarni, A. S. Nigavekar, S. K. Agarwal, V. P. S. Awana, and A. V. Narlikar, Physica C **166**, 530 (1990).
[31]R. P. Vasquez, J. Electron Spectrosc. Relat. Phenom. **56**, 217 (1991).
[32]H. van Doveren and J. A. T. Verhoeven, J. Electron Spectrosc. Relat. Phenom. **21**, 265 (1980).
[33]P. Alméras, H. Berger, and G. Margaritondo, Solid State Commun. **87**, 425 (1993).
[34]D. van der Marel, J. van Elp, G. A. Sawatzky, and D. Heitmann, Phys. Rev. B **37**, 5136 (1988).
[35]G. van der Laan, C. Westra, C. Haas, and G. A. Sawatzky, Phys. Rev. B **23**, 4369 (1981).
[36]J. P. Tobin, W. Hirschwald, and J. Cunningham, Appl. Surf. Sci. **16**, 441 (1983).
[37]M. Nagoshi, Y. Syono, M. Tachiki, and Y. Fukuda, Phys. Rev. B **51**, 9352 (1995).
[38]S. W. Gaarenstroom and N. Winograd, J. Chem. Phys. **67**, 3500 (1977).
[39]R. J. Bird and P. Swift, J. Electron Spectrosc. Relat. Phenom. **21**, 227 (1980).
[40]Goodfellow GmbH, Germany.
[41]S. P. Kowalczyk, R. A. Pollak, F. R. McFeely, L. Ley, and D. A. Shirley, Phys. Rev. B **8**, 2387 (1973).
[42]D. E. Ramaker, J. Electron Spectrosc. Relat. Phenom. **66**, 269 (1994).
[43]C. D. Wagner, Anal. Chem. **44**, 967 (1972).

Supplemental information for: Phys. Rev. B 84, 064521 (2011) Electric transport across $Sr_{1-x}La_xCuO_2$/Au/Nb planar tunnel junctions and x-ray photoelectron and Auger-electron spectroscopy on $Sr_{1-x}La_xCuO_2$ thin films

J. Tomaschko, C. Raisch, V. Leca, T. Chassé, R. Kleiner, and D. Koelle

This supplement describes in detail the patterning procedure for planar tunnel junction (PTJ) fabrication, which is based on optical lithography and Ar^+ ion milling. We use a self-alignment process for final definition of the PTJ area, which ensures alignment of the metallic wiring layer with the upper electrode of the PTJ and which prevents exposure of the junction edges to chemicals during any time in the patterning process. The PTJs were patterned in four steps, which we denote as (I) contact pad patterning, (II) edge isolation, (III) metallization, and (IV) junction milling.

During Ar^+ milling (beam energy 0.3 keV), the sample was mounted on a water-cooled ($T \approx 8\,^\circ$C) copper block which reduces heating of the sample. A shutter in front of the sample was used to mill in intervals of $t_o = 5$ s open and $t_c = 10$ s closed. This helps to avoid excessive heating of the sample surface, which might induce interdiffusion at the interface and oxygen loss in the SLCO layer, which has a detrimental effect on the Cooper pair or quasiparticle tunneling properties.

I. CONTACT PAD PATTERNING

This step defines the contact pads of the PTJ. Figure 1(a) shows a cross section of the as-grown sample, indicating the stacking sequence. The 26 nm thick SLCO and the 21 nm thick Nb electrodes are separated by a 5 nm thick Au layer, protecting both electrodes from mutual reduction or oxidation, respectively. In a first step, the sample was coated by photoresist (PR) which was patterned by optical lithography [c.f. Fig. 1(b)]. Subsequently, the sample was loaded into the milling chamber and the regions exposed to Ar^+ ions were milled down into the KTO substrate. Figure 1(c) shows the cross section after PR removal in acetone and Fig. 1(d) shows the corresponding top view.

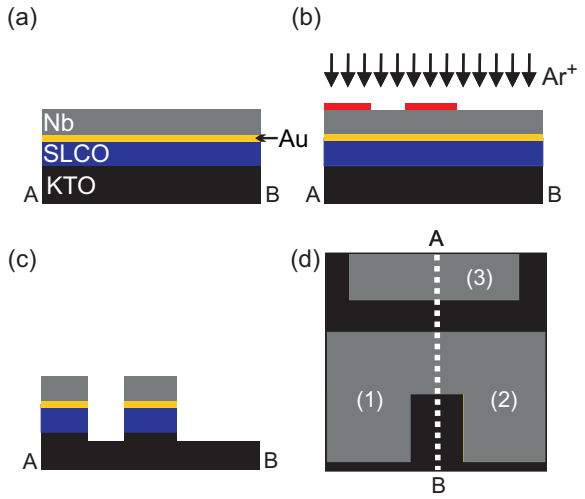

FIG. 1: **Contact pad patterning:** cross sections of the sample, (a) prior to patterning, (b) before, and (c) after Ar^+ ion milling and removal of PR. (d) shows top view corresponding to (c); white dashed line indicates the position of cross sections $\overline{AB}$ shown in (a)-(c).

II. EDGE ISOLATION

The next step provides isolation of the contact pads and of the short edges of the PTJ by an SiO_2 layer and at the same time defines the length (along $\overline{AB}$) of the PTJ. Here, a mask was used which had essentially the same geometry as the one used for contact pad patterning. However, the structures on this mask are slightly smaller, i.e. their edges are shifted by 10 μm with respect to the previous mask; c.f. Fig. 2(a). Furthermore, Ar^+ ion milling is stopped after milling into the bottom SLCO electrode as indicated in Fig. 2(b). Subsequently, we sputtered ~ 10 nm of SiO_2 in a Ar/O_2 atmosphere (at 200 Pa), followed by lift-off. This process results in the structure shown in Figs. 2(c) and (d).

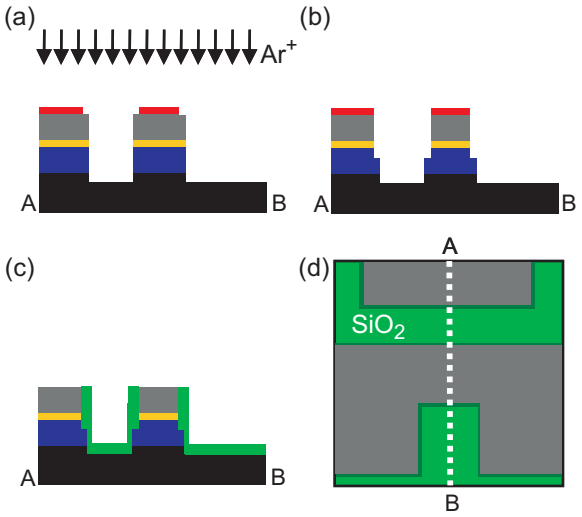

FIG. 2: **Edge isolation:** cross sections of the sample, (a) before, and (b) after Ar^+ ion milling into the bottom SLCO layer. (c) shows the structure after deposition of an SiO_2 layer and lift-off patterning (removal of PR). (d) shows top view corresponding to (c); white dashed line indicates the position of cross sections $\overline{AB}$ shown in (a)-(c).

III. METALLIZATION

Step III provides a connection between the upper Nb electrode of the PTJ and pad (3). This step starts with preparation of a lift-off mask [c.f. Fig. 3(a)], which covers everywhere, except for the light grey areas in Fig. 3(d). Subsequently, the sample is milled for a few seconds to remove the degraded Nb surface ($\sim 1\,$nm) which formed during the the previously described patterning process. Then, a 5 nm thick Au protection layer is sputtered without breaking the vacuum, before transferring the sample to the Nb sputtering setup and depositing 100 nm of Nb. This Au/Nb bilayer is patterned by lift-off and will be used as a milling mask in step IV. Figures 3(b) and (c) show vertical ($\overline{AB}$) and horizontal ($\overline{CD}$) cross sections, respectively, after this step. Figure 3(d) shows the corresponding top view at the end of this metallization process. The width of the central Au/Nb strip (along $\overline{CD}$) defines the width of the PTJ.

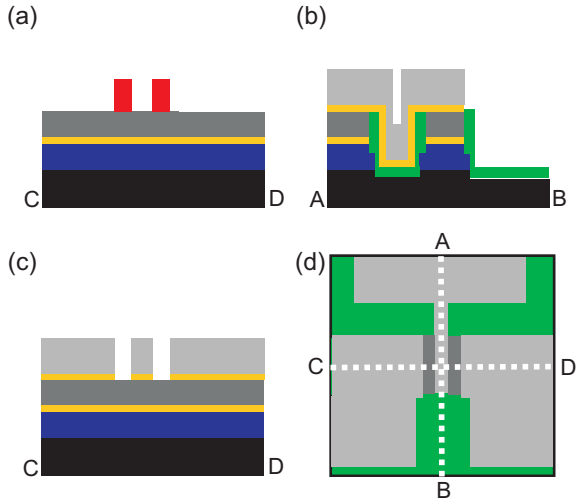

FIG. 3: **Metallization:** cross sections of the sample, (a) after patterning a lift-off mask, and (b),(c) after Au/Nb bilayer deposition and lift-off patterning (removal of PR). (d) shows top view corresponding to (b) and (c); white dashed lines indicate the position of the cross sections $\overline{AB}$ and $\overline{CD}$ shown in (a), (b), and (c).

IV. JUNCTION MILLING

Step IV is the final patterning step of the PTJ, using a self-alignment method. Here, the whole sample area is milled with Ar^+, without any PR [c.f Fig. 4(a)]. During milling, the areas uncovered by the 100 nm thick Nb top layer are milled down to the KTO substrate or to the bottom SLCO electrode as shown in Figs. 4(b) and (c), respectively. This step is possible, as the Nb top layer is thicker than the Nb electrode of the SLCO/Au/Nb trilayer. The final top view, shown in Fig. 4(d), is a schematic representation of the optical image shown in Fig. 1 in the main paper.

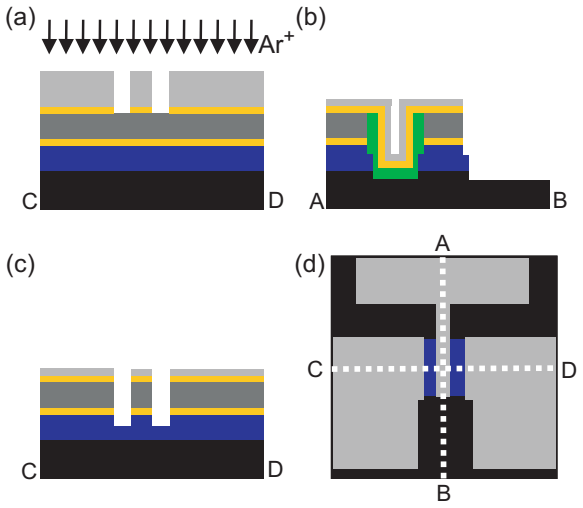

FIG. 4: **Junction milling:** cross sections of the sample, (a) at the start of Ar^+ milling, and (b),(c) after Ar^+ milling. (d) shows top view corresponding to (b) and (c); white dashed lines indicate the position of the cross sections $\overline{AB}$ and $\overline{CD}$ shown in (a), (b), and (c).

Publication III

Importance of grain-boundary Josephson junctions in the electron-doped infinite-layer cuprate superconductor $Sr_{1-x}La_xCuO_2$

J. Tomaschko,[1] V. Leca,[1,2] T. Selistrovski,[1] R. Kleiner,[1] and D. Koelle[1,*]

[1]*Physikalisches Institut – Experimentalphysik II and Center for Collective Quantum Phenomena in LISA$^+$, Universität Tübingen, Auf der Morgenstelle 14, DE-72076 Tübingen, Germany*

[2]*Faculty of Applied Chemistry and Materials Science, University Politehnica of Bucharest, Gheorghe Polizu Street 1-7, Bucharest RO-011061, Romania*

(Received 6 September 2011; published 5 December 2011)

Grain-boundary bicrystal Josephson junctions of the electron-doped infinite-layer superconductor $Sr_{1-x}La_xCuO_2$ ($x = 0.15$) were grown by pulsed laser deposition. $BaTiO_3$-buffered 24° [001]-tilt symmetric $SrTiO_3$ bicrystals were used as substrates. We examined both Cooper pair (CP) and quasiparticle (QP) tunneling by electric transport measurements at temperatures down to 4.2K. CP tunneling revealed an extraordinary high critical current density for electron-doped cuprates of $j_c > 10^3$ A/cm^2 at 4.2 K. Thermally activated phase slippage was observed as a dissipative mechanism close to the transition temperature. Out-of-plane magnetic fields H revealed a remarkably regular Fraunhofer-like $j_c(H)$ pattern as well as Fiske and flux-flow resonances, both yielding a Swihart velocity of 3.1×10^6 m/s. Furthermore, we examined the superconducting gap by means of QP tunneling spectroscopy. The gap was found to be V shaped with an extrapolated zero-temperature energy gap $\Delta_0 \approx 2.4$ meV. No zero-bias conductance peak was observed.

DOI: 10.1103/PhysRevB.84.214507 PACS number(s): 74.50.+r, 74.72.Ek, 61.72.Mm, 74.25.Sv

I. INTRODUCTION

Only two families of electron-doped high transition temperature (high-T_c) cuprate superconductors are known: the T' compounds[1,2] and the infinite-layer (IL) compounds[3–5] $A^{II}_{1-x}Ln^{III}_xCuO_2$ (where A^{II} is a divalent alkaline-earth metal and Ln^{III} is a trivalent lanthanide). The IL compounds exhibit the simplest crystal structure among all cuprate superconductors and are therefore predestined to examine the nature of high-T_c superconductivity. However, as the fabrication of high-quality superconducting IL samples is challenging, these compounds have been less examined than any other cuprate superconductor. High-pressure preparation is necessary to stabilize the superconducting IL phase, yielding polycrystalline bulk material.[6–8] To obtain single-crystalline samples, IL thin films were deposited epitaxially on single-crystalline templates.[9–11] After it had been shown that compressive strain hinders electron doping of the CuO_2 planes, buffer layers were introduced,[10] enhancing the T_c close to the maximum of 43 K.[5,11]

The importance of grain-boundary Josephson junctions (GBJs) in the high-T_c cuprates has been demonstrated by various experiments (see, e.g., reviews 12–14, and references therein). Chaudhari *et al.*[15] realized the first single $YBa_2Cu_3O_{7-\delta}$ (YBCO) GBJs. They showed that such GBJs act as weak links, which later on have been used, e.g., for the realization of sensitive high-T_c superconducting quantum interference devices (SQUIDs).[16] In particular, cuprate GBJs played a decisive role in experimental tests on the determination of the superconducting order-parameter symmetry of the cuprates.[17] For example, Alff *et al.*[18] observed an increased conductance across various high-T_c GBJs at low voltage, a so-called zero-bias conductance peak (ZBCP), which was explained by the formation of zero-energy surface states [so-called Andreev bound states (ABS)] due to d-wave pairing of the underlying material.[19–21] Tsuei *et al.*[22] revealed d-wave pairing in YBCO with superconducting rings containing three GBJs. Schulz *et al.*[23] realized an all high-T_c 0-π-SQUID comprising two YBCO GBJs with phase shifts of 0 and π, respectively, to prove d-wave pairing in YBCO, and later on a similar experiment was done for the electron-doped T' compound $La_{2-x}Ce_xCuO_{4-\delta}$.[24] And Lombardi *et al.*[25] found an oscillatory dependence of the critical current density j_c on the GBJ misorientation angle, as an indication of d-wave pairing in YBCO.

However, so far all experiments on IL cuprates have only been performed on bulk polycrystals or single-crystalline thin films, but no Josephson devices have been fabricated. Very recently, we reported on thin-film planar $Sr_{1-x}La_xCuO_2$ (SLCO)/Au/Nb junctions,[26] which showed quasiparticle (QP) tunneling, but no Cooper pair (CP) tunneling. In this work, we report on the fabrication and characterization of SLCO bicrystal GBJs. We found high j_c well below T_c, thermally activated phase slippage close to T_c, very regular Fraunhofer-like j_c vs magnetic field H patterns, as well as Fiske and flux-flow resonances as remarkable features of CP tunneling. QP tunneling essentially revealed a well-defined, V-shaped gap but did not show any ZBCP. Such devices may give new insights into basic properties of the IL cuprates and allow for a comparison with the properties of GBJs based on other hole- and electron-doped cuprates. Moreover, the pairing symmetry of the IL cuprates is still an open question and phase-sensitive experiments based on SLCO GBJs could help find the answer.

II. SAMPLE FABRICATION AND EXPERIMENTAL SETUP

To fabricate SLCO GBJs, we deposited SLCO thin films on $BaTiO_3$-buffered symmetric [001]-tilt $SrTiO_3$ bicrystals with misorientation angle $\theta = 24°$ by pulsed laser deposition (cf. Ref. 26). Further details will be described elsewhere.[27] Four chips, each with seven junctions, have been fabricated and characterized. All SLCO GBJs showed comparable properties,

which verifies reproducibility of our data. For simplicity, data presented in this work stems from one chip. The SLCO films with thickness $t \sim 25$ nm are c-axis oriented, as confirmed by x-ray diffraction, i.e., current flow is restricted to the ab plane. Each chip was patterned via standard photolithography and argon ion milling to create junctions with widths w ranging between 10 and 1000 μm. Electric transport measurements were performed in a four-point configuration, with the sample mounted inside a noise-filtered, magnetically and radio frequency shielded probe in a liquid-helium dewar.

III. ELECTRIC TRANSPORT PROPERTIES AT ZERO MAGNETIC FIELD

Figure 1(a) shows bias current I vs voltage V characteristics (IVCs) of a 50-μm-wide junction at various temperatures T and $H = 0$. The IVCs are resistively and capacitively shunted junction (RCSJ) -like and do not show a significant excess current. At low T there is a small hysteresis [cf. inset of Fig. 1(a)], corresponding to a Stewart-McCumber parameter $\beta_c = 2\pi I_0 R_n^2 C/\Phi_0$ slightly above 1. Here, I_0 is the maximum Josephson current in the absence of thermal noise, and R_n and C are the normal resistance and capacitance of the junction, respectively; Φ_0 is the magnetic flux quantum. By comparison of measured IVCs with numerical RCSJ simulations including thermal noise, we determined $\beta_c(T)$ and the noise parameter (thermal energy divided by Josephson coupling energy) $\Gamma(T) \equiv 2\pi k_B T/[I_0(T)\Phi_0]$; k_B is the Boltzmann constant.

With the 4.2-K values $\beta_c = 3.5$ and $\Gamma = 0.01$ and the measured $R_n = 10\ \Omega$, we find $I_0 = 17.6\ \mu$A and $C = 0.65$ pF. The 4.2-K value for I_0 corresponds to a critical current density $j_0 \approx 1.4$ kA/cm^2. This value is two orders of magnitude below j_0 values for corresponding ($\theta = 24^\circ$) YBCO GBJs,[28] but two orders of magnitude above j_0 of GBJs from electron-doped T' compounds such as $Nd_{2-x}Ce_xCuO_{4-\delta}$ (NCCO)[29] and $La_{2-x}Ce_xCuO_{4-\delta}$ (LCCO),[30] thus, probably the highest reported j_0 value for electron-doped cuprate GBJs. The 4.2-K value for C corresponds to a capacitance per junction area $C/A \approx 50\ \mu$F/cm^2, which is by a factor of $\sim$20 larger than typical C/A values of YBCO GBJs.[14,31]

With increasing T, j_0 decreases nonlinearly, as shown in Fig. 1(b). For 10 K $\leqslant T \leqslant$ 19 K, we find a power-law behavior $j_0 \propto (1 - T/T_c)^\alpha$ with $\alpha = 2.0 \pm 0.1$. Such quadratic behavior was explained by a reduction of the order parameter Δ at the GB interface due to the small coherence length ξ of the cuprate superconductors.[32] For lower T, high-T_c GBJs usually exhibit a linear $j_0(T)$ dependence.[14] Contrary to that, we observed a monotonous decrease in $|dj_0/dT|$ with decreasing T below $\sim$9 K. This resembles the behavior of an early YBCO GBJ, reported by Mannhart *et al.*[33] in good agreement with the Ambegaokar-Baratoff relation,[34] which is valid for superconductor-insulator-superconductor (SIS) junctions.

Figure 1(c) shows $R(T)$ curves measured with different bias currents I. To access the normal resistance R_n of the GBJ, in one case an overcritical current $I = 30\ \mu$A was applied. We found, that R_n increases from 7.1 to 10.1 Ω when T is lowered from 19 to 4.2 K, corresponding to an areal resistance $\rho_n \equiv R_n A = 0.09$–$0.13\ \mu\Omega\,$cm^2. Thus, ρ_n is in between the values reported for YBCO GBJs (10^{-3}–$10^{-2}\ \mu\Omega$cm^2)[28,35]

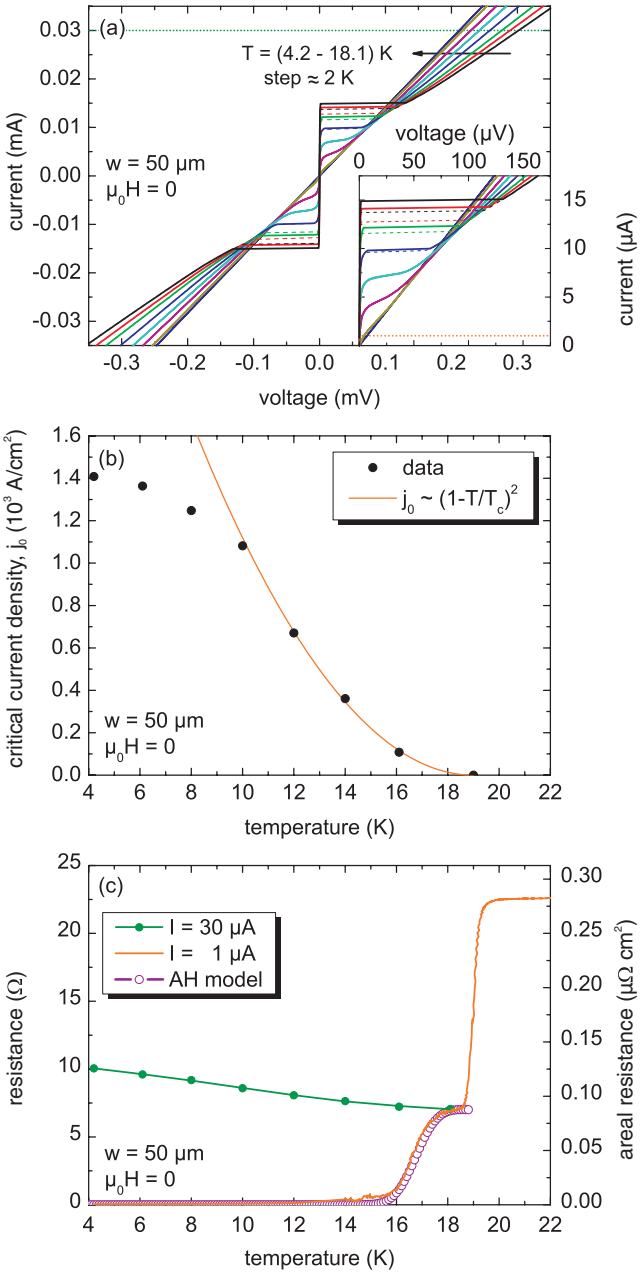

FIG. 1. (Color online) Electric transport characteristics at $H = 0$ for 50-μm-wide SLCO GBJ. (a) Current-voltage curves at different temperatures. Inset shows an expanded view. Curves for decreasing I are shown as dashed lines. The horizontal dotted lines indicate the values used for I in (c). (b) Critical current density j_0 vs T. Values (full symbols) were determined by RCSJ fits of the IVCs. The line is a parabolic fit of the data for $T \geqslant 10$ K. (c) Resistance vs temperature, measured with different bias currents. The curve shown for $I = 30\,\mu\text{A} \approx 2I_c(4.2\,\text{K})$ corresponds to the normal resistance R_n of the junction. Open symbols show the calculated resistance according to the Ambegaokar-Halperin (AH) model.

and the values for GBJs from the T' compounds NCCO (1–10 $\mu\Omega\,$cm^2)[29] and LCCO (30–130 $\mu\Omega\,$cm^2) GBJs.[30]

We further find $I_0 R_n \sim 0.18$ mV at 4.2 K, which is comparable to values for NCCO GBJs,[29] but one to two orders

of magnitude smaller than the products (∼1–8mV) reported for LCCO GBJs[30] or YBCO GBJs.[28] We note that our values of I_0R_n and j_0 fall right onto the scaling line $I_0R_n \propto 1/\rho_n^{1.5}$ shown by Gross and Mayer[36] for YBCO GBJs, which was suggested to be related to the oxygen stoichiometry at the barrier. Thus, we speculate that our small I_0R_n product is a fingerprint of oxygen vacancies at the barrier due to vacuum annealing[26,27] of the as-deposited SLCO films, which would also be in line with the conclusions of Hilgenkamp and Mannhart.[14] The intrinsically shunted junction (ISJ) model[14,36] is based upon such barrier defects, which are supposed to form localized states. On the one hand, localized states suppress Δ at the grain-boundary interface. On the other hand, they enable resonant QP tunneling across the barrier. The former point is in accordance with our observed quadratic $j_0(T)$ behavior close to T_c and it further explains the small I_0R_n products. The latter one explains the small ρ_n, because resonant tunneling is consistent with a highly transparent barrier. Finally, we want to remark, that our small I_0R_n product is comparable to values reported for those T'-compound GBJs[29,30] which did *not* exhibit a ZBCP.

We next discuss the resistive transition, which is also shown in Fig. 1(c) as the $R(T)$ curve measured with small bias current $I = 1\,\mu$A. Upon decreasing T, we first find a sharp decrease in R, which we associate with the transition of the SLCO film to the superconducting state, with $T_c = 19.0$ K and the width of the resistive transition $\Delta T_c \approx 0.5$ K. We note that the observed value of T_c is only about half of the maximum T_c value reported for SLCO.[5,11] This can be attributed to nonoptimum doping of our SLCO films ($x = 0.15$) and/or to strain effects due to the lattice mismatch of the $BaTiO_3$ buffer layer and SLCO ($a_{\mathrm{BTO}} = 3.997$ Å, $a^{\mathrm{bulk}}_{\mathrm{SLCO}} = 3.949$ Å).[26,37] For $T < T_c$ down to ∼15 K, we observe a "foot structure" in $R(T)$. Such behavior has been observed, e.g., in YBCO and NCCO GBJs before and was attributed to thermally activated phase slippage (TAPS),[29,38] as described by Ambegaokar and Halperin.[39] Within the AH model, a finite resistance due to TAPS is given by $R_p(T) = R_n(T)J_0^{-2}[\Gamma^{-1}(T)]$. Here, $J_0[x]$ is the modified Bessel function of the first kind. We calculate $R_p(T)$ using the quadratic $j_0(T)$ dependence close to T_c [cf. Fig. 1(b)], and the measured $R_n(T)$. Similar calculations for other SLCO GBJs with different widths also yielded very good agreement. Thus, we verified that TAPS is present in our samples and is responsible for the finite slope of the $I(V)$ curves ($dI/dV|_{V=0} \neq \infty$) close to T_c [cf. Fig. 1(a)].

IV. ELECTRIC TRANSPORT PROPERTIES VS MAGNETIC FIELD

Figure 2(a) shows IVCs of the 50-μm-wide junction at different magnetic fields H and constant $T = 4.2$ K. H was applied perpendicular to the film plane. The modulation of the critical current density $j_c(H)$ (measured with a voltage criterion $V_c = 5\,\mu$V) is shown in Fig. 2(b) (lower curve). We observed a remarkably regular Fraunhofer-like pattern with oscillations visible throughout the entire scanned field range (±65 μT) (here, we only show the pattern for $|\mu_0 H| \leqslant 30\,\mu$T for clarity). The oscillation period $\mu_0\Delta H$ for this junction is 1.6 μT. In the thin-film limit ($\lambda_L^2/t \gg w$; λ_L is the London

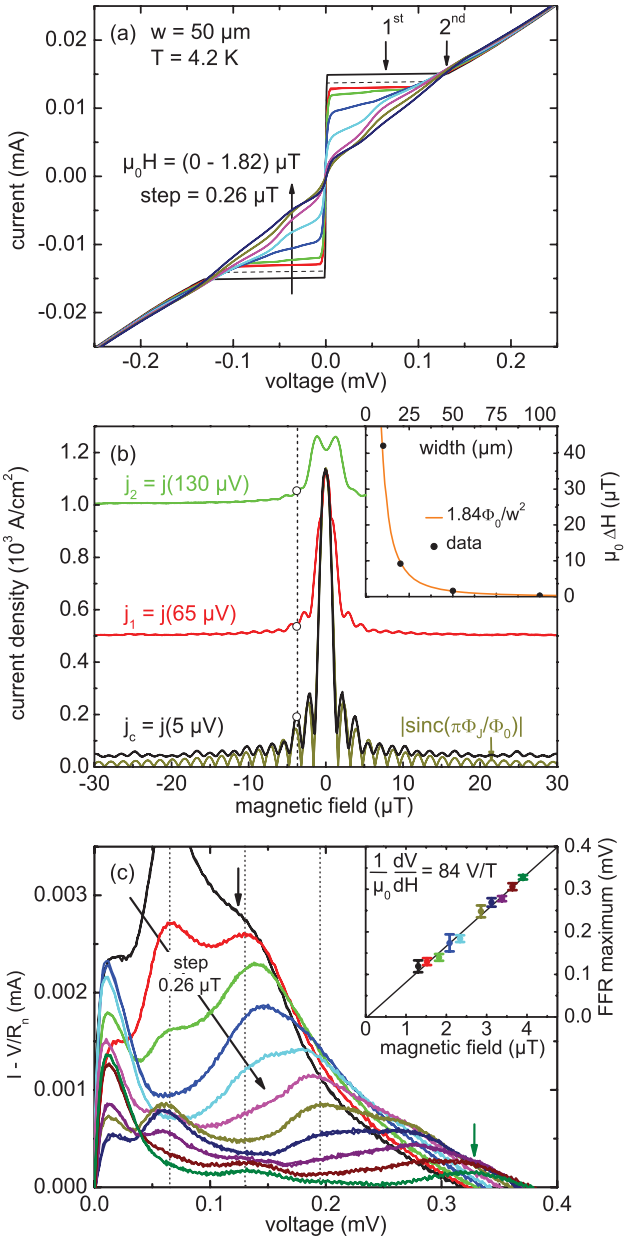

FIG. 2. (Color online) (a) Current-voltage curves of 50-μm-wide SLCO GBJ for different values of $H \parallel c$ axis ($T = 4.2$ K). (b) Magnetic field dependence of the critical current density j_c and the currents j_1 and j_2 at the first and second Fiske resonance, respectively. For comparison with $j_c(H)$, an ideal Fraunhofer patten is also shown. The inset shows the oscillation period $\mu_0\Delta H$ of $j_c(H)$ vs the width of four SLCO GBJs as full circles. The theoretical dependence (Ref. 40) $\mu_0\Delta H = 1.84\Phi_0/w^2$ is shown as a solid line. (c) Current-voltage curves, with the normal current $I_n = V/R_n$ subtracted from the bias current, for $\mu_0 H = 1.3$–$3.9\,\mu$T. Vertical lines indicate Fiske resonances and arrows indicate the position of the flux-flow resonance (FFR) maximum (for 1.3 and 3.9 μT). The inset shows the linear magnetic field dependence of the FFR maximum.

penetration depth), a perpendicular field is focused into the GBJ by the superconducting electrodes and the modulation period becomes[40] $\mu_0\Delta H = 1.84\Phi_0/w^2$, which is *independent of* λ_L. By analyzing four junctions with different widths w on

the same chip, we verified this dependence, as shown in the inset of Fig. 2(b).

At $|V| \approx 65$ and 130 μV, resonant features appear in the IVCs [cf. arrows in Fig. 2(a), labeled as "1st" and "2nd"]. The amplitude of enhanced current (as compared to a linear IVC) shows an oscillatory dependence on H with the same period as $j_c(H)$. This is shown in Fig. 2(b), where we also plot the current densities $j_1 \equiv j(65\,\mu\text{V})$ and $j_2 \equiv j(130\,\mu\text{V})$ at the first and second resonance, respectively. The first resonance has its minima when $j_c(H)$ and the second resonance are near their maxima [cf. vertical dotted line in Fig. 2(b)], characteristic for Fiske resonances,[41] i.e., standing electromagnetic waves in the junction. The Fiske resonances appear at equidistant voltages $V_n = \Phi_0 c_S n/2w$, where c_S denotes the Swihart velocity[42] and $n = 1,2,3,\ldots$. From the measured V_n we find $c_S = 3.1 \times 10^6$ m/s, which is comparable to $c_S^{\text{YBCO}} \approx 10^7$ m/s found for YBCO GBJs.[31,43] For the 10-, 20-, and 100-μm-wide junctions the first Fiske resonance appeared at $V_1 = 316$, 167, and 31 μV, respectively, yielding $c_S = 3.1$, 3.2, and 3.0×10^6 m/s.

In Fig. 2(c), the current $I_n = V/R_n$ has been subtracted from the bias current I to show the resonances in the IVCs (for various values of H) more clearly. For some field values, the positions of the Fiske resonances are marked by vertical dashed lines. Besides Fiske resonances, a resonance is visible with its maximum position V_m shifting $\propto H$ (cf. arrows and inset). The peak height of this resonance decreases monotonically with H, which is indicative of a Josephson flux-flow resonance (FFR).[44] The peak position of the FFR in *thin-film* GBJs is given by[43] $V_m = d_B c_S \mu_0 H F$, where d_B denotes the effective barrier thickness and $F \approx \Phi_0/(w d_B \mu_0 \Delta H)$ accounts for flux focusing.[40] The inset in Fig. 2(c) shows V_m vs $\mu_0 H$. From the slope $V_m/\mu_0 H = (84 \pm 2)$ V/T and $\mu_0 \Delta H = 1.6\,\mu$T we extract $c_S = (3.2 \pm 0.1) \times 10^6$ m/s, in agreement with the value determined from Fiske resonances.

V. QUASIPARTICLE TUNNELING SPECTRA

We now turn to quasiparticle tunneling spectra. Figure 3(a) shows differential conductance curves, $G(V) = dI/dV(V)$, of the 20-μm-wide junction for voltages $|V| \leqslant 15$ mV. The curves were measured with lock-in technique. Coherence peaks are clearly visible at voltages near ± 5 mV. To show that $G(V)$ indeed probes the density of states (DOS) we have integrated the $G(V)$ curves between $-15\,\text{mV} < V < 15\,\text{mV}$ [cf. inset of Fig. 3(a)]. The maximum deviation from the value at 4.2 K is $\sim 1\%$, i.e., within experimental accuracy, the total DOS is constant. At $|V| > 10$ mV $G(V)$ increases linearly with V. Such a V-shaped background conductance $G_n(V)$ has also been reported for T'-compound GBJs[45,46] and is indicative of a normal state DOS increasing linearly with energy. To determine $G_n(V,T)$ we use the expression $G_n(V,T) = e^{-1} \frac{d}{dV} \int_{-\infty}^{\infty} N_n(E)[f(E - eV) - f(E)]dE$, with $N_n(E) \propto a\,|E| + b$ and $f(E) = [1 + \exp(E/k_B T)]^{-1}$, which is fitted to the measured $G(V)$ curves (for $|V| > 10$ mV) for different values of T. The resulting $G_n(V,T)$ exhibit some rounding at low voltages, as illustrated in the left inset of Fig. 3(b) for $T = 4.2$ K. Figure 3(b) shows the normalized conductance $G(V)/G_n(V)$ for temperatures between 4.2 and 15.9 K.

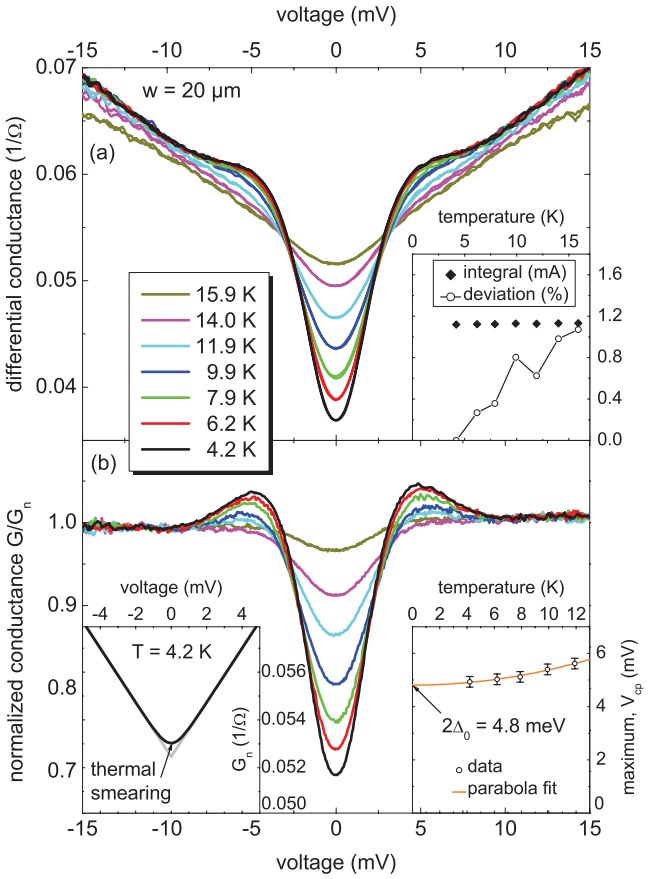

FIG. 3. (Color online) (a) Differential conductance $G(V)$ of 20-μm-wide SLCO GBJ for different values of T. The inset shows the integral of the $G(V)$ curves vs T for $-15\text{mV} \leqslant V \leqslant 15\text{mV}$ and the deviation from the integral at 4.2 K. (b) Normalized conductance $G/G_n(V)$ at various temperatures. The left inset shows the normal state conductance $G_n(V)$ at 4.2 K used for normalization. The development of the coherence peak position V_{cp} with temperature is illustrated in the right inset.

For a fully gapped superconductor the subgap conductivity is U-shaped while for an order parameter with nodes a V-shape is obtained.[47] Thermal smearing[48] and lifetime limiting processes[49] are rounding the spectra but do not change the substantial shape of the subgap conductivity. Both Figs. 3(a) and 3(b) show that in the subgap regime the conductance is V shaped. Moreover, the V shape becomes more pronounced for decreasing temperature. These findings suggest that nodes are present in the superconducting order parameter.

The normalized $G(V)/G_n(V)$ curves revealed a slight increase of the coherence peak position V_{cp} with increasing T [cf. right inset in Fig. 3(b)]. Such behavior is usually explained by thermal smearing, although, according to BCS theory, the increase of V_{cp} should be more pronounced.[48] T'-compound GBJs, however, even revealed a *decrease* of V_{cp} with increasing T.[45,46] Furthermore, in GBJs $V_{cp}(0) = 2\Delta_0/e$.[47,48] A parabolic fit extrapolated to $V_{cp}(0) = (4.8 \pm 0.2)$ mV, yielding $\Delta_0 = (2.4 \pm 0.1)$ meV for the 20-μm-wide junction. Other junctions with different widths revealed essentially the same value. We thus find a reduced gap ratio $2\Delta_0/(k_B T_c) = 3.0 \pm 0.2$, which is somewhat lower than the BCS value 3.5.[50] We

note that our data are in contrast to low-temperature scanning tunneling microscopy (STM) results reported for polycrystalline $Sr_{0.9}La_{0.1}CuO_2$ bulk samples[51] with $T_c = 43$ K, where the gap was determined to $\Delta_0 = (13 \pm 1)$ meV, yielding $2\Delta_0/(k_B T_c) = 7.0 \pm 0.5$. However, our data are in line with results obtained on other T'-compound thin-film GBJs, where $2\Delta_0/(k_B T_c) = 2.8$–$3.5$.[45,46] Furthermore, according to an empirical dependence of the reduced gap ratio on T_c, a ratio of ~ 4 is expected for samples with $T_c = 19$ K (cf. Wei *et al.*[52] and the literature cited therein), which is also close to our data.

The conductance spectra of our junctions did not show a zero-bias conductance peak.[19,53,54] For $Nd_{2-x}Ce_xCuO_{4-\delta}$, the absence of a ZBCP in GBJ QP spectra has primarily been interpreted as evidence for s-wave pairing.[18] However, subsequent experiments identified $Nd_{2-x}Ce_xCuO_{4-\delta}$ as a d-wave superconductor[55] indicating that the ZBCP has been suppresed, e.g., by strong disorder at the barrier, reducing the QP mean-free path l_0 to a value below the in-plane coherence length ξ_{ab} and therefore suppressing the constructive interference of electron- and hole-like QPs forming Andreev bound states.[56] We also refer to the work of Giubileo *et al.*[57] who performed point-contact spectroscopy on $Pr_{1-x}LaCe_xCuO_{4-y}$ crystals. They showed, that depending on the barrier strength Z, different conductance regimes were accessible, the high-Z tunneling regime and the low-Z contact regime, where ZBCPs only occurred in the latter one. Thus, from the absence of a ZBCP in our QP spectra, we cannot conclude s-wave pairing.

VI. CONCLUSIONS

In summary, we have fabricated high-quality GBJs from the electron-doped infinite-layer superconductor $Sr_{1-x}La_xCuO_2$ ($x = 0.15$) deposited on 24° symmetric [001]-tilt $SrTiO_3$ bicrystals. While in many respects these junctions are comparable to GBJs made of other cuprates, there are also differences. For example, the Josephson critical current density of up to 1.4×10^3 A/cm^2 at 4.2 K is remarkably high for electron-doped cuprates. The magnetic field dependence of the critical current follows a nearly perfect Fraunhofer pattern which is quite unusual for 24° cuprate grain-boundary junctions. As for other cuprates, the quasiparticle spectra of our GBJs are V shaped in the subgap regime indicative of a superconducting order parameter with nodes. For a d-wave order parameter we would have expected zero-bias conductance peaks which, however, were absent in our samples. It remains to be shown whether this is due to a suppression, e.g., by strong disorder at the barrier or due to an order parameter without sign change.

ACKNOWLEDGMENTS

J.T. gratefully acknowledges support by the Evangelisches Studienwerk e.V. Villigst. V.L. acknowledges partial financial support by the Romanian Ministry of Education and Research (Human Resources Reintegration Project No. 1476/2006) and by CNCSIS -UEFISCSU Project No. PNII - IDEI ID_743/2007). This work was funded by the Deutsche Forschungsgemeinschaft (Project No. KL 930/11).

*koelle@uni-tuebingen.de

[1] Y. Tokura, H. Takagi, and S. Uchida, Nature (London) **337**, 345 (1989).
[2] H. Takagi, S. Uchida, and Y. Tokura, Phys. Rev. Lett. **62**, 1197 (1989).
[3] T. Siegrist, S. M. Zahurak, D. W. Murphy, and R. S. Roth, Nature (London) **334**, 231 (1988).
[4] M. G. Smith, A. Manthiram, J. Zhou, J. B. Goodenough, and J. T. Markert, Nature (London) **351**, 549 (1991).
[5] G. Er, S. Kikkawa, F. Kanamaru, Y. Miyamoto, S. Tanaka, M. Sera, M. Sato, Z. Hiroi, M. Takano, and Y. Bando, Physica C **196**, 271 (1992).
[6] G. Er, Y. Miyamoto, F. Kanamaru, and S. Kikkawa, Physica C **181**, 206 (1991).
[7] N. Ikeda, Z. Hiroi, M. Azuma, M. Takano, Y. Bando, and Y. Takeda, Physica C **210**, 367 (1993).
[8] J. D. Jorgensen, P. G. Radaelli, D. G. Hinks, J. L. Wagner, S. Kikkawa, G. Er, and F. Kanamaru, Phys. Rev. B **47**, 14654 (1993).
[9] C. Niu and C. M. Lieber, Appl. Phys. Lett. **61**, 1712 (1992).
[10] H. Adachi, T. Satoh, Y. Ichikawa, K. Setsune, and K. Wasa, Physica C **196**, 14 (1992).
[11] S. Karimoto, K. Ueda, M. Naito, and T. Imai, Appl. Phys. Lett. **79**, 2767 (2001).
[12] R. Gross, *Interfaces in High-T_c Superconducting Systems* (Springer-Verlag, Berlin, 1994), pp. 176–209.
[13] J. Mannhart and P. Chaudhari, Phys. Today **54**(11), 48 (2001).
[14] H. Hilgenkamp and J. Mannhart, Rev. Mod. Phys. **74**, 485 (2002).
[15] P. Chaudhari, J. Mannhart, D. Dimos, C. C. Tsuei, J. Chi, M. M. Oprysko, and M. Scheuermann, Phys. Rev. Lett. **60**, 1653 (1988).
[16] D. Koelle, R. Kleiner, F. Ludwig, E. Dantsker, and J. Clarke, Rev. Mod. Phys. **71**, 631 (1999).
[17] C. C. Tsuei and J. R. Kirtley, Rev. Mod. Phys. **72**, 969 (2000).
[18] L. Alff, A. Beck, R. Gross, A. Marx, S. Kleefisch, T. Bauch, H. Sato, M. Naito, and G. Koren, Phys. Rev. B **58**, 11197 (1998).
[19] C.-R. Hu, Phys. Rev. Lett. **72**, 1526 (1994).
[20] S. Kashiwaya and Y. Tanaka, Rep. Prog. Phys. **63**, 1641 (2000).
[21] G. Deutscher, Rev. Mod. Phys. **77**, 109 (2005).
[22] C. C. Tsuei, J. R. Kirtley, C. C. Chi, Lock See Yu-Jahnes, A. Gupta, T. Shaw, J. Z. Sun, and M. B. Ketchen, Phys. Rev. Lett. **73**, 593 (1994).
[23] R. R. Schulz, B. Chesca, B. Goetz, C. W. Schneider, A. Schmehl, H. Bielefeldt, H. Hilgenkamp, and J. Mannhart, Appl. Phys. Lett. **76**, 912 (2000).
[24] B. Chesca, K. Ehrhardt, M. Mößle, R. Straub, D. Koelle, R. Kleiner, and A. Tsukada, Phys. Rev. Lett. **90**, 057004 (2003).
[25] F. Lombardi, F. Tafuri, F. Ricci, F. MilettoGranozio, A. Barone, G. Testa, E. Sarnelli, J. R. Kirtley, and C. C. Tsuei, Phys. Rev. Lett. **89**, 207001 (2002).
[26] J. Tomaschko, C. Raisch, V. Leca, T. Chassé, R. Kleiner, and D. Koelle, Phys. Rev. B **84**, 064521 (2011).

[27]J. Tomaschko, V. Leca, T. Selistrovski, S. Diebold, J. Jochum, R. Kleiner, and D. Koelle (unpublished).
[28]H. Hilgenkamp and J. Mannhart, Appl. Phys. Lett. **73**, 265 (1998).
[29]S. Kleefisch, L. Alff, U. Schoop, A. Marx, R. Gross, M. Naito, and H. Sato, Appl. Phys. Lett. **72**, 2888 (1998).
[30]M. Wagenknecht, Ph.D. thesis, University of Tuebingen, Germany, 2008.
[31]D. Winkler, Y. M. Zhang, P. A. Nilsson, E. A. Stepantsov, and T. Claeson, Phys. Rev. Lett. **72**, 1260 (1994).
[32]G. Deutscher and K. A. Müller, Phys. Rev. Lett. **59**, 1745 (1987).
[33]J. Mannhart, P. Chaudhari, D. Dimos, C. C. Tsuei, and T. R. McGuire, Phys. Rev. Lett. **61**, 2476 (1988).
[34]V. Ambegaokar and A. Baratoff, Phys. Rev. Lett. **10**, 486 (1963); **11**, 104 (1963).
[35]J. H. T. Ransley, P. F. McBrien, G. Burnell, E. J. Tarte, J. E. Evetts, R. R. Schulz, C. W. Schneider, A. Schmehl, H. Bielefeldt, H. Hilgenkamp, and J. Mannhart, Phys. Rev. B **70**, 104502 (2004).
[36]R. Gross and B. Mayer, Physica C **180**, 235 (1991).
[37]S.-I. Karimoto and M. Naito, Appl. Phys. Lett. **84**, 2136 (2004).
[38]R. Gross, P. Chaudhari, D. Dimos, A. Gupta, and G. Koren, Phys. Rev. Lett. **64**, 228 (1990).
[39]V. Ambegaokar and B. I. Halperin, Phys. Rev. Lett. **22**, 1364 (1969).
[40]P. A. Rosenthal, M. R. Beasley, K. Char, M. S. Colclough, and G. Zaharchuk, Appl. Phys. Lett. **59**, 3482 (1991).
[41]D. D. Coon and M. D. Fiske, Phys. Rev. **138**, A744 (1965).
[42]J. C. Swihart, J. Appl. Phys. **32**, 461 (1961).
[43]Y. M. Zhang, D. Winkler, P.-A. Nilsson, and T. Claeson, Phys. Rev. B **51**, 8684 (1995).
[44]R. E. Eck, D. J. Scalapino, and B. N. Taylor, Phys. Rev. Lett. **13**, 15 (1964).
[45]S. Kleefisch, B. Welter, A. Marx, L. Alff, R. Gross, and M. Naito, Phys. Rev. B **63**, 100507 (2001).
[46]M. Wagenknecht, D. Koelle, R. Kleiner, S. Graser, N. Schopohl, B. Chesca, A. Tsukada, S. T. B. Goennenwein, and R. Gross, Phys. Rev. Lett. **100**, 227001 (2008).
[47]H. Won and K. Maki, Phys. Rev. B **49**, 1397 (1994).
[48]C. Noce and M. Cuoco, Il Nuovo Cimento D **18**, 1449 (1996).
[49]R. C. Dynes, V. Narayanamurti, and J. P. Garno, Phys. Rev. Lett. **41**, 1509 (1978).
[50]J. Bardeen, L. N. Cooper, and J. R. Schrieffer, Phys. Rev. **108**, 1175 (1957).
[51]C.-T. Chen, P. Seneor, N.-C. Yeh, R. P. Vasquez, L. D. Bell, C. U. Jung, J. Y. Kim, M.-S. Park, H.-J. Kim, and S.-I. Lee, Phys. Rev. Lett. **88**, 227002 (2002).
[52]J. Y. T. Wei, C. C. Tsuei, P. J. M. van Bentum, Q. Xiong, C. W. Chu, and M. K. Wu, Phys. Rev. B **57**, 3650 (1998).
[53]S. Kashiwaya, Y. Tanaka, M. Koyanagi, H. Takashima, and K. Kajimura, Phys. Rev. B **51**, 1350 (1995).
[54]Y. Tanaka and S. Kashiwaya, Phys. Rev. Lett. **74**, 3451 (1995).
[55] Ariando, D. Darminto, H.-J. H. Smilde, V. Leca, D. H. A. Blank, H. Rogalla, and H. Hilgenkamp, Phys. Rev. Lett. **94**, 167001 (2005).
[56]M. Aprili, M. Covington, E. Paraoanu, B. Niedermeier, and L. H. Greene, Phys. Rev. B **57**, R8139 (1998).
[57]F. Giubileo, S. Piano, A. Scarfato, F. Bobba, A. D. Bartolomeo, and A. M. Cucolo, Physica C **470**, 922 (2010).